Stress-Mediated Reaction Pathways for Dislocation Nucleation in Copper

by

Robert D. Boyer

B.S. Materials Science and Engineering

Case Western Reserve University

M. S. Materials Science and Engineering

Massachussetts Institute of Technology

SUBMITTED TO THE DEPARTMENT OF MATERIALS SCIENCE AND ENGINEERING
IN PARTIAL FULFILLMENT OF THE REQUIREMENTS FOR THE DEGREE OF

DOCTOR OF PHILOSOPHY IN MATERIALS SCIENCE AND ENGINEERING
AT THE
MASSACHUSETTS INSTITUTE OF TECHNOLOGY

JUNE 2007

Signature of Author: .....
Department of Materials Science and Engineering
May 25, 2007

Certified by: .....
Sidney Yip
Professor of Nuclear Science and Engineering

Thesis Supervisor

Accepted by: .....
Samuel M. Allen
POSCO Professor of Physical Metallurgy
Chair, Departmental Committee on Graduate Students

Stress-Mediated Reaction Pathways for Dislocation Nucleation in Copper

by

Robert D. Boyer

Submitted to the Department of Materials Science and Engineering
on May 25, 2007 in Partial Fulfillment of the
Requirements for the Degree of Doctor of Philosophy in
Materials Science and Engineering

Abstract

The ductile behavior of metals requires dislocation nucleation, from either homogeneous or heterogeneous sources, in order to produce the large number of dislocations necessary for extensive plastic deformation. As with the majority of the defect processes that comprise deformation and failure of materials, dislocation nucleation is well described in the framework of transition state theory as a stress-mediated, thermally activated process. We have used reaction pathway sampling methods and well-fit empirical potentials to determine the stress-dependent behavior of and atomistic mechanisms for dislocation nucleation at stresses much lower than typically accessible to atomistic techniques. We have shown that a significant range of stresses exist for which homogeneous dislocation loop nucleation is feasible because the critical nucleate transitions to an in-plane shear perturbation where the shear displacement of most particles is significantly less than the Burger's vector. We have also revealed that the common structural conception of activation volume for dislocation nucleation does not apply for all stresses and in general over-predicts the stress-dependence of activation by considering only the shear displacement of the critical defect. Furthermore, by considering the full reaction pathway for dislocation nucleation in perfect crystals and at a vacancy, we have provided a fully atomistic description of shear localization via an expanded one-dimensional chain analysis of the wave-steepening behavior. Lastly, both breaking the local atomic symmetry and increasing the extent of heterogeneous nucleation sites are shown to lower the activation energy for dislocation nucleation. In general we have applied reaction pathway sampling to the problem of dislocation nucleation in Cu not only for a perfect crystal, but also in the presence of point defects, vacancy clusters and nanowire surfaces. As a result the strength of a variety of nucleation sites in mediating activation as well as specific atomistic mechanisms for dislocation nucleation have been discussed from both structural and energetic perspectives.

Thesis Supervisor: Sidney Yip

Title: Professor of Nuclear Science and Engineering and Materials Science and Engineering

Acknowledgements

I have not made the journey through graduate school alone. I would first like to acknowledge my advisor, Prof. Sidney Yip, for his support and direction throughout my thesis work. His experience has been a tremendous resource over the last five years.

The input of my thesis committee members, Prof. Chris Schuh and Prof. Nicola Marzari, has shaped my thesis significantly, and I thank them for it.

I have had the privilege of stable support from Lawrence Livermore National Laboratory throughout my thesis work and also the opportunity to visit and interact with many of the great people from LLNL.

The various members of my research group, past and present, have been vital to overcoming obstacles both small and large throughout graduate school. A second pair of eyes or an alternate perspective are often critical to research progress. These have come from the students, post-docs, alumni and visitors that have comprised Prof. Yip's research group throughout my graduate research. Their contribution is immeasurable.

Of course without friends and family none of this matters. My biggest thanks go out to everyone who has walked with me personally through graduate school. The end is sweeter for having reached it with all of you.

Contents

List of Figures

Figure 2-5: The evolution of the configurational energy for five MD simulations at 0.0001 K of a perfect FCC Cu lattice under <112>{111} simple shear at τ = 3.7683, 3.7702, 3.771, 3.7718 and 3.7725 GPa in order of increasing initial energy indicates that τ_{ath} falls between 3.771 and 3.7718 GPa.

Figure 2-6: The activation energy versus applied shear stress shows reasonable agreement for two different simulation cell sizes (~12.5 nm edge lengths versus ~6.2 nm edge lengths).

Figure 2-7: In order of increasing applied stress, the saddle point configuration takes the form of a) a partial dislocation loop, b) an in-plane shear perturbation, and c) a shear wave normal to the slip plane. Configurations representing the three observed structural saddle point regimes are colored here according to the centrosymmetry parameter with ranges of a) 0.039 to 0.25, b) 8.2×10^{-4} to 3.8×10^{-3} and c) 6×10^{-17} to 1.3×10^{-12}.

Figure 2-8: A schematic of the atomic displacements (arrows) adjacent to a slip plane (bold dashed line) illustrates that the atomic displacements cannot be used to directly calculate the displacement across the slip plane. In the picture, dashed circles represent the reference FCC lattice while the solid circles are the displaced particles.

Figure 2-9: The inelastic displacement across the slip plane for a) a partial dislocation loop and b) and in-plane shear perturbation which are calculated by fitting displacements to a set of positions in the slip plane in order to calculate the relative displacement between the two planes.

Figure 2-10: The structurally defined activation volume for an in-plane shear perturbation is calculated via two methods which are schematically represented in two-dimensions. The volume under the displacement curve is approximated in a) as the length swept out multiplied by the maximum of the profile. A more refined numerical approximation in b) takes a similar approach but divide the profile into a series of small line lengths each with an associated displacement.

Figure 2-11: The activation volume for homogeneous dislocation loop nucleation calculated using three definitions: the integral of the in-plane shear displacement (open squares), the area swept out by half the peak displacement multiplied the peak displacement (open circles), and the derivative of activation energy w.r.t applied shear stress (solid line) is plotted as a function of the normalized <112>{111}shear stress in the system.

Figure 2-12: The maximum inelastic shear displacement decreases to zero at the athermal stress.

Figure 2-13: The area swept out by the dislocation, defined here as the portion of the slip plane with shear displacement > 0.003Å, decreases with increasing applied shear stress until near the athermal stress where the dislocation begins to spread in the slip plane.

Figure 3-1: Schematic representation of the energetic contributions to the PN model of a dislocation. The slip plane is represented by the horizontal dashed line, the vertical dotted lines correspond to the original "lattice" and the magnitude of the misfit across the slip plane is given by the arrows. In a) the constant displacement in the elastic body above the slip plane yields only misfit energy; whereas the gradient in the displacement profile in b) disrupts the lattice above the slip plane leading to an additional elastic energy term.

Figure 3-2: The stress-dependent misfit energy, γ, is plotted here in terms of the normalized elastic, x_0/b_p, and plastic, x_1/b_p, displacements between the two atomic planes surround the slip plane. Values are normalized by the partial Burger's vector.

Figure 3-3: The shear stress associated with simple shear for Cu calculated via the atomistic empirical potential by Mishin.

Figure 3-4: An example CINEB reaction pathway for homogeneous dislocation loop nucleation was calculated using the PN model (open circles) at $\tau = 3.68$ GPa.

Figure 3-5: The relaxed image configurations for the sample CINEB reaction pathway for homogeneous dislocation loop nucleation at $\tau = 3.68$ GPa are a series of displacement profiles with radial symmetry. The displacement at each of the 256 nodes representing a circular slice of the slip plane with radius, r, are shown for the nine image configurations along the reaction pathway.

Figure 3-6: The activation energy calculated via CINEB using the PN model (open circles) decreases at a much higher rate with applied shear stress than the least-squares fit behavior taken from atomistic CINEB with the Mishin Cu potential (dashed line).

Figure 3-7: The activation volumes calculated from the least square fitting of the atomistic CINEB (dashed line) and PN model CINEB (solid line) activation energies reflect the difference in stress dependence. The structurally defined activation energy calculated from the PN model (open squares) is also plotted.

Figure 3-8: The activation energy, Q_{H0}, calculated via the CINEB method using the PN model holding constant the shear modulus (open circles) falls between Q_{PN} (dotted line) and the activation energy from the atomistic CINEB calculations, Q (dashed line). The CINEB data does not fit well (solid line) to the form used for the atomistic data.

Figure 3-9: The activation volume calculated from the least-squares fitting of the atomistic NEB (dashed line) and the constant shear modulus PN model (solid line) exhibit the same general trend with significantly lower volume from the PN model. The structural defined activation volume (open squares) from the constant shear modulus PN model increases as τ approaches τ_{ath}.

Figure 4-1: Full energetic pathway for homogeneous nucleation of a leading and trailing partial dislocation loop under <110>{111} simple shear strain of 0.96. The inset shows the biased image density maintained prior to the climbing image along the pathway.

Figure 4-2: The shear displacement in the <110> and the <112> directions between each particle in the initial configuration and the corresponding particle in the first eight images along the reaction pathway are plotted here versus the normalized particle position in the <111> direction normal to the slip plane. The displacement profiles, given in units of angstroms, show linear growth of a shear wave until R_8, where spreading is observed in the particle displacements in each plane.

Figure 4-3: The displacement in the <110> and <112> directions from the initial perfect crystal configuration to a series of images along the reaction pathway is plotted for each of 161,280 particles in the atomistic CINEB calculation. The pathway corresponds to a) the onset of shear localization, b) the nucleation of a leading partial dislocation loop, c) the formation of an unstable stacking fault, d) the nucleation of a trailing partial dislocation loop and e) the return of a prefect crystal whose strain is decreased by the Burger's vector compared to the initial perfect crystal configuration.

Figure 4-4: A sample one-dimensional chain in the three-dimensional configuration shows the spiral pattern along the chain direction which is a consequence of the atomic stacking of {111} slip planes in an FCC lattice

Figure 4-5: The positions relative to the emerging defect for the two one-dimensional chains used in the current analysis are shown as a white circle, chain A, and a green square, chain B. Chain A passes through the center of the emerging defect while chain B is as far from the center as possible considering the periodic boundary condition.

Figure 4-6: For each particle in chain A (points) and chain B (open squares) the displacement between the initial strained perfect crystal configuration and a series of images along the reaction pathway for dislocation nucleation exhibit the four stages of wave steepening. Shear localization in chain A occurs with a) initial divergence from the uniform linear growth of the entire system (R_7) and proceeds through b) non-linear growth (R_8), c) formation of a shear shock (R_{10}) and ultimately d) atomistic defect nucleation (R_{12}). Displacements are given in units of angstroms.

Figure 4-7: Atomistic configurations colored by the centrosymmetry parameter representing the four stages of wave steepening a) linear growth, b) non-linear growth, c) shear shock formation and d) atomistic defect formation.

Figure 4-8: The reaction pathway for dislocation nucleation at a vacancy, calculated with the CINEB method and the free-end algorithm, provides the energy (open circles) and atomistic configurations for a series of images for use in the three-dimensional wave-steepening analysis.

Figure 4-9: The positions relative to the emerging defect for the two one-dimensional chains used in the analysis of dislocation nucleation at a vacancy are shown as a white circle, chain A_{vac}, and a green square, chain B_{vac}. Chain A_{vac} passes through the crystal adjacent to the vacancy while chain B_{vac} is as far from the vacancy as possible considering the periodic boundary condition.

Figure 4-10: For each particle in chain A_{vac} (points) and chain B_{vac} (open squares) the displacement between the initial relaxed vacancy configuration and a series of images along the reaction pathway for dislocation nucleation exhibit the four stages of wave steepening. In the vicinity of the vacancy chain A_{vac} exhibits a) linear growth of local shear displacement wave (R_1 and R_5) b) non-linear growth (R_6), c) formation of a shear shock (R_7) and ultimately d) atomistic defect nucleation (R_9). Displacements are given in units of angstroms.

Figure 4-11: Displacement profile at both chain A_{vac} and chain B_{vac} for the initial configuration along the reaction pathway taking a perfect FCC lattice as the reference configurations. All displacements are in angstroms.

Figure 5-1: The activation energy for dislocation nucleation at a vacancy was calculated via the CINEB method (open circles) for a range of <112>{111} shear stresses, τ, and fit via the least-squares method to Equation 2.1 (solid black line). At all τ the vacancy-mediated activation energy is lower than the energy for homogeneous nucleation (dashed line).

Figure 5-2: The activation volume calculated as the derivative of the activation energy (solid line) and the integral of the inelastic displacement in the slip plane (open squares) for dislocation nucleation at a vacancy show trends very similar to the observed behavior for homogeneous nucleation.

Figure 5-3: A series of snapshots from atomistic configurations along the pathway for dislocation nucleation at a vacancy reveal a behavior reminiscent of a Frank-Reed source. Centrosymmetry for all snapshots ranges from 0.037 to 0.26 with dark blue for the stacking fault (c.s. $\approx$ 0.04) and all other colors corresponding to the dislocation line or, as in a) the vacancy. An initial leading partial dislocation is b) nucleated, c) grows from the vacancy, d) finally breaks free from the point defect e) impinges on itself and f) annihilates to form a stacking fault from which g) a trailing partial dislocation is nucleated and grows to bow out at the vacancy before eventually h) breaking free of the dislocation and i) annihilating itself through the periodic boundary.

Figure 5-4: Increasingly large clusters of atoms were removed from a perfect crystal to create configurations with nearly spherical vacancy clusters. Each of these clusters is labeled with the number of particles it contains.

Figure 5-5: The activation energy for dislocation nucleation under constant <112>{111}shear stress strain for a series of increasingly large vacancy clusters indicates that the behavior is dominated by the surface symmetry and not the cluster size at atomic length scales.

Figure 5-6: The saddle point configurations along the reaction pathway for dislocation nucleation at a) the 13 and b) 19 vacancy clusters are represented by the particles with non-FCC symmetry which include the dislocation loops and the atoms surrounding the cluster. In addition the four slip planes which intersect the cluster are represented by dashed lines.

Figure 5-7: Displacement profiles for a series of parallel <111> slip planes intersecting the thirteen-vacancy cluster illustrate the local atomic relaxation near the cluster relative to a perfect crystal lattice.

Figure 5-8: Displacement profiles for a series of parallel <111> slip planes intersecting the nineteen-vacancy cluster illustrate the local atomic relaxation near the cluster relative to a perfect crystal lattice.

Figure 5-9: The nanorod configuration used for NEB calculations contains 205,480 particles and is initially 25 nm long and 10.8 nm in diameter.

Figure 5-10: In the snapshot from an MD simulation, particles are colored according to the centrosymmetry parameter with all FCC particles removed to reveal a partial dislocation loop emerging from the surface of the nanorod and leaving a stacking fault in its wake.

Figure 5-11: The activation energy for nucleation of a dislocation loop at the surface of a nanowire pulled in tension is plotted with respect to the resolved shear stress in the activated slip system.

Figure A-1: The behavior of the reaction coordinate as the NEB simulation progresses is one indicator that a simulation is converging.

Figure A-2: The behavior of the reaction pathway under the influence of the updated variable spring constant method which creates high image density near the saddle point (reaction coordinate ≈ 0.04) and uniform image density along the portions of the path with $E_i < E_{ref}$.

Figure A-3: The reaction pathway for an unconverged NEB simulation utilizing the free-end algorithm is a) susceptible to escaping the 'free end' but b) can be caught via a simple addition to the methodology.

Figure A-4: The reaction pathway escapes from the free end and is updated five times before finding a stable free end which allows the simulation to converged to the minimum energy pathway.

Chapter 1

Introduction

1.1 Motivation and Background

Strength is a fundamental consideration for most material applications. Both the onset and accumulation of plastic deformation are critical to the understanding of material strength, and each can be described in terms of macroscopic constitutive behavior and continuum theory. In fact, although the unit processes involved in yield and deformation occur primarily at the atomistic level [1, 2], the fundamental theoretical work describing the structure and properties of dislocations began in the early part of the 20^{th} century before researchers had access to atomic-scale information from either microscopy or atomistic simulations. Detailed atomistic studies to gain insight into the mechanisms for yield and plastic deformation governing materials strength can lead to a broader understanding of the macroscopic behavior of materials under applied stress.

Atomistic simulations techniques have been used extensively to study the deformation of materials [3-16]. Specifically, molecular dynamics (MD) can be used to probe the time-dependent evolution of an atomistic system driven by an applied stress or strain state [17]. However, in order to accurately capture the vibrational motion of atoms a timestep on the order of femtoseconds is required. The constrained timestep for MD constitutes a severe limitation to the total time that can be feasibly simulated with current computational resources. Deformation studies with MD are therefore limited to extremely high strain rates, on the order of 1×10^8 s^{-1} at the lowest [9, 18]. The majority of material applications and experimental work occurs at strain

rates eight to ten orders of magnitude lower than those accessible by MD. As a result of the high strain rate, the stress driving the formation and propagation of defects via MD simulation typically meets or exceeds the athermal limit at which the processes are expected to occur spontaneously.

Deformation unit processes, such as dislocation nucleation, are stress-mediated, thermally activated transitions. In order to outline the relevant behavior of such transitions, we will consider a system at equilibrium under zero applied shear stress, τ, which sits at a local minimum in a model potential energy landscape. In Figure 1-1 this configuration is depicted schematically as A at $\tau = 0$. The transition to state B requires overcoming an energetic barrier and at $\tau = 0$ the final state is energetically unfavorable. When a shear stress is imposed on the system, the potential energy landscape shifts until, at the athermal stress, $\tau = \tau_{ath}$ in Figure 1-1, the activation barrier for the transition disappears. The initial configuration has become unstable, and any small perturbation of the system will cause immediate transition. In the example of dislocation nucleation, the crystalline lattice becomes mechanically unstable and a dislocation forms spontaneously at this critical stress. For any stress below τ_{ath} the activation barrier, Q, can be defined as the difference between the energy of the local equilibrium configuration at A and the maximum energy for the transition that must be overcome to reach state B which occurs at the energy peak in Figure 1-1 or, in higher dimensional space, a saddle point configuration. In general a range of stresses exist for which the transition to state B is favorable but requires the application of some thermal energy to overcome the activation barrier. Many deformation unit processes such as dislocation nucleation, cleavage decohesion, and twin boundary migration can be accurately described in the terms of thermally-activated processes with stress-mediated activation barriers[5, 19, 20].

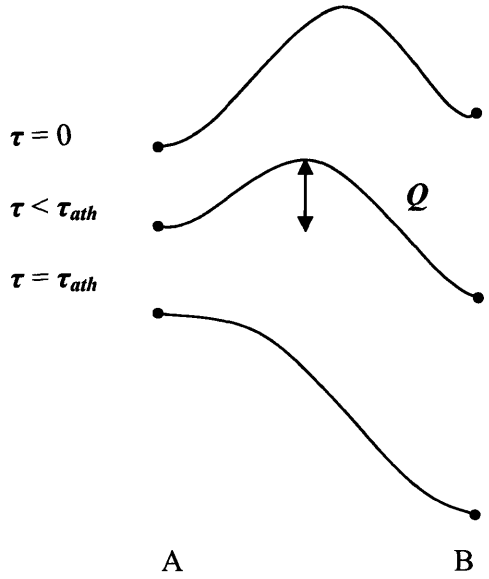

Figure 1-1: The schematic of a stress mediated activation barrier shows the behavior of the reaction pathway as a function of applied load: $\tau = 0$ where the initial configuration, A, is stable with respect to configuration B, $\tau < \tau_{ath}$ where configuration A is metastable with respect to configuration B and the transition is governed by the activation barrier, Q, and $\tau = \tau_{ath}$ where $Q = 0$ and configuration A spontaneously relaxes to configuration B with any perturbation.

Although much work atomistic work has been performed to study the deformation of materials, particularly via MD simulation, another group of methods developed specifically to efficiently probe configuration space has recently been adopted by the materials community. The methods, broadly described as reaction pathway sampling methods, search for the saddle point configurations and in some cases the full minimum energy pathway between stable configurations. These include the nudged elastic band (NEB) method [21, 22] and the dimer method [23, 24] which have recently been developed and have not been used to explore materials problems to the same extent as MD or other more established atomistic simulation methods. However, some examples of the application of these methods to materials processes do exist, predominantly in the study of dislocation motion [6, 25, 26] and crack extension [3, 27]. As the name implies, reaction pathway sampling methods yield information regarding the energetics of "reaction pathways" including the minimum energetic barrier to a material transition found at the saddle point configuration and, in some cases, the entire minimum energy path between the initial and final stable states.

Reaction Pathway Sampling Methods

The majority of the work presented in this thesis makes use of the NEB method, which is an efficient numerical scheme for finding both the saddle point configuration and minimum energy pathway between an initial and final state. In the NEB method an initial and final configuration

are required as input, but a specific reaction coordinate, such as the radius of a dislocation loop, is neither known in advance nor imposed during the calculation. Instead the change in position of every particle in the system is taken as the reaction coordinate allowing the method to probe the entirety of configuration space. The NEB method also requires as input a series of configurations, known as images, which represent an initial guess at the pathway between the input initial and final configurations. In our discussion these images are denoted by $\boldsymbol{R_1}$, $\boldsymbol{R_2}$, ..., $\boldsymbol{R_{NI}}$ where $\boldsymbol{NI}$ is the number of images and $\boldsymbol{R_1}$ and $\boldsymbol{R_{NI}}$ correspond to the initial and final configurations which in the standard implementation of the NEB method are at all times fixed.

The energy landscape for a schematic system with only two degrees of freedom is plotted as a contour map in Figure 1-2. The initial images are shown as blue crosses and were produced through a simple linear interpolation between the initial and final configuration. A single iteration of the NEB method involves calculation of the tangent vector, $\boldsymbol{\tau_i}$, between each image, calculating the force, $\boldsymbol{F_i}$, on each image, and updating the series of images based on the forces. $\boldsymbol{F_i}$ is calculated as the sum of a non-physical spring force component acting parallel to the tangent and the true force component acting perpendicular to the tangent direction. The spring force ensures that the images remain equally spaced along the path and the true force is allowed to 'nudge' the images towards the minimum energy path (MEP). In Figure 1-2 two intermediate iterations of the relaxation are shown as a series of open circles. The final converged series of image configurations, given by open circles connected with a line, follows the MEP and includes two images falling fairly close to either side of the saddle point configuration. Reaction pathway sampling methods are an area of open research and several updates to the basic NEB formalism proposed by various researchers, including the use of a saddle point searching algorithm, have been put to use in the work that follows and are described in more detail alongside the projects for which each is used. In addition we have included, as Appendix A, a practical guide which discusses the use of the NEB method for problems in high-dimensionality configurational space and some solutions to method-base problems we have encountered along the way.

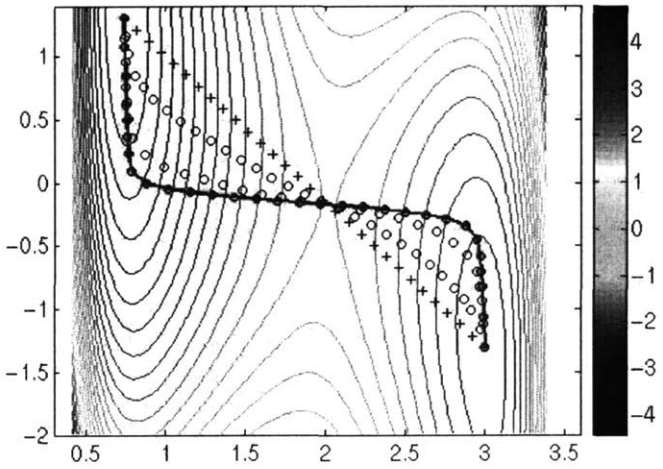

Figure 1-2: A contour plot of the energy landscape for an example of the nudged elastic band method in two dimensions where the crosses represent the initial linearly interpolated images, open circles represent intermediate stages and the circles connected by a solid line represent the final minimum energy path for the system.

Although unlike MD reaction pathways sampling methods provide no direct dynamic information, activation barriers for thermally activated processes and, in the case of the NEB, a series of configurations corresponding to a minimum energy pathway can be produced by efficiently probing potential energy hyperspace. These configurations can be thought of as a series of snapshots along the most probable path for the transition being studied and thereby yield mechanistic information without dynamics [28-30]. Furthermore in the context of transition state theory the activation barriers can be used to estimate a rate of transition [31].

A Comment on Potentials

The heart of any reaction pathway sampling method is the empirical potential or other energetic material description employed. Prior to the last decade, empirical potentials were predominantly fit to equilibrium properties such as lattice constants, cohesive energies, and elastic constants because experimental data for configurations away from equilibrium is relatively difficult to obtain [17, 32]. Potentials derived in this way often produce reasonable results for properties and configurations observed near equilibrium. However, the goal of reaction pathways sampling techniques is to accurately capture the energy and atomic configuration of a system along the entire pathway including configurations far from equilibrium. In fact the most critical configurations for the use of these methods in studying materials deformation are the unstable saddle point configuration associated with the activation barriers to defect nucleation and motion. The empirical potentials of the past could not have been constructively employed to sample these saddle point configurations. However, starting with a

potential fit by Sankey and Niklewski [33], which employed a force-matching scheme, empirical potentials have been increasingly fit to ab inito data which contains information about a wide range of configurations including those far from equilibrium [32, 34-36].

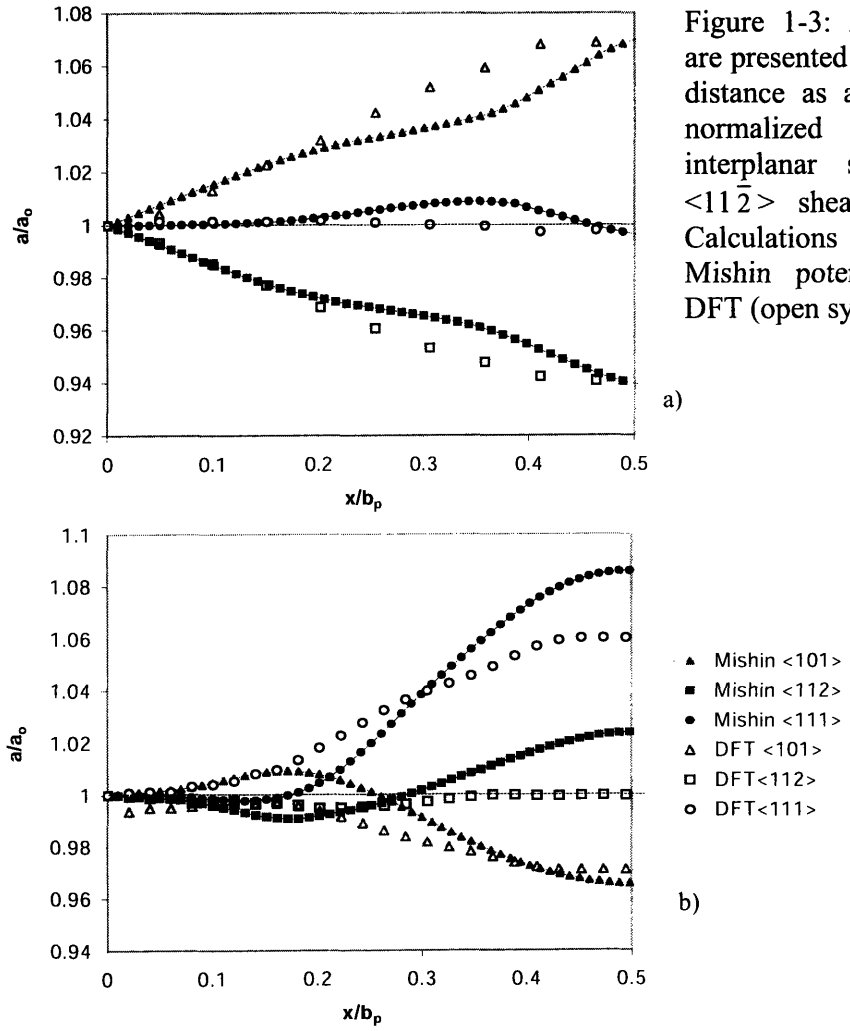

Figure 1-3: Atomic relaxation patterns are presented as the change in interplanar distance as a function of displacement normalized by the equilibrium interplanar spacing for pure {111} $<11\bar{2}>$ shear of a) Cu and b) Al. Calculations were performed with the Mishin potentials (closed symbols) and DFT (open symbols)

As an example of the advancing capabilities of modern potentials two Al EAM potentials by Ercolessi and Adams [32] and by Mishin and others [34] as well as a Cu EAM potential by Mishin and others [35] were benchmarked against ab initio calculations of the affine shear strain energy and the multiplane generalized stacking fault energy [37]. The full results are discussed elsewhere [12, 38, 39], but Figure 1-3 contains the relaxation pattern during affine shear of a) Cu and b) Al with the Mishin potentials and DFT calculations. The Cu potential accurately captures even these detailed unstable configurations related to shear deformation. The Al potential does

qualitatively capture much of the relaxation behavior observed with DFT; however, expansion occurs in the <112> direction which is not observed with DFT. The less robust nature of the potential for Al is related to the directional nature of bonding in Al [40, 41] and the relative difficulty of matching a potential with directional bonds to the inherently spherical EAM form [37, 42, 43]. The uniform, spherical nature of bonding in Cu makes it ideally suited for description by the functional form used in EAM potentials. This degree of benchmarking shows accurate reproduction of local atomic structure for configurations far from equilibrium in the case of the Cu potential and allows for detailed understanding of the results obtained with empirical potentials. Well-benchmarked, high-level empirical potentials have paved the way for confident use of reaction pathway sampling techniques to study the unit processes of plastic deformation.

The reaction pathways for many deformation unit processes such as dislocation nucleation and propagation have not been described with fully atomistic simulations at stresses significantly below the athermal load. In particular we will discuss dislocation nucleation in a variety of structural environments as a means of producing defects responsible for the extensive plastic deformation necessary for ductility in Cu. The combination of recently developed reaction pathway sampling methods and high-end empirical potentials will yield a more detailed mechanistic understanding of these unit processes than previously attainable through atomistic simulation.

1.2 Problem Statement

In this thesis we explore the stress-dependent behavior of dislocation nucleation in a ductile metal, Cu, in a perfect crystal, at a vacancy or vacancy cluster, and at the surface of a nanowire. For each system we apply the Nudged Elastic Band technique and the energetics from high-end empirical potentials, either directly for atomistic calculations or indirectly as input to continuum descriptions of dislocation nucleation. We therefore gain access to both energetic and mechanistic information for systems under a range of driving stresses that extends far below the athermal stress. Although the local environment for the emerging dislocation ranges from bulk

perfect crystal, to point defects and surfaces, the dislocations being nucleated are essentially equivalent allowing for discussion of the effects of the structural environment on the creation and propagation of a common defect contributing to plastic deformation. Within this context we engage several problems of current interests to the mechanics of materials community.

In chapter two, using the NEB method, we calculate the minimum energy pathway for homogeneous dislocation loop nucleation under a range of shear stresses approaching the athermal stress. The energetic and structural description of the saddle point provided by these calculations is used to bring together the conflicting structural and analytic definitions of activation volume. Furthermore, we are able to characterize the behavior of the saddle point configuration as a function of the applied shear stress in the general context of nucleation under a thermodynamic driving force. The fully atomistic calculations of activation energy also allow us to test the effectiveness of common continuum descriptions for the energetics of dislocation nucleation.

The atomistic simulations in chapter two intrinsically incorporate all of the stress-dependent behavior captured by the underlying empirical potential. However there is no straightforward way turn off and on the various contributions to the stress dependence when using the fully atomistic potential. With this in mind, we implement in chapter three a Peierls-Nabarro model within the NEB framework to pinpoint the physical origins of the stress-mediation for the test case of homogeneous dislocation nucleation.

In order to develop an atomistic understanding of the onset of plastic deformation, in chapter four we expand a simple one-dimensional chain description of the shear localization process to fully three-dimensional reaction pathways taken from NEB simulation. The onset of plastic deformation cannot be fully described by continuum theory or simulation because they ignore by design the discrete nature of the atomic lattice. Nucleation from a perfect crystal is more accessible to continuum description, but the many defect-mediated processes in materials deformation rely on specific atomic-scale mechanisms. The one-dimensional chain analysis first shows the general validity in three dimensions of the wave-steepening description of shear localization. Secondly, we compare the wave-steepening behavior for a perfect lattice and a

configuration containing a single vacancy in order to discuss the structural process of stress concentration at a heterogeneity and illuminate the process by which point defects predispose a lattice towards instability.

In chapter five, we discuss the effects of heterogeneity on the energetics of dislocation nucleation. In general heterogeneous nucleation is considered energetically favorable relative to a similar homogeneous process. As a result, moving from a fundamental discussion of nucleation in the model perfect crystal towards atomistic understanding of specific heterogeneous defect processes is a necessary step in describing plastic deformation in real materials. There are a vast array of heterogeneous process that can occur in the onset and accumulation of plastic deformation. We choose a few representative examples as an indication of the types of information accessible to reaction pathway sampling. First we perform an analysis of the stress-dependent behavior for dislocation nucleation at a vacancy to calculate the effects of a simple heterogeneity on the activation energy and activation volume. Secondly we calculate the reaction pathway for nucleating dislocations at a series of increasingly large vacancy clusters to observe the effects on the activation energy of increasing the lattice disruption and varying the local atomic structure of heterogeneities. Lastly we determine the effects of tensile loading on the activation energy for dislocation nucleation at the surface of a nanowire.

Chapter 2

Activation Volume for Homogeneous Dislocation Loop Nucleation via Atomistics

2.1 Introduction

Homogeneous dislocation loop nucleation is a classic problem in crystal plasticity often used as a test case for a variety of computational and theoretical work [44-48]. However, the viability of homogeneous nucleation as a mechanism for real materials deformation in competition with heterogeneous processes has long been in doubt [45] and has even been questioned as a potential explanation for material behavior under nanoindentation because of the relatively large volume involved in the production of a homogeneous dislocation loop [49, 50]. In order to discuss the feasibility of homogeneous dislocation nucleation, we have used atomistically-informed sampling methods to find stress-dependent reaction pathways and saddle point configurations with the purpose of measuring the rate at which applied stress decreases the activation energy, a quantity known as the activation volume. Further we have investigate the definition of activation volume in terms of atomic structure at the saddle point and will show that although the critical defect for nucleating a partial dislocation loop may encompass several hundred atoms, the nature of these defects allows the activation volume to remain low. Consequently the activation energy for homogeneous dislocation loop nucleation is low enough to be reasonably accessible to thermal fluctuation at stresses well below the athermal stress.

Activation volume is a key concept in our understanding of the many stress-mediated, thermally-activated mechanisms that make up deformation and eventual failure in materials. However, in practice the activation volume assumes numerous often conflicting definitions [45, 51]. Activation volume is strictly defined as the derivative with respect to stress of the activation energy for a thermally activated process [52]. In continuum-scale, thermodynamic descriptions of homogeneous dislocation nucleation such as those developed by Cottrell and Kocks the stress dependence is restricted solely to the work required to create a defect against a constant stress [45]. In this case the activation volume is typically defined structurally as the area swept out by the dislocation loop at the saddle point multiplied by the burger's vector of the dislocation. While this structural definition of activation volume holds to the strict definition for these models, its incorrect correlation with the actual stress dependence of deformation processes has gained wide usage [20, 53, 54]. Another set of alternative definitions come from the many basic nucleation formalisms in which "activation volume" is used as a constant fitting parameter with no indication of the widely accepted non-linear stress dependence of the activation energy. All of these models have at least a limited range over which they can be reasonably used to represent either defect energy or nucleation rates; however, activation volume has become a confusing term used too readily to simultaneously describe the structure of a saddle point configuration, the stress dependence of all models, and, at least in theory, the actual stress dependence of the activation energy for deformation unit processes. In the current work we have used fully atomistic calculations of the activation energy for homogeneous dislocation nucleation as well as the atomistic saddle point configurations in order to provide a better understanding of the stress-dependant behavior of the activation volume.

In recent years there has been a particular focus on nanoindentation as a means of reaching the high stresses in a local region of perfect crystal required for homogeneous dislocation nucleation to dominate over the variety of heterogeneous processes that govern plasticity under most circumstances [8, 55-60]. The original observations of homogeneous dislocation loop nucleation under nanoindentation were performed using atomistic simulation where not only was the strain rate associated with deformation much higher than experimental rates but also the nanoindenter tip was in general smaller than experimentally accessible. Recent simulations utilizing a range of indenter sizes have indicated that homogeneous dislocation loop nucleation

occurs only for indenter tips smaller than the current state of the art experimentally and that a surface nucleation mechanism likely dominates in most experimental observations [58]. Further doubt has been cast on the feasibility of a homogeneous model by a series of high-temperature experiments which have predicted an activation volume associated with plasticity under a nanoindenter that is far too small over too wide a range of stresses to fit the standard conception of homogeneous dislocation loop nucleation [49, 50]. The experimental and computational work indicating the dominance of surface nucleation in nanoindentation is compelling; however, a significant concept in understanding the stress dependence for dislocation nucleation seems to have been overlooked. Although nanoindentation is capable of probing very small material volumes, the local region associated with nucleation of a defect is still significantly smaller. As the onset of defect nucleation is approached this smaller "local region" becomes mechanically unstable. The result is essentially a composite behavior where in the locality of the emerging defect the elastic constants approach zero while the surround "bulk" material maintains elastic stiffness commensurate to the applied indenter load. Activation volume for nanoindentation under an indenter load, P, is typically defined experimentally as dQ/dP, where Q is the activation energy. In terms of the stress at the emerging defect, τ, the activation volume can then be written as $dQ/dP = dQ/d\tau * d\tau/dP$. However, as mechanical instability drives the elastic constants towards zero $d\tau/dP$ approaches zero. The applied indenter load becomes relatively unable to load the "activate" region and as a result a measurement of dQ/dP ceases to be a conclusive indication of the stress dependence of the activation energy in the localized region. By directly calculating $dQ/d\tau$ via atomistic simulation in a relatively small volume of material we are able to capture the true stress dependence of the activation energy.

2.2 Reaction Pathways for Homogeneous Dislocation Loop Nucleation

Nudged elastic band (NEB) relaxations [21] of the pathway for homogeneous dislocation nucleation in Cu were performed using the embedded atom method (EAM) potential developed by Mishin et al [35] as the basis for calculation of both the total energy and atomic forces. An example of the full path is plotted in Figure 2-1 with each open circle representing the energy associated with a fully atomistic image configuration along the relaxed path. The 3N spatial degrees of freedom, associated with the N particles in each image configuration, are used as the degrees of freedom in our implementation of the NEB method. Distance between images in this 3N hyperspace, defined as $|\boldsymbol{R}_i - \boldsymbol{R}_{i-1}|$, then serves as the reaction coordinate for the description of the pathway for dislocation nucleation. In all cases the reaction coordinate is normalized by the total pathlength. The calculation of the reaction pathway is considered converged when the sum of the atomic forces perpendicular to the path is less than 0.005 eV/Å^2 for each 161,280 particle image configuration.

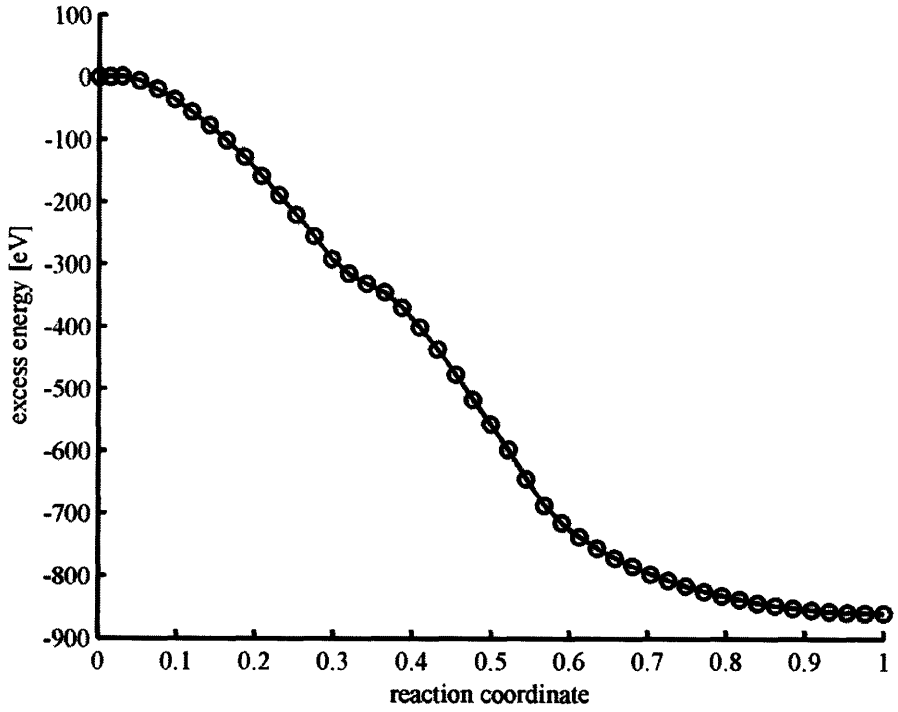

Figure 2-1: The excess energy (open circles) for a series of fully atomistic image configurations defines the energetic reaction pathways for homogeneous nucleation of a leading and trailing partial dislocation loop under simple shear.

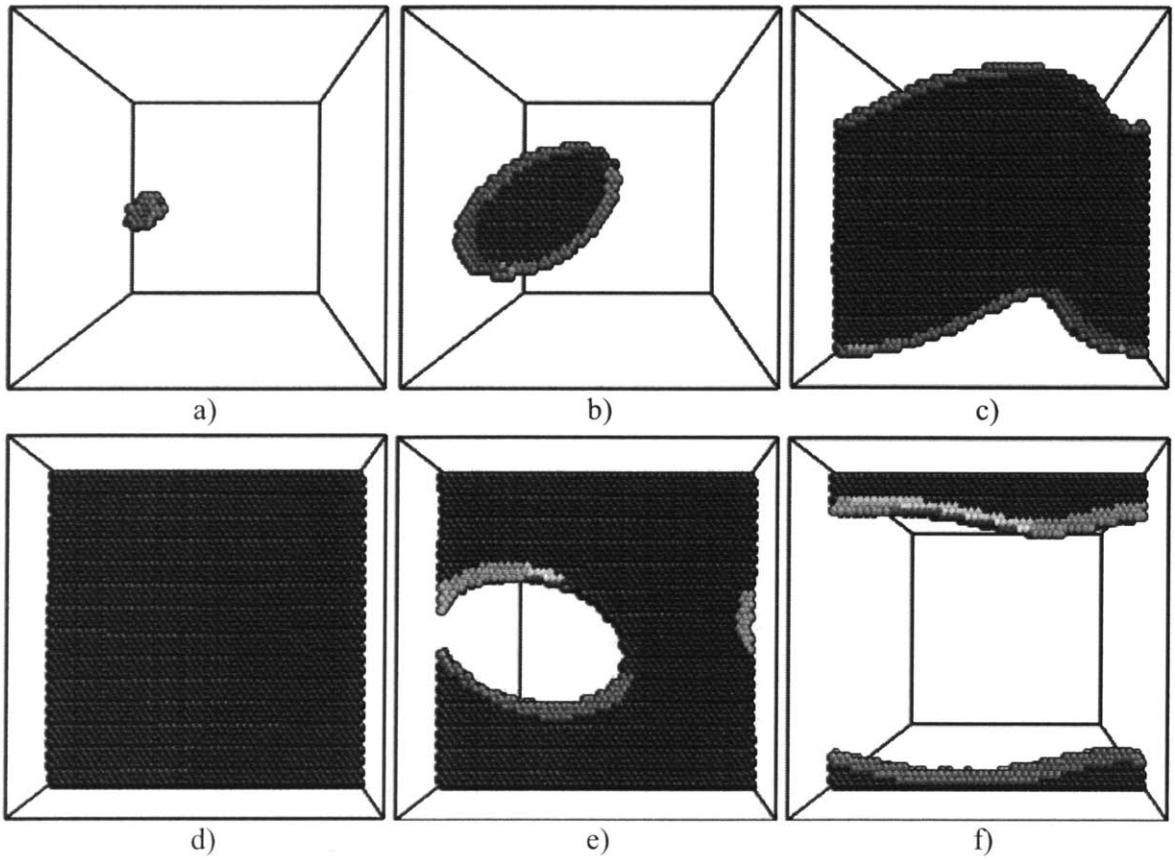

Figure 2-2: An initial leading partial dislocation is a) nucleated, b) grows, c) impinges on itself and d) annihilates to form a stacking fault from which e) a trailing partial dislocation is nucleated and eventually f) annihilates with itself through the periodic boundary. The stacking fault is colored in dark blue and all other colors correspond to the partial dislocations.

A series of representative snapshots from the full reaction pathway for homogeneous dislocation loop nucleation is presented in Figure 2-2. Particles are colored according to the centrosymmetry parameter [61] and those with centrosymmetry below 0.039 are removed in order to display the emerging defect. Those particles contributing to the stacking fault are colored in dark blue, centrosymmetry between 0.039 and 0.05, and all other colors correspond to the partial dislocations, centrosymmetry between 0.08 and 0.25. The observed behavior is as expected within the constraint of atomistic simulations with a periodic boundary condition. An initial leading partial dislocation is nucleated on a particular {111} slip plane (Figure 2-2a). The propagation of a partial dislocation leaves behind a stacking fault and a partial dislocation loop constitutes the boundary of the stacking fault within the slip plane (Figure 2-2b). Because of the periodic boundary, the partial dislocation loop impinges upon itself in Figure 2-2c to and

eventually the dislocation dipoles on opposite sides of the loop annihilate with one another to form a stacking fault across the entire slip plane in Figure 2-2d. As we move further along the path in Figure 2-1, the trailing partial dislocation shown in Figure 2-2e is nucleated and, following its leading counterpart, sweeps across the slip plane and through the periodic boundary to ultimately annihilate as well (Figure 2-2f). The specifics of the trailing partial dislocation nucleation process do not affect the activation barrier for homogeneous dislocation loop nucleation. However, in the interest of completeness, we have noted that the path depicted in Figure 2-2 holds until the applied stress decreases the partial dislocation splitting distance to below the width of the simulation cell and a trailing partial dislocation is nucleated prior to the formation of a complete stacking fault.

2.3 Stress-Dependent Activation

In Figure 2-3 the energy of each image along the pathway for homogeneous dislocation nucleation is shown as a function of reaction coordinate for a series of successively higher <112>{111} shear stresses, τ. The series of image configurations in the full reaction pathway corresponds to the nucleation of first a leading and then a trailing partial dislocation, and as such the activation barrier presented is associated with the initial nucleation of a leading partial dislocation loop encircling a stacking fault as outlined in Figure 2-2. However, two upgrades to the basic NEB formulation have been implemented for the stress-dependent calculations. First, we have utilized the climbing image implementation (CINEB) which allows a single image to search for the saddle point ensuring an accurate description of this critical configuration [62]. Secondly, a "free-end" algorithm [63], which allows for an unstable final configuration in the CINEB framework, was used for these calculations to both improve computational efficiency by reducing the required number of images and to improve the accuracy of the path description near the saddle point due to increased image density. In these CINEB calculations the <112>{111} shear strain is held constant, and the reported shear stress is taken to be that of the perfect crystal under the applied strain state. The pathways shown in Figure 2-3 exhibit the expected trend of decreasing activation barrier with increasing applied shear stress up to the critical stress, τ_{ath}. Although the deficiency of continuum descriptions for dislocation loops whose radii are on the

order of the burgers vector is well known [48], we note for completeness that considering a fully atomistic configuration eliminates the unphysical stable pre-nucleates observed in such continuum descriptions.

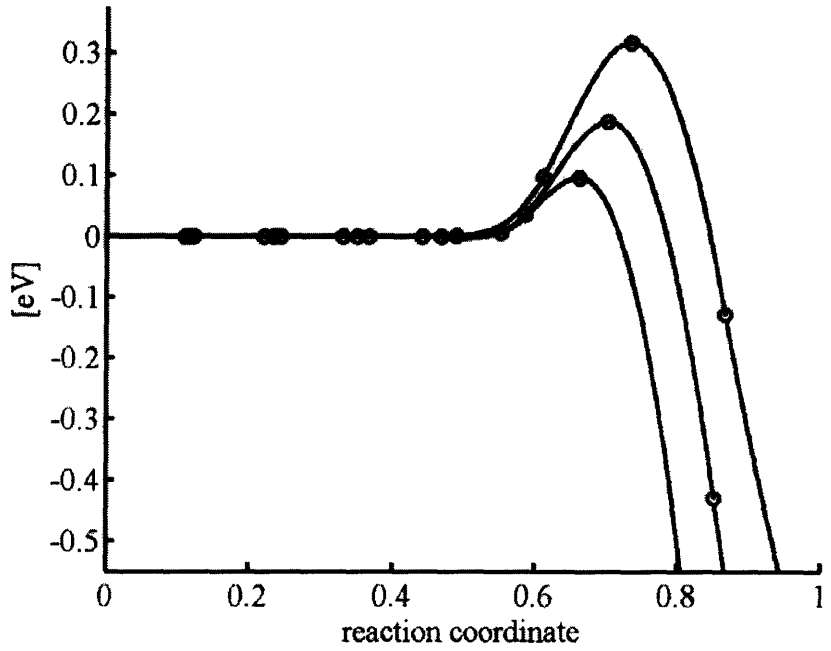

Figure 2-3: The configuration energy for a series of images along the minimum energy path for homogeneous partial dislocation loop nucleation in Cu is plotted under increasing applied <112>{111} shear stress. The open circles are the energies calculated from atomistic configurations along the pathway calculated by NEB method, and the dark line is a spline interpolation taken from the gradient of the energy landscape at the atomistic configurations.

The shear-stress dependent activation energy for homogeneous partial dislocation loop nucleation calculated using the CINEB method is plotted in Figure 2-4 (open circles). Within the framework of stress-mediated, thermally-activated processes the activation barrier which must be overcome by thermal fluctuation is a maximum at zero stress and decreases to zero at the athermal shear stress at which the dislocation will nucleate spontaneously. The activation barrier should therefore fit the following form [46, 52, 64, 65]:

$$Q = Q_o(1 - \tau / \tau_{ath})^{\alpha} \qquad (2.1)$$

where increasing the applied shear stress, τ, decreases the magnitude of the activation barrier. Q_o is the activation energy at $\tau = 0$, and the exponent, α, controls the rate at which the applied shear stress decreases the activation energy.

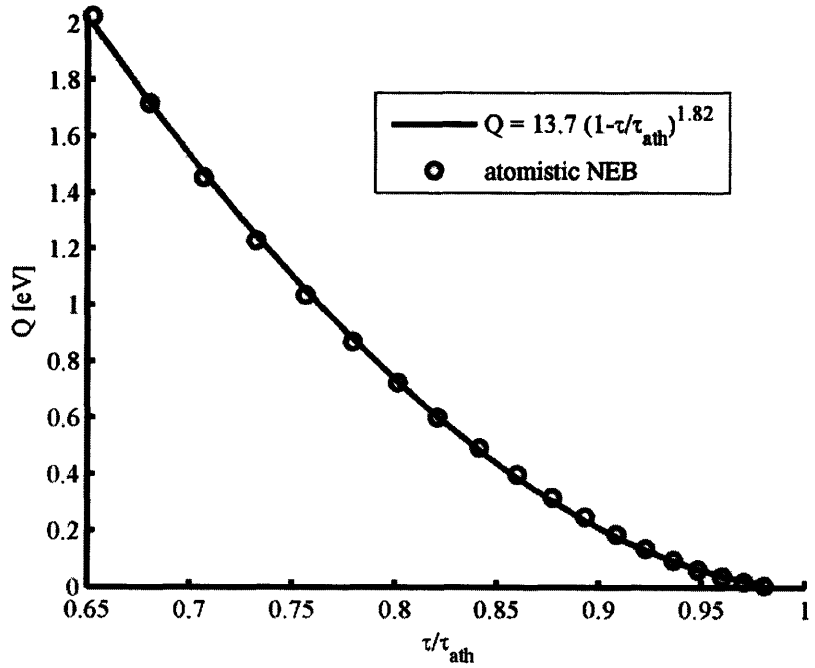

Figure 2-4: The stress-dependent activation energy for homogeneous dislocation loop nucleation was calculated using the CINEB method (open circles) and fit via the least-square method to Equation 2.1 (solid black line) in order to obtain Q_o and α.

A least-squares fit of the $Q(\tau)$ data taken from the CINEB simulations to the parameters Q_o and α in Equation 2.1 yield values of 13.7 and 1.82 respectively (Figure 2-4 solid curve). The choice of τ_{ath} has a non-trivial effect on the fitting parameters and as a consequence has been validated in two ways. First, within the framework of the least squares fitting procedure for $Q(\tau)$, $\tau_{ath} = 3.78$ minimizes the R^2 value for the full data set and can therefore be taken as the athermal stress indicated by the NEB methodology. Secondly, MD simulations at a temperature of 0.0001 K and a series of constant <112>{111} simple shear were performed. In all cases the crystal lattice was stable for stresses below 3.771 GPa and nucleated a dislocation for stresses above 3.7718 GPa. The evolution of the configurational energy over time for representative runs near τ_{ath} is shown in Figure 2-5. The MD simulations serve as a sanity check for the athermal stress indicated by the least-squares fitting procedure. Throughout the thesis, τ_{ath} for homogeneous dislocation loop nucleation is taken to be 3.78 GPa as indicated by the NEB fitting procedure.

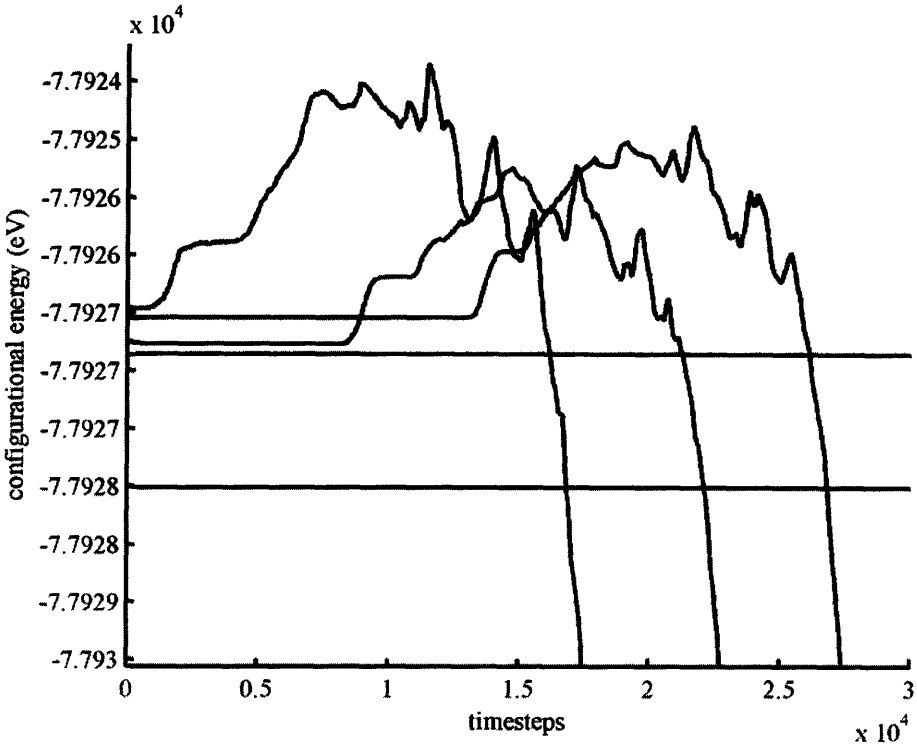

Figure 2-5: The evolution of the configurational energy for five MD simulations at 0.0001 K of a perfect FCC Cu lattice under <112>{111} simple shear at τ = 3.7683, 3.7702, 3.771, 3.7718 and 3.7725 GPa in order of increasing initial energy indicates that τ_{ath} falls between 3.771 and 3.7718 GPa.

The periodic boundary condition raises a particular question of convergence for our NEB simulations of activation energy. Our actual system is a periodic, three-dimensional array of shear defects emerging simultaneously under the applied shear stress. Figure 2-2 shows the annihilation of the partial dislocation loops with these periodic image configurations. The presence of these periodic images lowers the energy associated with the emerging defect because the far-reaching elastic field surrounding dislocations of opposite sense cancel one another. In order to comment on the convergence of our calculations w.r.t the simulation cell, we have calculated the activation energy for homogeneous dislocation loop nucleation via CINEB simulations in cells containing 20,160 particles at three applied <112>{111} shear stresses. These activation energies are plotted in Figure 2-6 (open triangles) along with the previously reported activation energies calculated with the 161,280 particle simulation cell (open circles).

The periodic distance associated with the smaller simulation cell is one-half that of the larger cell (~12.5 nm versus 6.2 nm). At 0.8 τ_{ath} the difference in activation energy is about 0.06 eV or roughly 10% of the activation energy calculated using the larger cell. The magnitude of the difference decreases as τ approaches τ_{ath}, but the percentage difference grows to almost 20% at 0.94 τ_{ath}. However, these simulations indicate a reasonable numerical agreement between the two cell sizes. We have used the larger cell throughout the current work with the goal of limiting, to the extent possible within the bounds of computation resources, the effects of the elastic interactions through the periodic boundary.

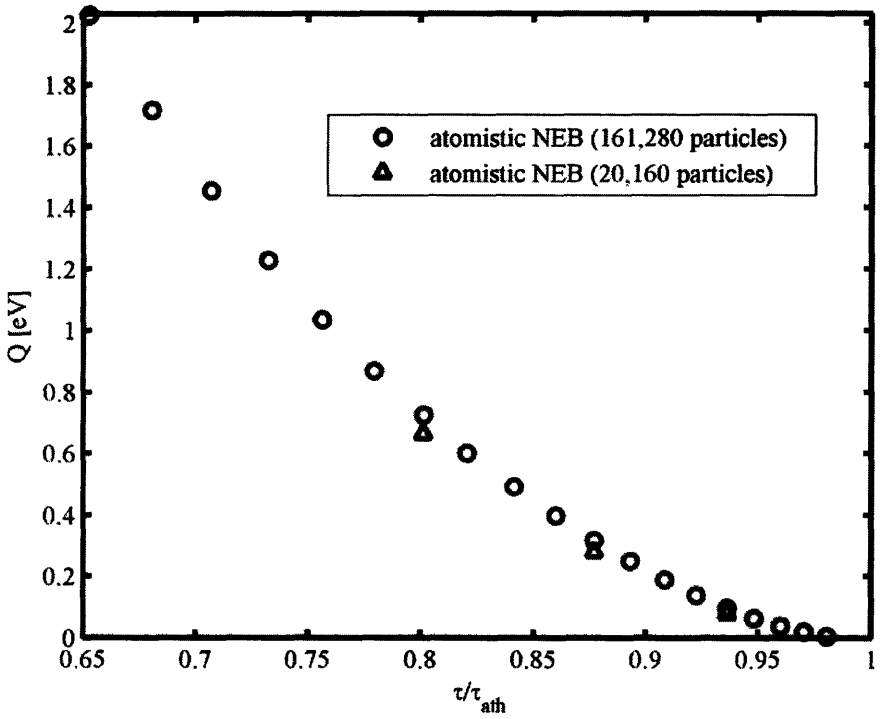

Figure 2-6: The activation energy versus applied shear stress shows reasonable agreement for two different simulation cell sizes (~12.5 nm edge lengths versus ~6.2 nm edge lengths).

The first point of reference for discussion of the magnitude of the activation energy for homogeneous dislocation nucleation is a discussion by A. H. Cottrell in the 1950's [45] which states that thermally activated nucleation is impossible for anything but stresses very near the athermal stress. Although the declaration was based on a simple model with limited stress dependent behavior, the prevailing concept that homogeneous dislocation loop nucleation is kinetically infeasible has persisted. A more recent calculation by Xu and Argon predicts the

activation energy for Cu at τ/τ_{ath} = 0.5 to be 16 eV [44]. Based on the fit of atomistic data to Equation 2.1 we have calculated the activation energy to be 3.9 eV at the same level of normalized shear stress. The disparity in activation energies highlights the usefulness of the generic reaction coordinate employed in our atomistic CINEB calculations. While formulating a continuum description of a specific defect process requires a researcher to make specific choices to include various degrees of freedom, the atomistic NEB allows the system to make those choices based on the energy landscape. There are several recent examples where additional relaxation from fully atomistic descriptions of dislocation nucleation and propagation has provided as much as an order of magnitude decrease in the activation energy compared to continuum energy descriptions [20, 66]. The differences in activation energies have been attributed to the increased degrees of freedom associated with the atomistic simulation. In particular the work by Xu and Argon ignores takes the shear modulus to be constant even as the applied shear stress approaches the athermal stress. The atomistic calculations can be seen as an indication of the possible routes towards improvement of such continuum descriptions for defect processes.

2.4 Structural Regimes for Saddle-point Configurations

Our goal is to provide insight into the stress-dependence of homogeneous dislocation nucleation and the validity of our current definitions of activation volume. However, some immediate insight can be gleaned from the simple observation that three separate regimes exist for the general structure of the saddle point configuration as the applied stress in the system is increased. A representative atomistic configuration from each regime is given in Figure 2-7 where particles are colored according to the centrosymmetry parameter.

First at the lowest values of applied stress (less than 0.6 τ_{ath}) the saddle point configuration is a partial dislocation loop (Figure 2-7a) the size of which decreases with increasing applied stress. In the first regime the activation energy is above 2.0 eV and thermal fluctuations are unlikely to result in dislocation nucleation. The probability of a random thermal fluctuation resulting in a fully formed partial dislocation loop should realistically be very low which makes the high

activation energy in this regime satisfying from a purely intuitive standpoint. The theoretical difficulty of nucleating such an extended defect has historically been cited as indication that homogeneous nucleation was not feasible [45]. However, a fully formed dislocation loop is not the critical configuration above 0.6 τ_{ath}. In the range of 0.6 $\tau_{ath} < \tau < 0.99\ \tau_{ath}$ the saddle point configurations take the form of in-plane shear perturbations whose maximum displacement is below b_p and as such do not constitute fully-formed dislocation loops. The representative configuration in Figure 2-7b shows a continuous degrease in the centrosymmetry from a peak of 3.8×10^{-3} at the center of the elliptical defect to a minimum of 8.2×10^{-4}. As the stress is increased in this second regime the magnitude of the maximum centrosymmetry decreases; however, the size of this elliptical defect remains relatively constant until very near the athermal stress where some spreading is observed.

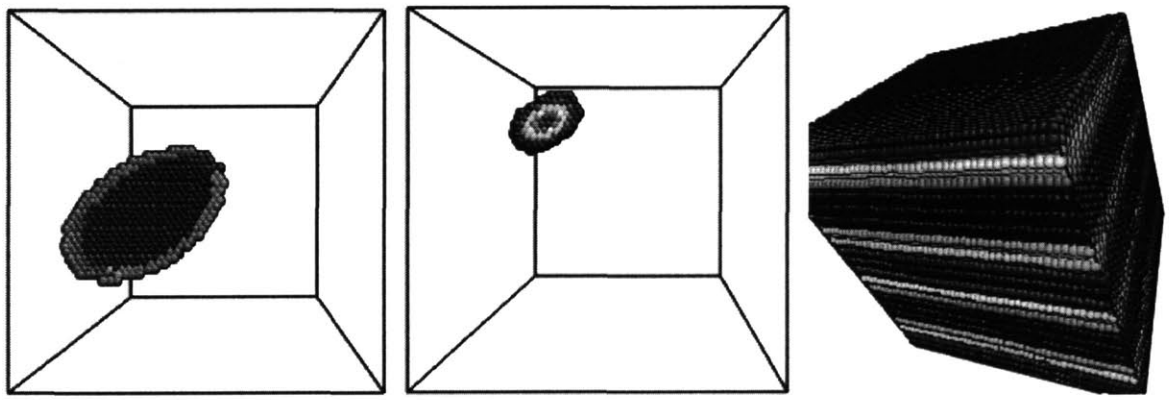

a) b) c)

Figure 2-7: In order of increasing applied stress, the saddle point configuration takes the form of a) a partial dislocation loop, b) an in-plane shear perturbation, and c) a shear wave normal to the slip plane. Configurations representing the three observed structural saddle point regimes are colored here according to the centrosymmetry parameter with ranges of a) 0.039 to 0.25, b) 8.2×10^{-4} to 3.8×10^{-3} and c) 6×10^{-17} to 1.3×10^{-12}.

The last regime at the highest values of applied shear stress very near to τ_{ath} corresponds to shear perturbations not localized to the eventually activated slip plane (or to any other single slip plane). The configurations associated with this regime show breaks in crystal symmetry spread throughout the crystal as either a shear wave normal to the slip plane or some intermediary stage as these shear waves collapse and localize to the activated slip plane (Figure 2-7c). Practically,

the last regime would be difficult to observe experimentally as the saddle points are roughly phonon modes which always exist in a crystal at temperature. The range of stress at which thermal activation of homogeneous dislocation nucleation is feasible (say with activation energy below 1eV) extends below $0.75\tau_{ath}$ including the second and third saddle point regimes. From a structural standpoint, stresses at which the eventual formation of a dislocation loop within a crystalline lattice is kinetically viable are possible because the existence of in-plane shear perturbations as saddle-point configurations removes the requirement of thermally inducing a fully formed dislocation loop.

The value of the exponent in Equation 2.1 has been the subject of some recent debate. In particular Cahn et al have shown $\alpha = 1.5$ for stress-dependent processes defined by a single degree of freedom or reaction coordinate and broadly applied the analysis to dislocation nucleation [46]. However, even a fully formed partial dislocation loop is not completely described by the area swept out or the radius of the defect as the shear displacement within the stacking fault is not constant at b_p for a real defect. Likewise, in the second saddle point regime where the maximum shear displacement exhibits the most significant change with applied stress, the area swept out by the in-plane shear perturbation is not constant. The more complicated shear stress dependence of the saddle point may be captured in the atomistically calculated $\alpha = 1.82$. The assumption of a single reaction coordinate does not fully hold for homogeneous dislocation loop nucleation particularly in the second saddle point regime near the critical stress where thermal activation is most energetically feasible.

2.5 Activation Volume

The fully-atomistic CINEB calculations intrinsically include the full stress-dependence of the nucleation processes. However, the various continuum models in use over the past few decades have considered various subsets of the stress-dependencies which exist for dislocation nucleation. Over time the definition for activation volume has become synonymous with the most popular of these models. In particular the stress dependence of the Gibb's free energy, G, for a dislocation loop in the classic formulation is limited to a term for the work required to

create an inelastic shear strain within the area swept out by the dislocation against a constant shear stress [45, 48]. The work term is give by:

$$W = V\varepsilon\tau = d_{<111>} ac\pi \cdot \frac{b_p}{d_{<111>}} \cdot \tau \tag{2.2}$$

where, for an elliptical partial dislocation loop with radii a and c, V is the volume in which the work is performed, ε is the shear strain in the slip plane and τ is the applied shear stress. The interplanar spacing in the <111> direction, $d_{<111>}$, cancels out and the purely structural definition of activation volume taken from the Gibb's free energy, which has found widespread use, is then given by:

$$\Omega' \equiv -\frac{\partial \Delta G}{\partial \tau} = \frac{\partial W}{\partial \tau} = ac\pi \cdot b_p \tag{2.3}$$

As discussed previously the structurally-defined activation volume, Ω', is in this formulation the magnitude of the shear displacement associated with a dislocation, multiplied by the area swept out by the dislocation loop. Because real dislocations are not discontinuous displacement profiles as assumed by Equations 2.2 and 2.3, standard practice in determining Ω' is to define the area within the slip plane with a displacement greater than some fraction of the maximum displacement as the area swept out by the dislocation and to multiply this by the maximum displacement, b_p in the case of a partial dislocation loop. For a fully formed partial dislocation, Equation 2.3 is then a reasonable approximation of this structural definition of activation volume. A more rigorous approach is to integrate the inelastic displacement across the slip plane, $u(x,y)$, with respect to the in-plane spatial dimensions, x and y.

$$\Omega' = \iint u(x, y)\, dxdy \tag{2.4}$$

Equation 2.4 provides a coherent structural definition of activation volume applicable for any in-plane shear perturbation or defect.

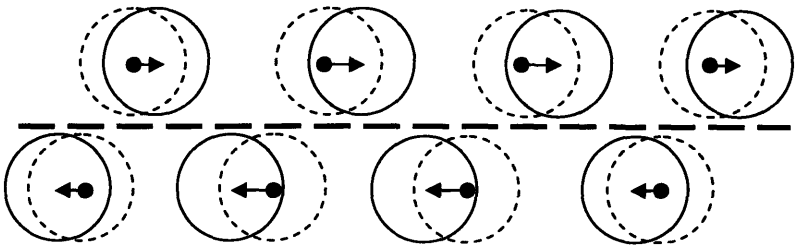

Figure 2-8: A schematic of the atomic displacements (arrows) adjacent to a slip plane (bold dashed line) illustrates that the atomic displacements cannot be used to directly calculate the displacement across the slip plane. In the picture, dashed circles represent the reference FCC lattice while the solid circles are the displaced particles.

In order to calculate the structural activation volume as defined by Equation 2.4, we must first calculate ***u(x,y)*** for each atomistic saddle point configuration calculated using the CINEB method. The slip plane is represented in Figure 2-8 by the bold dashed line between the two schematic {111} planes. The displacement in the slip plane is defined as the relative change in the position of the atomic planes above and below any point in the slip plane. In general for an atomistic simulation, each of the particles has a unique displacement within the atomic plane which is represented in Figure 2-8 as an arrow whose length indicates the magnitude of the particle displacement. However, the discrete atomic positions cannot be used to directly calculate ***u(x,y)*** in the slip plane because particles are rarely, if ever, found along the same <111> normal due to the stacking order of {111} planes in Cu's FCC lattice. To overcome the difficulties posed by the atomic lattice, we have fit a smooth displacement profile to the atomistic data for both {111} planes adjacent to the slip plane. With these two continuous profiles we can calculate the shear displacement across the slip plane for a finely spaced mesh of points in the slip plane. Examples of the resulting displacement profiles for a fully formed partial dislocation loop and for an in-plane shear perturbation are shown in Figure 2-9.

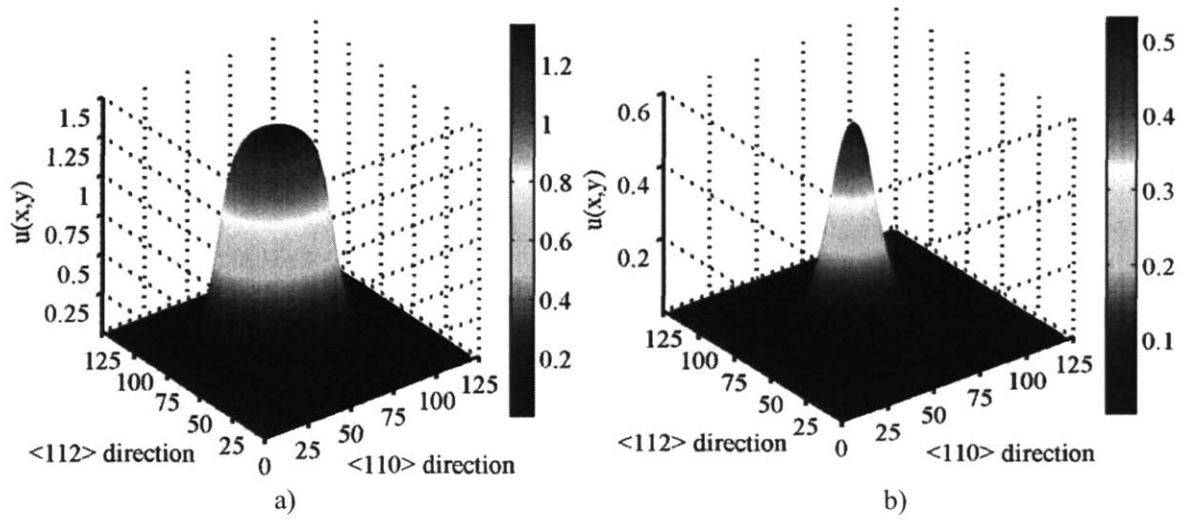

Figure 2-9: The inelastic displacement across the slip plane for a) a partial dislocation loop and b) and in-plane shear perturbation which are calculated by fitting displacements to a set of positions in the slip plane in order to calculate the relative displacement between the two planes.

Having calculated the displacement profile in the slip plane, application of Equations 2.3 and 2.4 to the displacement profiles of the CINEB-derived atomic configurations represents two methods for calculating the structurally defined activation volume. The area swept out by the dislocation loop is calculated by performing a least squares fit of the equation for an ellipse to the points in a displacement profile such as those in Figure 2-9 which fall between 0.5 $\boldsymbol{u_{max}}\pm 0.01\boldsymbol{u_{max}}$, where $\boldsymbol{u_{max}}$ is the maximum inelastic shear displacement in the slip plane. Adopting the convention of Equation 2.3 for the case of an in-plane shear perturbation, the structurally-defined activation volume is then calculated as:

$$\Omega' = ac\pi \cdot u_{\max} \tag{2.5}$$

Following Equation 2.4 the numerical integral of $\boldsymbol{u(x,y)}$ is taken as the displacement at a series of grid-points in the slip plane, which are calculated from inelastic displacement profiles such as those shown in Figure 2-9 multiplied by the area associated with each point. Convergence of the integral was reached for a square mesh 0.31 Å on a side. Two dimensional illustrations of the two methods for calculating $\boldsymbol{\Omega'}$ are shown in Figure 2-10. In principle the simplified method in Figure 2-10a should be a reasonable approximation of the numerical integral in Figure 2.10b. The method in Figure 2-10a is however particularly suited to the description of the extended

dislocation loops for which it was initially adopted since the volume under the displacement profile for a dislocation loop is dominated by the displacement plateau associated with the stacking fault.

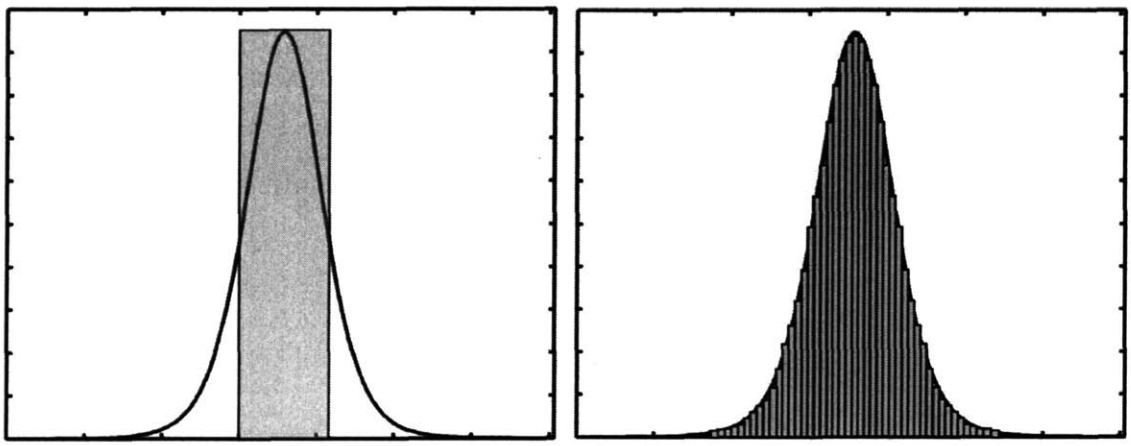

a) b)

Figure 2-10: The structurally defined activation volume for an in-plane shear perturbation is calculated via two methods which are schematically represented in two-dimensions. The volume under the displacement curve is approximated in a) as the length swept out multiplied by the maximum of the profile. A more refined numerical approximation in b) takes a similar approach but divide the profile into a series of small line lengths each with an associated displacement.

So far we have focused on one of the most commonly used definitions of activation volume which is based on the structure of the critical defect. However, the rigorous definition of the activation volume continues to be the derivative of the activation energy (plotted in Figure 2-4) with respect to the applied shear stress. The activation volume calculated using Equations 2.4 and 2.5 and as the derivative of Equation 2.1 has been plotted as a function of normalized shear stress in Figure 2-11. The form of Equation 2.1 constrains the derivative to zero at $\tau = \tau_{ath}$, and the saddle point coincides with the initial NEB configuration at $\tau = \tau_{ath}$ so that the structural definitions of activation volume are also equal to zero. However, the trends observed in the two descriptions are very different.

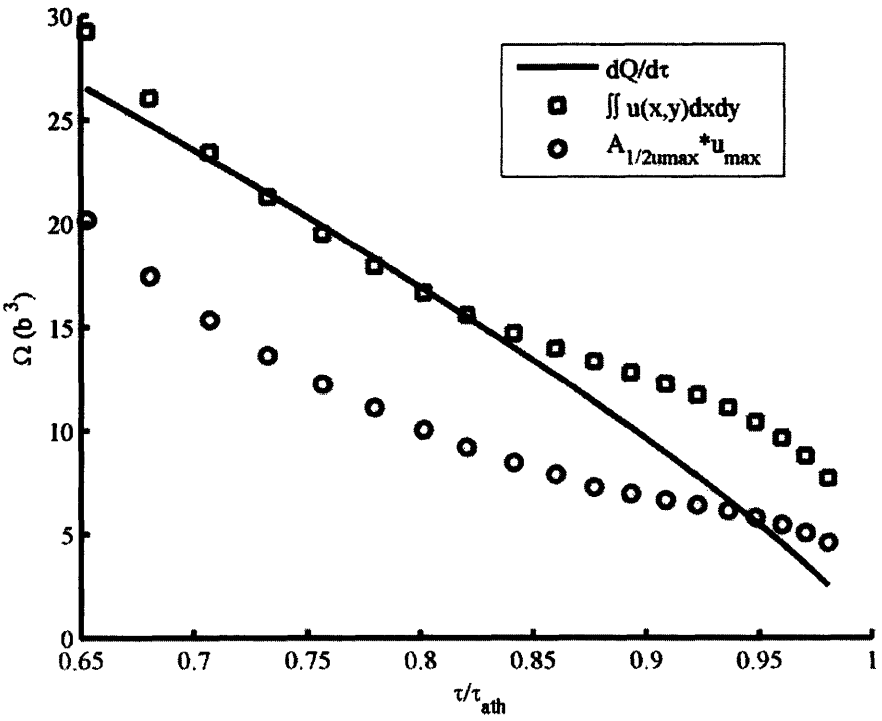

Figure 2-11: The activation volume for homogeneous dislocation loop nucleation calculated using three definitions: the integral of the in-plane shear displacement (open squares), the area swept out by half the peak displacement multiplied the peak displacement (open circles), and the derivative of activation energy w.r.t applied shear stress (solid line) is plotted as a function of the normalized <112>{111}shear stress in the system.

As discussed previously for shear stresses in the range of 0.6 $\tau_{ath} < \tau < 0.99\ \tau_{ath}$, the saddle point configurations take the form of in-plane shear perturbations whose maximum displacement is below $|\boldsymbol{b}_p|$, and as such the configurations do not constitute fully-formed dislocation loops. Above 0.82 τ_{ath}, corresponding to an activation energy of around 0.5 eV, the maximum displacement of the in-plane shear perturbation is actually below 0.5 $|\boldsymbol{b}_p|$ indicating that in the simplest perspective the saddle points for stresses of 0.82 $\tau_{ath} < \tau < \tau_{ath}$ are defects where no single particle has even broken its local FCC symmetry. Although the maximum displacement of the saddle point configuration decreases as the shear stress is increased, the shear perturbation begins to spread out in the plane. At stresses above 3.2 GPa the area contributing to Ω', that swept out by some infinitesimal shear displacement, increases which slows down the rate at which the structurally defined activation volume decreases as the shear stress approaches τ_{ath}.

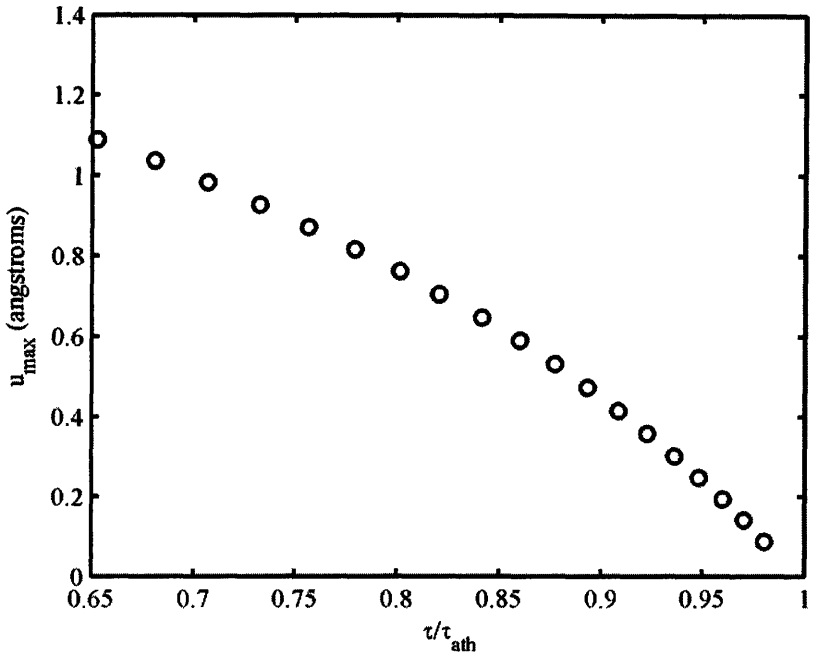

Figure 2-12: The maximum inelastic shear displacement decreases to zero at the athermal stress.

The spreading out of the shear perturbation in the slip plane has been observed although not discussed by Argon and Xu in their study using the boundary integral method [44]. The maximum inelastic shear displacement, u_{max}, in Figure 2-12 decreases to zero as the applied shear stress increases. However the area swept out by the shear displacement reaches a minimum at $0.85\tau_{ath}$ in Figure 2-13 and then increases seemingly towards infinity as τ approaches τ_{ath}. The increased area swept out by the critical defect as τ approaches τ_{ath} is reminiscent of the classical work by Cahn and Hilliard on second phase nucleation in a two component system [67]. They observe simultaneous decrease in maximum concentration and increase in the radius of the critical second-phase nucleate for concentrations approaching the saturation limit where a second phase will nucleate spontaneously. The correlation suggests a framework for discussion of the observed nucleation phenomenon for dislocations. The critical configuration in nucleation theory can be described along a spectrum bound by two extremes. On one end nucleates are taken to be small with a sharp interface separating a large fluctuation in the property of interest, in our work a small dislocation loop falls into this category. As the stress approaches τ_{ath} we observe a switch to a critical fluctuation in shear displacement which is spread out in the plane but whose

maximum displacement is relatively small. These two extremes are described as infinitesimal in degree but large in extent and large in degree but small in extent [67].

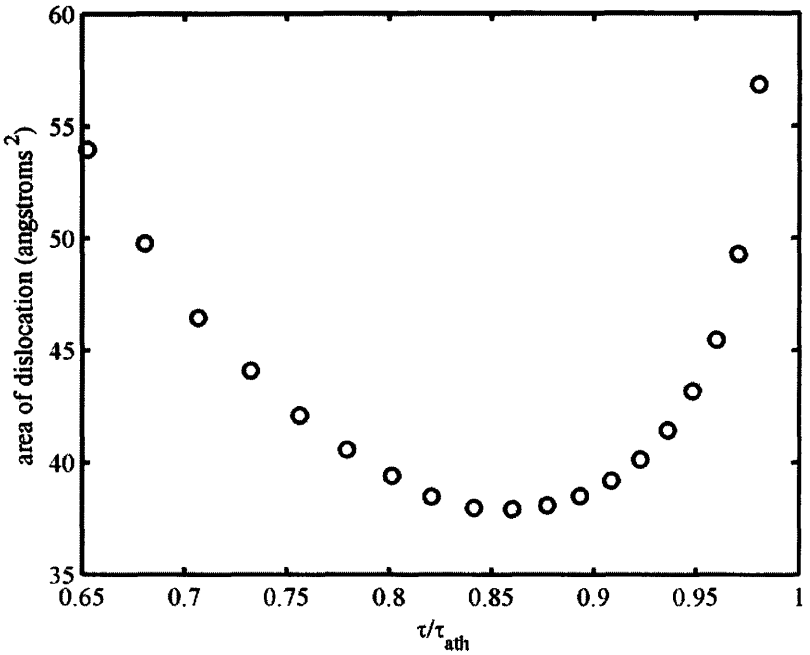

Figure 2-13: The area swept out by the dislocation, defined here as the portion of the slip plane with shear displacement > 0.003Å, decreases with increasing applied shear stress until near the athermal stress where the dislocation begins to spread in the slip plane.

A dislocation core's width is known to increase with decreasing elastic constants. We have observed the same behavior as τ approaches τ_{ath} and the elastic constants go to zero locally for an in-plane shear perturbation, which can be thought of as a combination of dislocations with displacements less than b_p. The discrepancy in the structural and analytical definitions of activation volume arises because in general the stress dependence of Q is not fully contained in the work term given by Equation 2.2 as is often assumed for studies of dislocation nucleation. The most promising path for further exploration is the consideration of additional local atomic relaxations associated with the emerging defect. We have discussed only the structurally defined activation volume associated with the inelastic shear displacement within the slip plane while dilation of the slip plane also occurs. We could also extend our analysis to additional planes above and below the dominant shear defect although this is likely at most a minor contributor to the stress dependence of the activation energy.

2.6 Conclusions

Near critical thresholds most thermally-activated defect processes in plasticity cannot be considered as a function of a single parameter. Even a relatively simple process such as homogeneous dislocation loop nucleation requires consideration of both a loop radius and a maximum shear displacement. More generality, although perhaps not much more rigor, can be found by considering the 3N degrees of freedom associated with the atomic positions in the local material volume of the emerging defect. We have performed atomistic calculations of the activation energy and saddle point configurations for homogeneous dislocation loop nucleation using the CINEB method. With full atomistic degrees of freedom, we have observed a higher exponent for the stress-dependent driving force for dislocation nucleation than previously expected. With atomistic CINEB calculations we have found the exponent of the stress-dependent driving force for dislocation nucleation to be 1.82. While the derivation of a 3/2 model is sound, it seems unlikely that it should strictly apply in the regime feasible for thermal activation of dislocation nucleation as the model assumes a single degree of freedom.

Homogeneous dislocation nucleation is typically ignored as a possible defect mechanism because of the assumed large activation volume associated with creating a fully formed dislocation loop. Our atomistic simulations have shown that, although the coordinated motion of one hundred or more atoms is required to nucleate a dislocation loop, for a large range of shear stresses below τ_{ath} the local shear displacement associated with most atoms is very small relative to the partial Burger's vector. The energetic penalty for production of the in-plane shear perturbations found to play the role of saddle point configuration is relatively small for stresses above 0.6 τ_{ath} compared to the energy required to produce a dislocation loop incorporating a similar number of particles. Consequently, activation energies below 1eV, which are reasonably accessible to thermal fluctuation, exist for stresses above 0.75 τ_{ath}. Low activation energy, due to smaller than expect contribution from the particles involved, lends credence to the idea that homogeneously nucleated dislocation loops could be responsible for plasticity in idealized conditions such as those available under nanoindentation. Here we have shown that a large range of stresses exist for which the process of homogeneous dislocation nucleation is kinetically viable. Competition with various heterogeneous processes will be discussed in chapter five.

The structure of the critical defect at the saddle point is typically purported to contain complete information regarding the stress-dependence for thermally activated defect processes within its shear displacement profile. In general the language associated with defect nucleation and propagation was laid out long before researchers had access to full atomistic information regarding non-equilibrium defect structures. The original models considered only the shear strain and the volume associated with the saddle point defect. By calculating both the derivative of the stress-dependent activation energy and the structurally-defined activation volume we have shown that the activation volume is not a simple quantification of the shear displacement of the saddle point configuration. The two most common definitions of activation volume show quantitative agreement for a limited range of stresses but exhibit qualitatively different stress-dependent behavior. We have shown using atomistic CINEB calculations with empirical potentials that the commonly used structural definitions are insufficient to fully explain the behavior of the activation volume. However, for atomistic simulation with empirical potentials the energy of the system is directly related to the structural configuration. As a consequence the energy of the saddle point must be definable in terms of atomic relaxations in the vicinity of the defect.

The stress-dependence of the structurally defined activation volume diverges from the expected behavior in part because of the spreading of in-plane shear perturbations with maximum displacements less than the Burger's vector. As a system becomes saturated, whether in applied shear stress, solute concentration, or likely many other thermodynamic driving forces for nucleation phenomenon, a transition occurs in the generic description of the critical configuration. In homogeneous dislocation loop nucleation as the stress approaches the athermal stress, we observe that although the maximum shear displacement decreases continuously, the extent of the defect dramatically increases. Very near the athermal stress saddle point configurations not localized to a single slip plane suggest behavior similar to spinodal decomposition where a phonon mode plays the role of long-wavelength fluctuation. The behavior of the saddle point configuration for dislocation nucleation as the system approaches the athermal stress suggests that a transition from a discrete critical nucleate, large in degree but small in extent to a diffuse critical nucleate small in degree but large in extent should be

generically observed as thermally activated nucleation phenomenon approach the athermal limit of their driving force.

Chapter 3

Origins of Stress Dependence for Activation

3.1 Introduction

In the previous chapter we presented an atomistic study of homogeneous dislocation loop nucleation with the goal of illuminating the stress dependence of a classic thermally-activated deformation unit process. The atomistic simulations intrinsically incorporate all of the stress-dependent behavior captured by the underlying empirical potential. However, the various factors contributing to the decrease in activation energy with increase applied shear stress cannot be extracted from one another. In general the formulation of empirical potentials does not easily allow for both accurate energetic description and the ability to performed parameterized studies. When all of the stress-dependence is included in a rigorous way we do not have straight-forward access to remove or alter the various contributors to stress-mediated behavior. Our interest in the current chapter is to use a simpler model, over which we can exercise more control, to pinpoint the physical origins of the stress-mediation for the test case of homogeneous dislocation nucleation.

Arguably the most common descriptive model of a dislocation was developed by Peierls [68] and Nabarro [69] in the 1940's. The basis of the Peierls-Nabarro (PN) model is the description of a dislocation as a shear displacement profile localized to a slip plane coupled to two separate elastic bodies, one above and one below the slip plane. The energy or forces associated with a dislocation, or more generally a displacement profile, can then be formulated as the sum of two contributions: the first due directly to the lattice disruption caused by the misfit across the slip

plane and the second due to the change in the misfit within the slip plane resulting in elastic strain in the materials above and below the slip plane. For our purposes the energy associated with an arbitrary in-plane shear displacement, $\boldsymbol{u}$, is then described in general by:

$$E_{disl} = E_{misfit}[u(x, y)] + E_{body}[\nabla u(x, y)] \tag{3.1}$$

where $\boldsymbol{x}$ and $\boldsymbol{y}$ define a unique position in the slip plane.

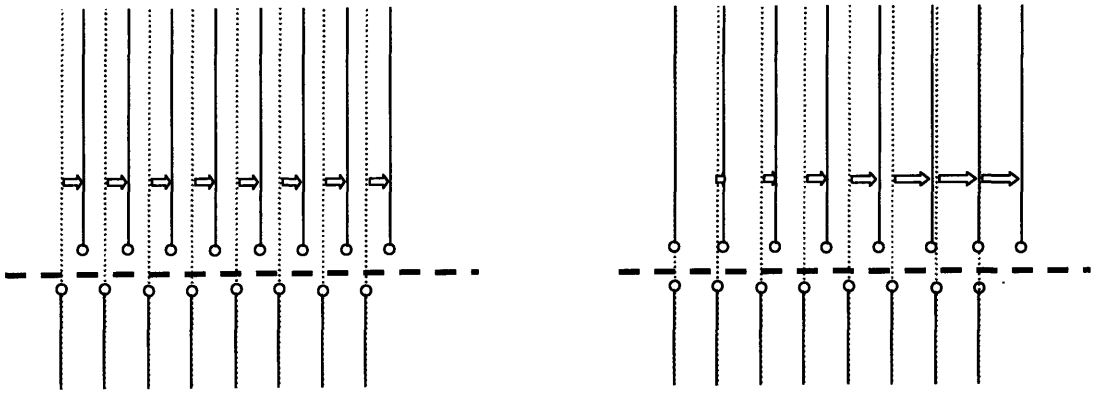

a) b)

Figure 3-1: Schematic representation of the energetic contributions to the PN model of a dislocation. The slip plane is represented by the horizontal dashed line, the vertical dotted lines correspond to the original "lattice" and the magnitude of the misfit across the slip plane is given by the arrows. In a) the constant displacement in the elastic body above the slip plane yields only misfit energy; whereas the gradient in the displacement profile in b) disrupts the lattice above the slip plane leading to an additional elastic energy term.

The misfit and elastic contributions are depicted schematically in Figure 3-1 where the bold dashed line represents the slip plane and the arrows represent the magnitude of the displacement between the reference crystal (dotted lines) and the current configurations (solid lines). If the displacement in the slip plane is constant, as in Figure 3-1a, the two elastic bodies move rigidly relative to one another, and the only contribution to the energy of the defect comes from the interaction of particles across the slip plane which is exactly the misfit energy term. However, when the displacement profile is not constant in the slip plane, the elastic bodies, represented by vertical lines in Figure 3-1b are strained in order to accommodate the gradient in displacement

profile. The second term then constitutes a contribution due to the interaction of particles within the same elastic body.

Various formulations of the PN model have been used extensively to describe the nucleation and propagation of dislocations [44, 70-74] and particularly in discussion of the structure of dislocation cores [75, 76]. Our goal here is not an improvement to the PN model but to take a well known formalism for the purpose of discussing the contributions to the stress-dependent behavior for homogeneous dislocation nucleation.

3.2 Peierls-Nabarro Model

Although the qualitative description of the PN model has remained relatively constant much progress has been made in calculation of the misfit energy and elastic response terms and in our ability to couple the two. In particular the original sinusoidal approximation for the misfit energy has been replaced with the concept of the generalized stacking fault energy (GSFE) [77, 78]. The GSFE is the energy associated with displacement of two rigid bodies relative to one another in a particular slip system. The application of robust empirical potentials [43, 79] or even ab-initio calculations [80, 81] currently allows for a very accurate depiction of the energetic penalty associated with the misfit in a slip plane.

Furthermore a variational formulation of the entire PN energy model for a line dislocation has been proposed to more accurately couple the energy due to the elastic body and the misfit energy [75]. The governing equation for this formulation is given below:

$$E_{disl} = \int \gamma[u(x)]dx - \kappa \iint \frac{du(x)}{dx}\frac{du(x')}{dx'} \ln|x - x'|\, dxdx' \qquad (3.2)$$

where $\boldsymbol{K}$ is a generic function of the elastic constants depending on the specific combination of edge and screw character which exists in the dislocation, $\boldsymbol{\gamma[u(x)]}$ is the generalized stacking fault energy and $\ln|x\text{-}x'|$ is the elastic energy kernel for the interaction of the gradient of the displacement at the two points whose positions are given by $\boldsymbol{x}$ and $\boldsymbol{x'}$. The energy functional is then discretized at a series of nodal points to yield:

$$E_{disl} = \Delta x \sum_i \gamma[u(x_i)] + \sum_{ij} \frac{du(x_i)}{dx_i} \frac{du(x_j)}{dx_j} X_{ij} \tag{3.3}$$

where X_{ij} is the discretized function describing the elastic interactions between nodes i and j based on their relative positions. The details of this formulation are presented elsewhere[75, 81], but Equations 3.2 and 3.3 are included here as the roadmap for a similar formulation of the PN model for a circular dislocation loop.

Application of the misfit energy term in Equation 3.2 to a circular dislocation or shear perturbation is straightforward. In general the misfit energy depends only on ***u(x,y)*** and is normalized by the area swept out by the displacement profile. We must also consider the applied shear stress, τ, transmitted through the elastic bodies. Taking into account the radial symmetry of the displacement profile in our formulation the misfit energy and applied shear stress terms are as follows:

$$E_o[u(r)] = \int_A [\gamma[u(r)] - \tau\, u(r)] \tag{3.4}$$

where each term is taken as the integral over the area, A, in the slip plane. The integral is easily transformed into a discrete formulation where $\mathbf{r_i}$ is the radius of node ***i*** and $\boldsymbol{\Delta r}$ is the width of the circular slice in the slip plane associated with each node:

$$E_o = 2\pi\Delta r \sum_i r_i(\gamma[u(r_i)] - \tau\, u(r_i)) \tag{3.5}$$

The elastic interaction kernel is a much more difficult problem but one that has received much attention. For our purposes we have taken the recent formulation by Khrashi et al of the shear stress on a circular Voltera dislocation as the basis for the elastic interaction between two concentric dislocations of radius ***r*** and ***r'*** [47, 82]. The resulting energy for an arbitrary, radially-symmetric shear displacement profile is as follows:

$$E_{disl} = E_o[u(r)] - H(\tau) \int_0^\infty dr \int_0^r \frac{du(r)}{dr} \frac{du(r')}{dr'} r\omega(\tfrac{r'}{r}) dr' \tag{3.6}$$

where $H(\tau)$ is the shear stress-dependent shear modulus and ω is the elastic interaction kernel based on $K(\eta)$ and $E(\eta)$, the complete elliptical integrals of the first and second kind respectively.

$$\omega(\eta) = 2(K(\eta) - E(\eta)) \tag{3.7}$$

The goal is to implement the PN energy formulation given by Equations 3.5 through 3.7 in the NEB framework in order to calculate the activation barrier for homogeneous dislocation nucleation. As such we have calculated the derivative of the energy:

$$\begin{aligned}\frac{\delta E_{dis}}{\delta u(r)} &= 2\pi\ r(\gamma[u(r)] - \tau) \\ &\quad - H(\tau)\int_0^r \tfrac{du(r')}{dr'}\tfrac{d}{dr}(r\omega(\tfrac{r'}{r}))dr' \\ &\quad - H(\tau)\int_r^\infty r'\tfrac{du(r')}{dr'}\tfrac{d}{dr}(\omega(\tfrac{r}{r'}))dr'\end{aligned} \tag{3.8}$$

We would like to simplify Equation 3.8. First,

$$\tfrac{d}{dr}(r\omega(\tfrac{r'}{r})) = \omega(\tfrac{r'}{r}) - \tfrac{r'}{r}\omega'(\tfrac{r'}{r})\ , \tag{3.9}$$

and

$$\omega'(\eta) = (\frac{2\eta E(\eta)}{1-\eta^2})\ . \tag{3.10}$$

Application of Equations 3.7, 3.9 and 3.10 to the second term in Equation 3.8 yields:

$$-H(\tau)\int_0^r \tfrac{du(r')}{dr'}(2K(\tfrac{r'}{r}) - \frac{2E(\frac{r'}{r})}{1-(\frac{r'}{r})^2})dr'\ . \tag{3.11}$$

The third term is simply

$$-H(\tau)\int_r^\infty r'\tfrac{du(r')}{dr'}(\frac{2\frac{r}{r'}E(\frac{r}{r'})}{1-(\frac{r}{r'})^2})dr' \tag{3.12}$$

Application of the energy functional in Equation 3.6 within the NEB framework required an additional term because the energy kernel for the elastic interaction due to the displacement gradient was numerically unstable. Convergence along the MEP was possible, but more often than not high frequency numerical oscillations developed in regions where the gradient of the displacement was largest. As a result convergence was very sensitive to the input configurations. A small numerical correction term was added to the interaction kernel

$$\varepsilon\delta(\tfrac{r'}{r}-1) \tag{3.13}$$

where ε is a stabilization factor taken to be 0.01. The total energy then becomes:

$$E_{disl} = E_o[u(r)] + H(\tau)\int_0^{\infty} dr \int_0^{r} \tfrac{du(r)}{dr}\tfrac{du(r')}{dr'} r\omega(\tfrac{r'}{r})dr' + \varepsilon H(\tau)\int_0^{\infty} drr(\tfrac{du(r')}{dr})^2 \tag{3.14}$$

and the variational force is:

$$\begin{aligned} -\frac{\delta E}{\delta u(r)} &= 2\pi\ r(\tau - \gamma[u(r)]) \\ &+ H(\tau)\int_0^{r} \tfrac{du(r')}{dr'}(2K(\tfrac{r'}{r}) - \frac{2E(\frac{r'}{r})}{1-(\frac{r'}{r})^2})dr' \\ &+ H(\tau)\int_r^{\infty} r'\tfrac{du(r')}{dr'}(\frac{2\frac{r}{r'}E(\frac{r}{r'})}{1-(\frac{r}{r'})^2})dr' \\ &+ 2\varepsilon H(\tau)\tfrac{d}{dr}(r\tfrac{du(r)}{dr}). \end{aligned} \tag{3.15}$$

The addition of the small stabilization factor solves the issue of high-frequency numerical noise allowing for easy convergence to the minimum energy path.

Lastly, because our intention is to directly compare the stress-dependence of the activation energy from the formulated PN model with atomistic calculations of the activation energy in chapter two, we have fit the model to data from the EAM potential for Cu by Mishin et al [35]. In Figure 3-2 the GSFE for <112>{111} shear displacement per plane, x_1, calculated with the Mishin Cu potential is given as a function of the affine shear displacement per plane, x_0,

normalized by the partial Burger's vector. The commonly reported GSFE for zero affine strain is found at $x_0/b_p = 0$. As x_0/b_p increases the unstable stacking energy decreases to zero which is a simple illustration of an activation barrier mediated by applied affine shear. With the GSFE surface we can calculate the misfit energy as a function of the <112>{111} displacement in the slip plane as required by the PN model for any applied global strain state.

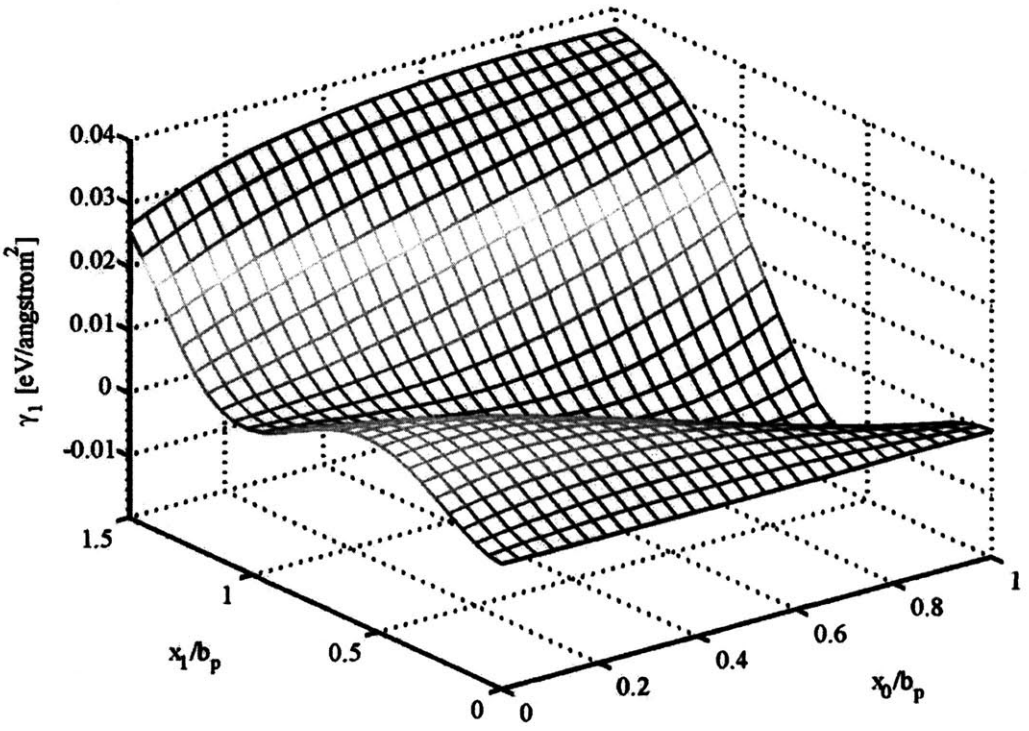

Figure 3-2: The stress-dependent misfit energy, γ, is plotted here in terms of the normalized elastic, x_0/b_p, and plastic, x_1/b_p, displacements between the two atomic planes surround the slip plane. Values are normalized by the partial Burger's vector.

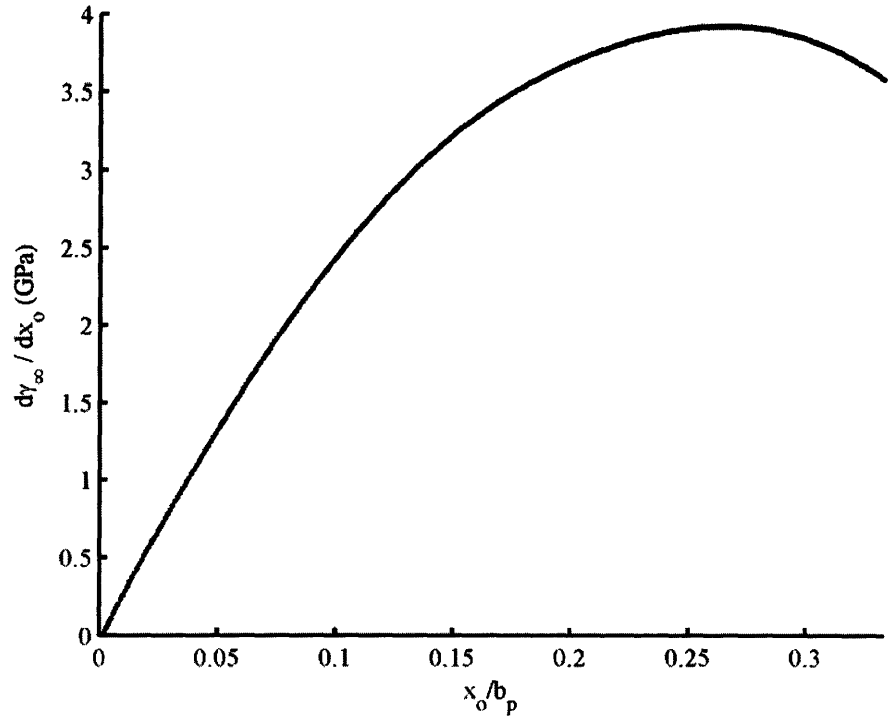

Figure 3-3: The shear stress associated with simple shear for Cu calculated via the atomistic empirical potential by Mishin.

We have also calculated the stress-dependent shear modulus using the Mishin Cu potential. The GSFE in Figure 3-2 is denoted γ_1 indicating that the energy is given for misfit across a single slip plane. In the framework of the multiplane generalized stacking fault energy, a series of such misfit energies for common displacement across an arbitrary number of slip planes (γ_1, γ_2, γ_3, ... etc.) can be defined. Affine shear is the upper limit of the multiplane generalized stacking fault behavior and is denoted γ_∞. In Figure 3-3 we have plotted the shear stress in the system, defined via γ_∞, as a function of the normalized shear displacement. The derivative of this curve w.r.t. the affine shear strain at any value of applied stress is taken as the stress-dependent shear modulus, $H(\tau)$, for our PN model calculations.

3.3 Calculation of Activation Volume via the PN Model

The foundational result for our discussion of the contributions to the stress dependence of homogeneous dislocation nucleation is a calculation of the activation energy and activation

volume given by the fully stress-dependent Peierls-Nabarro model as formulated in the previous section. Having implemented the PN model for a radially symmetric displacement profile in the CINEB framework, we have calculated the activation energy for dislocation nucleation over a range of simple shear corresponding to τ/τ_{ath} = 0.5 through τ/τ_{ath} = 1.0. The free end algorithm has been implemented in these simulations to allow for efficient sampling of the saddle point configuration. An example CINEB pathway relaxed at τ/τ_{ath} = 0.94 is shown in Figure 3-4 where the open circles are the energies calculated from the PN model for configurations along the pathway for dislocation nucleation. The solid line is a spline fit to the energies and forces along the path at each image. The corresponding image configurations are represented in Figure 3-5 by their displacement profile along a single radius. Each image configuration is composed of 256 nodes, i, each representing a circular slice of the slip plane with central radius, r_i, and a thickness, Δr, equal to 0.59 Å. The displacement in the slip plane is constrained to radial symmetry by the energy formulation, and as a result the displacement profile in the slip plane can be fully described by the profile along a representative radius.

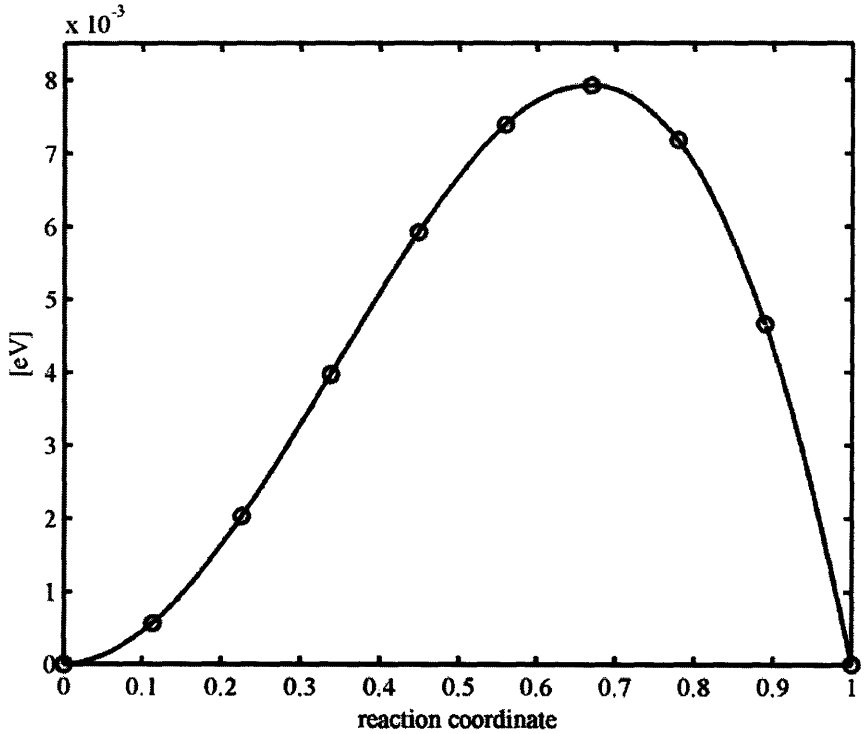

Figure 3-4: An example CINEB reaction pathway for homogeneous dislocation loop nucleation was calculated using the PN model (open circles) at τ = 3.68 GPa.

Following the atomistic study in the previous chapter we have compiled $Q_{PN}(\tau)$ data from the PN model implementation of the CINEB (open circles) in Figure 3-6 and then performed a least-squares fitting of the data to Equation 2.1 (solid line). The fitting parameters for Equation 2.1, Q_o and α_{PN}, taken from the PN calculations are 13.7 and 3.09 respectively.

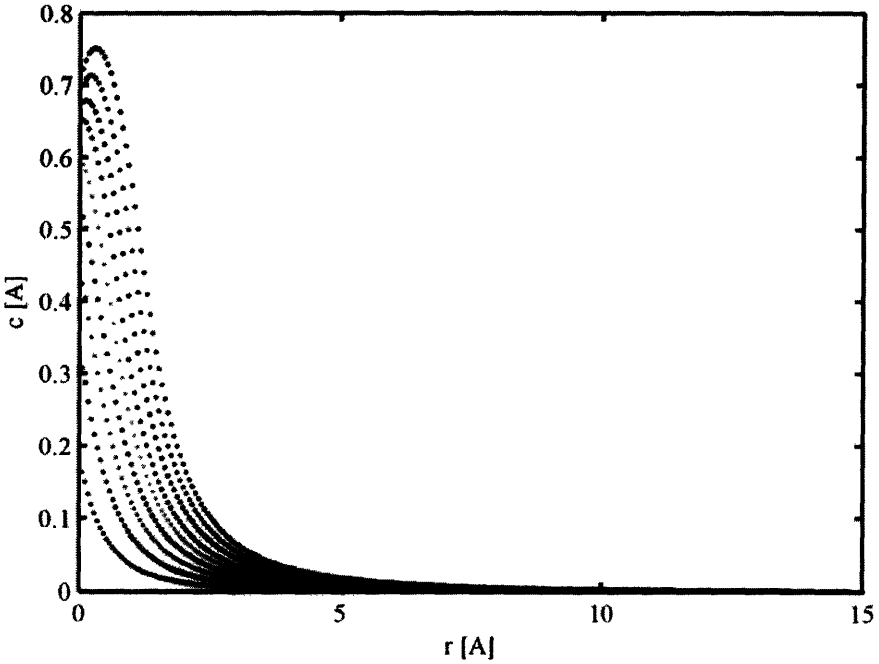

Figure 3-5: The relaxed image configurations for the sample CINEB reaction pathway for homogeneous dislocation loop nucleation at τ = 3.68 GPa are a series of displacement profiles with radial symmetry. The displacement at each of the 256 nodes representing a circular slice of the slip plane with radius, r, are shown for the nine image configurations along the reaction pathway.

The shear stress-dependent behavior of the PN model is quantitatively and qualitatively different than the atomistically derived data, plotted in Figure 3-6 as a dashed line. Although in the fit region Q_o is equivalent for the two calculations, the rate at which the activation energy dies off with applied shear stress as defined by the exponent of the driving stress is much higher for the PN model. The exponent, α_{PN}, is 3.1 where in the fully atomistic simulations we have calculated α = 1.8. As a result the activation energy calculated with the PN model in Figure 3-6 is much lower at any given stress than the atomistic data. We will discuss the possible causes of the discrepancy in activation energies between the atomistic and PN calculations at the end of this section.

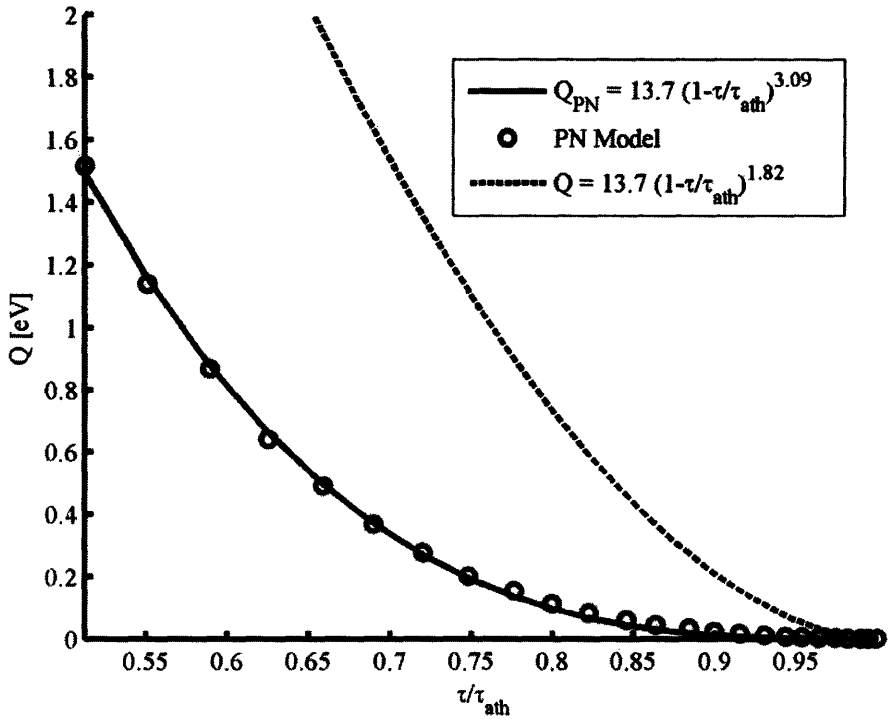

Figure 3-6: The activation energy calculated via CINEB using the PN model (open circles) decreases at a much higher rate with applied shear stress than the least-squares fit behavior taken from atomistic CINEB with the Mishin Cu potential (dashed line).

The image configurations calculated by the PN model are radially symmetric in-plane shear displacements or circular dislocation loops. A displacement profile, ***u(r)***, such as those shown in Figure 3-5 fully describes the shear defects because the energetic formulation for this model assumes radial symmetry. The numerical integral for the structural activation volume defined in Equation 2.4 for this model, Ω'_{PN}, is then taken as:

$$\Omega'_{PN} = \sum_i [\pi(r_i + 0.5\Delta r)^2 - \pi(r_i - 0.5\Delta r)^2]u_i + \pi(0.5\Delta r)^2 u_1 \tag{3.16}$$

which simplifies to

$$\Omega'_{PN} = 2\pi\Delta r \sum_i r_i u_i + 0.25\pi\Delta r^2 u_1 \tag{3.17}$$

and is simply a sum over the volume of cylindrical shells of thickness Δr, central radius r_i and height equivalent to the shear displacement, u_i for each node. The second term is a correction for

the center of the shear defect from $r = 0.0–0.5\Delta r$, which is required because the first node in our formulation sits at $r = 0$.

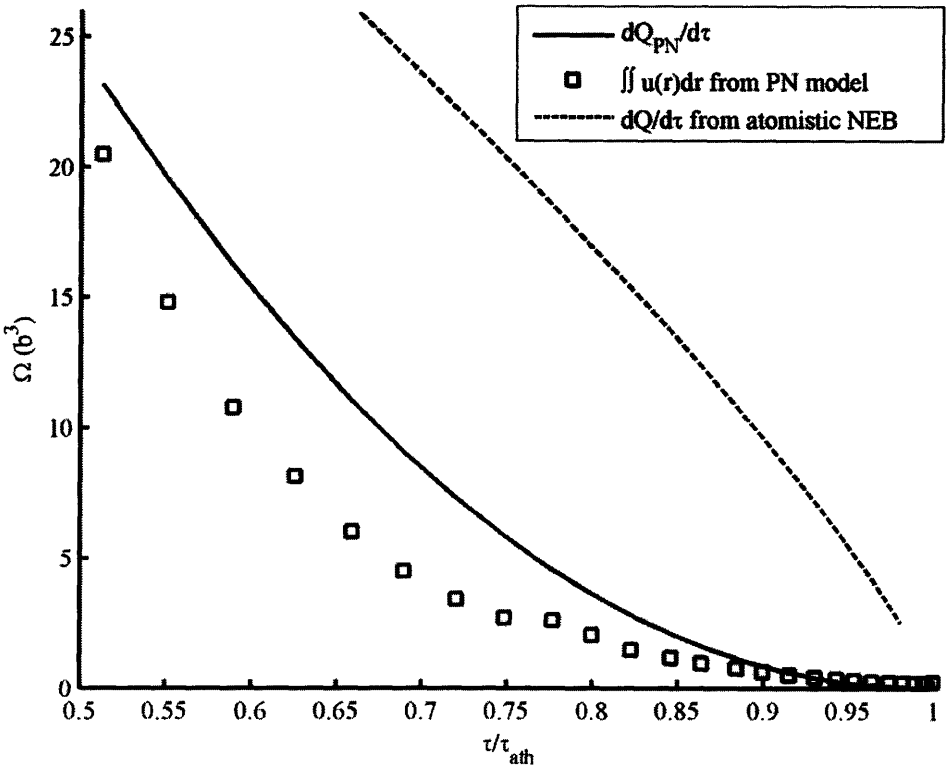

Figure 3-7: The activation volumes calculated from the least square fitting of the atomistic CINEB (dashed line) and PN model CINEB (solid line) activation energies reflect the difference in stress dependence. The structurally defined activation energy calculated from the PN model (open squares) is also plotted.

Using the structural definition in Equation 3.17 and the derivative of Q_{PN} w.r.t. τ, we have calculated the activation volume from the PN model. The activation volume according to both the structural (open squares) and analytic (solid lines) definitions is plotted in Figure 3-7. The structural definition from the PN model exhibits a change in behavior near $\tau/\tau_{ath} = 0.77$ associated with the cross-over between shear perturbations with a local shear displacement greater than $|0.5\boldsymbol{b}_p|$. Below this stress greater spreading in the plane occurs which causes a change in the rate at which the structurally-defined activation volume decreases in the plane. The same behavior is not observed in the derivative of Q_{PN} which decreases continuously to zero at τ_{ath}. The relationship between the structural and analytic definitions for activation volume from the PN model is similar to the trends observed for the atomistic simulations. In both cases the

effect of the spreading of the saddle point configurations in the slip plane at high shear stresses, which is observed in the structurally defined activation volume, is counterbalanced in the analytic description. As a result, for both the atomistic and PN model the analytically defined activation volume is continuous despite the change in behavior of the saddle point near τ/τ_{ath} = 0.77.

The formulation of the PN model as an in-plane shear displacement coupled to a sheared elastic continuum constrains the model to failure within the slip plane. In general we would expect that failure modes in the slip plane would dominate for a material such as Cu with highly localized atomic interaction and as a result the constraint should not negatively affect the model's behavior. However, the dramatic difference between the stress-dependence of the activation energy for homogeneous dislocation loop nucleation with the continuum PN model and atomistic simulations challenges the assumed failure mode.

In order to determine how the perfect crystal fails under affine shear when allowed access to full atomic degrees of freedom, we have turned to an analysis of the phonon modes under increasing applied shear. In general the softening of individual phonon modes correspond to specific instabilities within a lattice [83]. The energetic penalty for affine shear, γ_{∞}, would predict failure near 3.91 GPa for the Cu Mishin potential whereas for shear in a single slip plane we would expect a critical stress of 3.6 GPa [12]. The athermal stress for the atomistic simulations was shown in Figure 2-5 to be around 3.78 GPa according to MD simulations and NEB calculations. In the framework of the multiplane generalized stacking fault energy the athermal stress seems to indicate a first soft mode represented by neither γ_1, as originally expected, nor γ_{∞} but rather some intermediary (γ_2 , γ_3, etc.). Some precedent for an intermediate mode going soft first is seen in Al [84]. However, the longer-range directional nature of bonding in Al relative to CU [40, 41] is thought to be responsible for this behavior.

Phonon analysis for Cu with the Mishin potential indicates that the lattice first becomes unstable at 3.74 GPa and that the unstable mode corresponds to the shuffling of alternating slip planes throughout the entire lattice. The stress at which the phonon analysis predicts crystal instability is in line with our atomistic calculation of the athermal stress at 3.78 GPa because the

constraint of a finite atomistic simulation should increase slightly the critical stress in comparison to the unconstrained phonon analysis. The atomistic simulation limits the phonons to frequencies commensurate with the periodic boundary condition and the size of the supercell. The failure mode indicated by this analysis is excluded from the formulation of the PN model. As a result the stress-dependent behavior for the atomistic simulation and PN model is necessarily different, near the athermal stress in particular, because the failure modes which first result in lattice instability in one are not accessible to the other.

Although the difference in failure mode undoubtedly plays a role in the different stress dependence of the PN model and atomistic calculations, the lower activation energy at all stresses given by our PN model likely indicates a more severe flaw in its formulation. The energy associated with the initial perfect crystal is equivalent for both the atomistic and PN model calculations. From a purely structural perspective, the limited degrees of freedom in our PN formulation should not result in a decrease of the configurational energy at the saddle point. A well-formed energetic description with limited degrees of freedom should give higher energies that an equally well-formed description with more degrees of freedom. Some insight has been gained from the pursuit of this PN formulation but it seems likely that the elastic interaction kernel is too simple to be considered an accurate reflection of the energy for a circular shear displacement profile.

3.4 Break-down of Stress-Dependent Behavior

Although the stress dependence of the activation energy for homogeneous dislocation nucleation is not in general well-modeled by our Peierls-Nabarro formulation, we expect that some additional insight is possible by proceeding to study the contributions to the stress dependence. The formulation of the PN model contains a stress-dependent shear modulus, $\boldsymbol{H}$, taken as the derivative of the curve presented in Figure 3-3. Under zero applied shear stress, we have calculated the shear modulus, $\boldsymbol{H_o}$, to be 41.1 GPa. We have performed a series of CINEB simulations using the PN model with $\boldsymbol{H}$ constrained to $\boldsymbol{H_o}$ for all values of applied shear stress. The resulting activation energy, $\boldsymbol{Q_{Ho}}$, is plotted in Figure 3-8 as open circles and a least-square fit

of the data to Equation 2.1 was performed (solid line). For comparison we have also included the observed behavior of the atomistically derived activation energy (dashed line) and the fully stress-dependent PN model (dotted line).

The Q_{Ho} data in Figure 3-8 does not fit the standard form given in Equation 2.1. The R^2 value is an order of magnitude higher than the fit to Q_{PN} data. However, by removing the stress-dependence of the shear modulus, we do see a significant increase in the activation energy for stresses near the athermal stress. The continuum study of activation energy for dislocation nucleation by Xu and Argon [44] did not consider a stress dependent modulus, and as previously discussed, the calculated activation energy was a factor of four higher than the atomistic data. In general the stress-dependent modulus should lower the activation energy at any given applied stress and should be considered as a possible path towards upgrading the model of Xu and Argon.

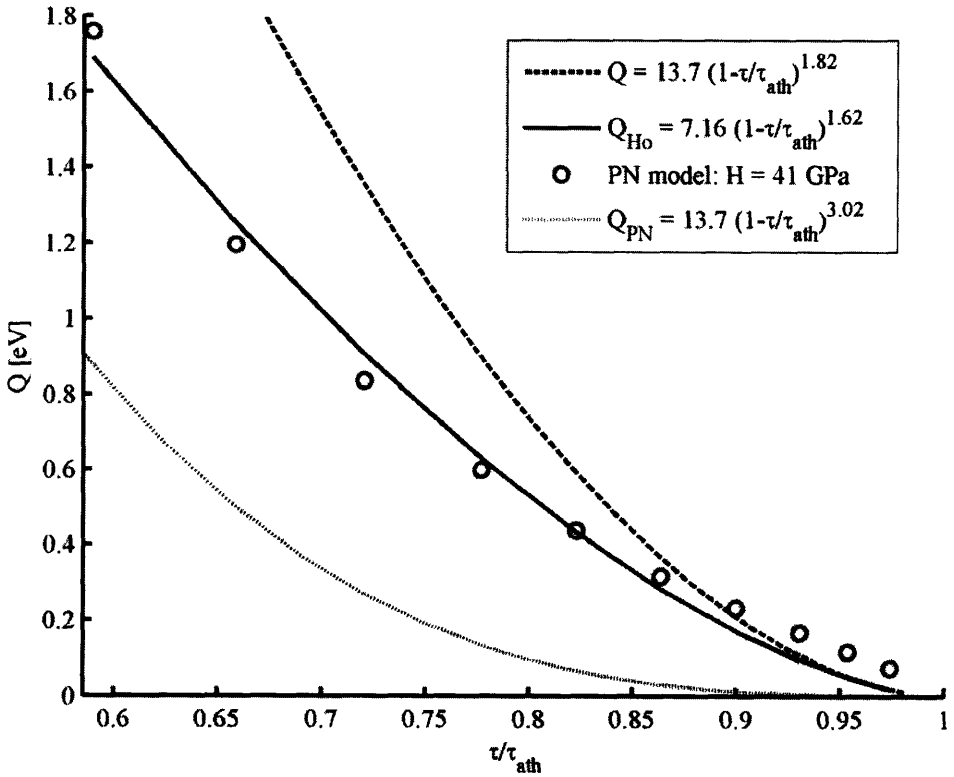

Figure 3-8: The activation energy, Q_{Ho}, calculated via the CINEB method using the PN model holding constant the shear modulus (open circles) falls between Q_{PN} (dotted line) and the activation energy from the atomistic CINEB calculations, Q (dashed line). The CINEB data does not fit well (solid line) to the form used for the atomistic data.

In Figure 3-9 the activation volume calculated structurally via Equation 2.1 and as the derivative of the least-square fit to Q_{Ho} w.r.t. τ is plotted versus the normalized shear stress. We have also included the analytic activation volumes for the atomistic data and the fully stress-dependent PN model.

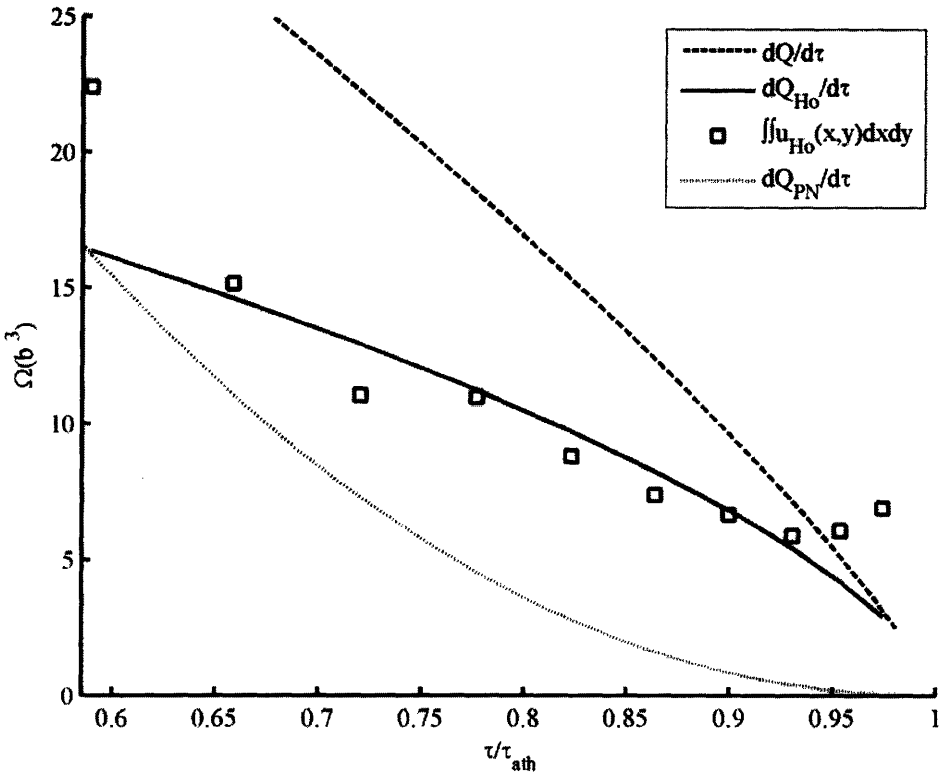

Figure 3-9: The activation volume calculated from the least-squares fitting of the atomistic NEB (dashed line) and the constant shear modulus PN model (solid line) exhibit the same general trend with significantly lower volume from the PN model. The structural defined activation volume (open squares) from the constant shear modulus PN model increases as τ approaches τ_{ath}.

The structurally defined activation volume exhibits a more dramatic stress-dependent behavior than observed in either the atomistic data or fully stress-dependent PN model. In Figure 3-9 the activation volume increases as the shear stress increases near the athermal stress. Furthermore, in the fully stress-dependent model the energy penalty due to the defect is lessened by the decreasing shear modulus. The activation energy in Figure 3-8 exhibits a slowed rate of decrease above $\tau/\tau_{ath} = 0.8$. The effects of the increasing structurally defined activation volume

in this regime are observable in the activation energy because $H(\tau) = H_o$ and does not lessen the penalty for activation volume as τ approaches τ_{ath}.

3.5 Conclusions

Near the athermal stress the failure mode for Cu corresponds to neither shear in a single slip plane nor to the affine shear. Instead we have observed an intermediate mode of shuffling slip planes to be responsible for instability. The choice of a mode inaccessible to the PN model plays a role in the mode's inability to accurately capture the full stress-dependent behavior observed atomistically.

Holding constant the shear modulus increases the activation energy at any level of applied shear stress. We expect that inclusion of the stress-dependent shear modulus may allow for improved accuracy, within the limitations of the model, for some previously formulated PN models for dislocation nucleation.

Although the PN model itself is seemingly flawed, its implementation has provided a useful framework for analysis of the stress-dependent behavior of the activation energy and saddle-point configurations for homogeneous dislocation loop nucleation. For shear stresses greater than $\tau/\tau_{ath} = 0.75$ the structurally defined activation volume is relatively constant or in some instances of the PN model increasing. The behavior is, in all cases, incompatible with the actual stress dependence of the activation energy in this regime which decreases continuously to zero. A closer look at the structure of the saddle point configuration reveals that the maximum displacement for both the atomistic and PN model configurations decreases continuously to zero. The nearly constant structural volume is a result of high energy activation volume at the peak being replaced by low energy volume near the periphery of the defect as it expands in the plane. In the original conception of the term, all activation volume was equal because the displacement of the defect was considered constant and the volume depended only on the area swept out by the dislocation. When the saddle point configuration becomes an in-plane shear perturbation not all activation volume contributes equally to the activation energy. The previous statement is different than observing that each activated particle contributes a different level of shear

displacement thus allowing the activation volume to be low while including a large number of particles. The relationship between a displacement profile and a misfit energy function such as the one described in Figure 3-2 indicates that at a constant applied shear stress each unit of activated volume does not make the same contribution to the activation energy. Furthermore the decreasing misfit energy and shear modulus with increased applied stress ensure that although the total activated volume according to the structural definition may increase, in general the energetic penalty for this activated volume decreases as the applied stress rises.

Chapter 4

Three-Dimensional Shear Localization in Incipient Plasticity

4.1 Introduction

One of the first theoretical indications of the need for a localized mechanism for shear deformation in materials came from the study published in 1926 by Frenkel in which he estimated the resolved shear stress required for plastic deformation by shearing two rigid blocks relative to one another [48]. The theoretical calculation showed that the stress required for rigid shear was orders of magnitude higher than the experimentally observed onset of plastic deformation. The simple observation of the disparity between model and experiment quickly led to the hypothesis and subsequent discovery of dislocations. In the intervening decades our understanding of the mechanisms for the onset and accumulation of plastic deformation has dramatically increased to include detailed atomistic description of a vast array of defect processes. However, simple models still have much to say regarding these unit processes for deformation particularly in terms of calculating controlling parameters for constitutive behavior and providing physical intuition to otherwise massively complex problems [79, 85].

The unit processes of shear deformation occur primarily at the atomistic length scale and, as in the case of dislocation nucleation and propagation, are often the result of motion localized to a single slip plane. However, the driving force for shear deformation is the global stress often applied at a dramatically larger length scale and simultaneously acting on the entire system. Our particular interest in this chapter is to discuss the process by which globally applied shear strain localizes to form an atomistic defect capable of relieving the applied strain. The one-dimensional chain model described first by Chang et al will be utilized as a means of discussing incipient

plasticity in a fully three-dimensional system [86]. The foundational work for this discussion is a description of shear localization in BCC molybdenum via "wave-steepening" performed by Chang with the one-dimensional chain model. We plan to expand the wave-steepening analysis to a fully three-dimensional atomistic description of shear localization in Cu.

4.2 Wave Steepening Behavior

The most important parameter for the description of the onset of partial dislocation loop nucleation is the relative displacement, in the <112> {111} direction, of a series of adjacent slip planes. By restricting all of the atoms in these planes such that they move as a single unit and limiting their motion to the <112>{111} partial Burger's vector direction, the degrees of freedom required to model partial dislocation nucleation can be reduced from $3N$, where N is the number of particles in the system to n, the number of planes in the system. With these constraints any atom contained within a single slip plane can be used to describe the behavior of that plane, and the entire system can be described by the behavior of a one-dimensional chain of atoms with a representative from each plane. The deformation of the entire system can therefore be described by a series of displacements in the <112>{111} direction between adjacent planes given by $\Delta x = (\Delta x_1, \Delta x_2, \ldots, \Delta x_i, \ldots, \Delta x_n)$. The significant decrease in degrees of freedom creates a tractable parameter space that allows for relatively straightforward analysis and visualization of shear deformation. Physically accurate deformation mechanisms cannot be observed because local atomic relaxations are not allowed, but the elegance of the model allows for a strong intuitive understanding of the energetic barriers related to shear deformation and the initial behavior of a mechanically unstable crystal lattice.

Constrained molecular dynamics simulation can be performed with this one-dimensional system. In the original work by Chang in BCC Mo a simple shear perturbation was applied normal to the slip plane [86]. In addition an initial affine shear strain very near the athermal strain of the one-dimensional chain system was then applied. MD integration was then performed and the evolution of the shear perturbation over time observed. The four stages of wave steepening observed by Chang in an initially sinusoidal shear displacement "wave" were linear

growth, non-linear growth, shear shock formation, and finally atomistic defect formation. In the one-dimensional MD simulation these four stages were well defined as the initial sinusoidal wave exhibited first increasing amplitude and then became asymmetric while further increasing in amplitude (wave steepening). Next the shear displacement profile became discontinuous (wave breaking), and finally formed a two-layer twin nucleate which is the first stable atomistic defect in a BCC Mo lattice.

4.3 Shear Localization in Perfect Crystals

In order to observe the process of shear localization in a fully three-dimensional system, a CINEB relaxation of the pathway for homogeneous dislocation nucleation was performed using the embedded atom method (EAM) potential for Cu developed by Mishin et al as the basis for calculation of both the total energy and atomistic forces [34]. The calculation of the pathway is considered converged when the sum of the atomic forces perpendicular to the path is less than 0.005 eV/Å^2 in each image.

The reaction pathway for homogeneous dislocation loop nucleation within a 161280 particle simulation cell under a constant <110>{111} simple shear strain of 0.096 (with all other elements of the strain tensor equal to zero) is shown in Figure 4-1. The strain state was chosen such that the activation energy is 1 eV and the saddle point configuration is a small partial dislocation loop. The complete set of 58 input configurations included the nucleation of a leading and then trailing partial dislocation loop so that both the initial and final configurations were perfect crystals differing only in the strain relieved by propagation of a single full dislocation through the simulation cell. With the goal of carefully observing the onset of dislocation loop nucleation, the input configurations were biased such that the density of images prior to the saddle point was approximately ten times higher than the image density along the remainder of the path. The initial disparity in density was maintained throughout the simulation because the highest energy image is allowed to search for the saddle point configuration during CINEB calculations. The decoupling of the saddle point configuration, from the standard NEB path integration, does not allow for transmission of a difference in spring force across the saddle and the relationship between the image spacing before and after the saddle point configuration in the

final relaxed pathway is therefore unconstrained. In this way the image density along the path can be biased toward higher density either before or after the saddle point depending on the region of greater interest.

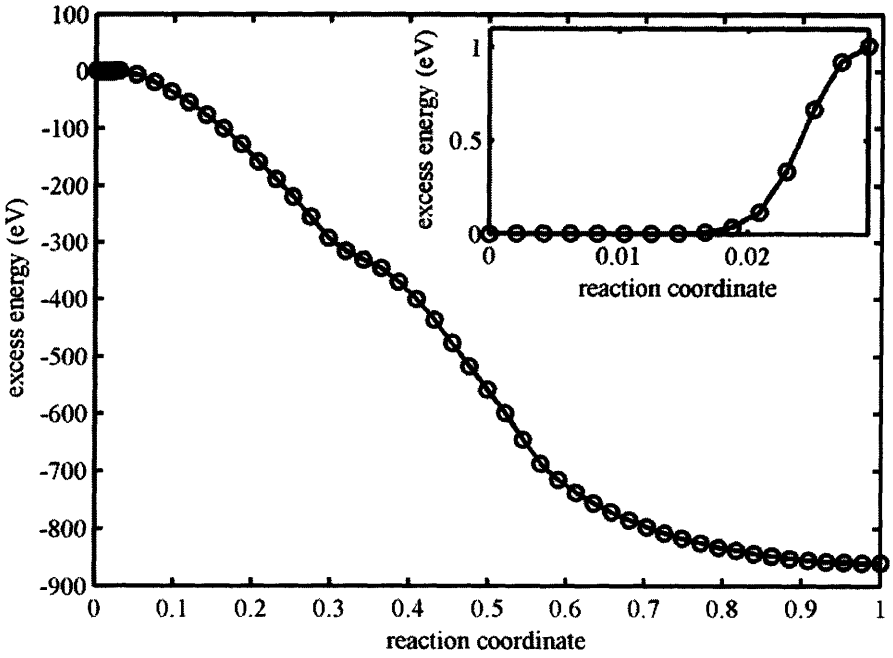

Figure 4-1: Full energetic pathway for homogeneous nucleation of a leading and trailing partial dislocation loop under <110>{111} simple shear strain of 0.96. The inset shows the biased image density maintained prior to the climbing image along the pathway.

As the system evolves along the path in Figure 4-1, the initially perfect crystal becomes mechanically unstable. Before submitting to the one-dimensional chain analysis, we will consider the behavior of the entire system as it moves along the path. Taking the perfect crystal lattice as a reference state, the displacement of each particle in the simulation is plotted in Figure 4-2 for each of the first six image configuration. The perfect crystal develops a sinusoidal displacement wave in the <110> and <112> directions. Proceeding along the path, shear displacement perturbation maintains the sinusoidal behavior but increases in magnitude for each of the initial seven image configurations. The behavior is reminiscent of the first stage of the "wave-steepening" description of shear localization in the one-dimensional chain analysis. The input configurations for this CINEB relaxation were created by linear extrapolation between the initial configuration, a perfect fcc crystal, and a small dislocation loop. The initial portion of the

relaxed reaction pathway which includes a regime where all the atoms in each {111} slip plane move in concert was never included as part of the input.

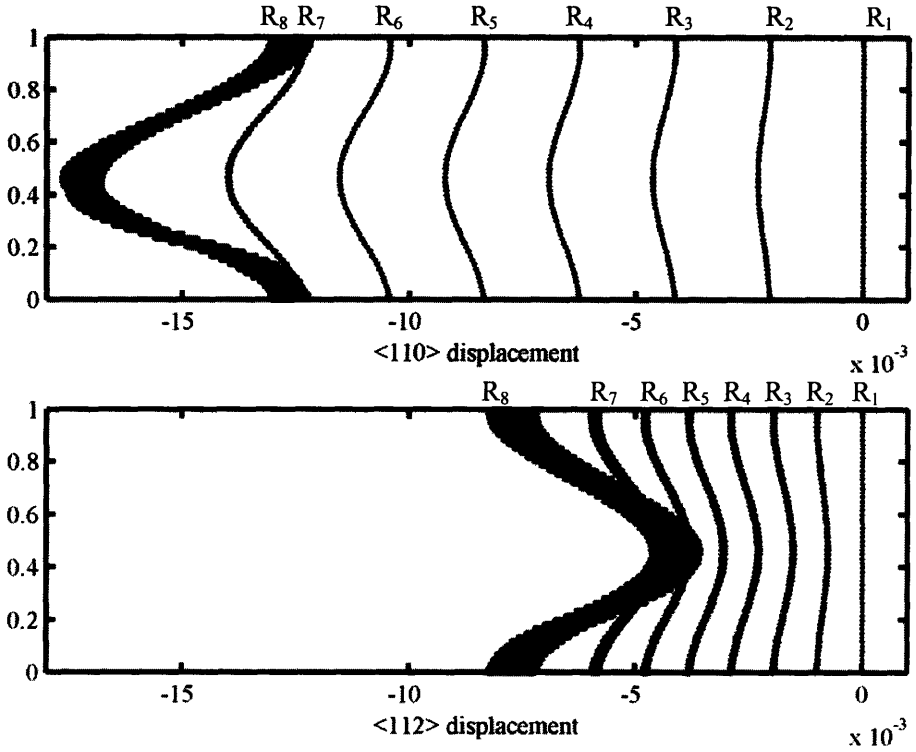

Figure 4-2: The shear displacement in the <110> and the <112> directions between each particle in the initial configuration and the corresponding particle in the first eight images along the reaction pathway are plotted here versus the normalized particle position in the <111> direction normal to the slip plane. The displacement profiles, given in units of angstroms, show linear growth of a shear wave until R_8, where spreading is observed in the particle displacements in each plane.

Uniform linear growth of a sinusoidal displacement is exhibited by the entire three-dimensional system in Figure 4-2 until R_8. As the system moves further along the reaction pathway, the range of displacement in each plane broadens which indicates that the particles in each slip plane are no longer moving as a rigid unit. Figure 4-3 shows the progression of the displacement profiles for the full system via representative image configurations along the reaction pathway. The broadening of the initially uniform sinusoidal displacement wave is shown in Figure 4-3a. Here the data is plotted such that the spacing between {111} planes, along the <111> normal to the slip plane, is discernable. As a consequence we can visualize the three-

dimensional system in terms of the displacement of particles localized to discrete atomic planes. The magnitude of the maximum in-plane shear displacement approaches $|\boldsymbol{b}_p|$ at R_{17} in Figure 4-3b. A partial dislocation loop is forming but has not swept across the entire configuration which results in the range of displacements at the slip plane. Furthermore, significant displacement is observed for seven or eight planes above and below the slip plane in this unstable configuration. Figure 4-3c shows the displacement profile for the stacking fault in R_{28}. All particles adjacent to the slip plane exhibit non-zero shear displacement and the range of shear displacements in the slip plane has narrowed to values near $|\boldsymbol{b}_p|$. In addition more planes above and below the slip plane are now contributing to the defect. However, the stacking fault is unstable under the applied strain, and the configuration continues to evolve as a trailing partial dislocation is nucleated in Figure 4-3d which is associated with R_{34}. The nucleation of a trailing partial dislocation is marked by broadening of the displacement profile in both the <110> and <112> directions. However, a full dislocation constitutes displacement in the <110> direction only. As a result increased atomic displacement in the <110> direction approaching $|\boldsymbol{b}|$ corresponds to atomic displacement in the <112> direction returning to zero. Finally as the full dislocation annihilates through the periodic boundary within the slip plane the system is once again a perfect crystal in the final image configuration, R_{58}. The decrease in the magnitude of the affine shear displacement by a full Burger's vector is observed in the atomic displacements in Figure 4-3e.

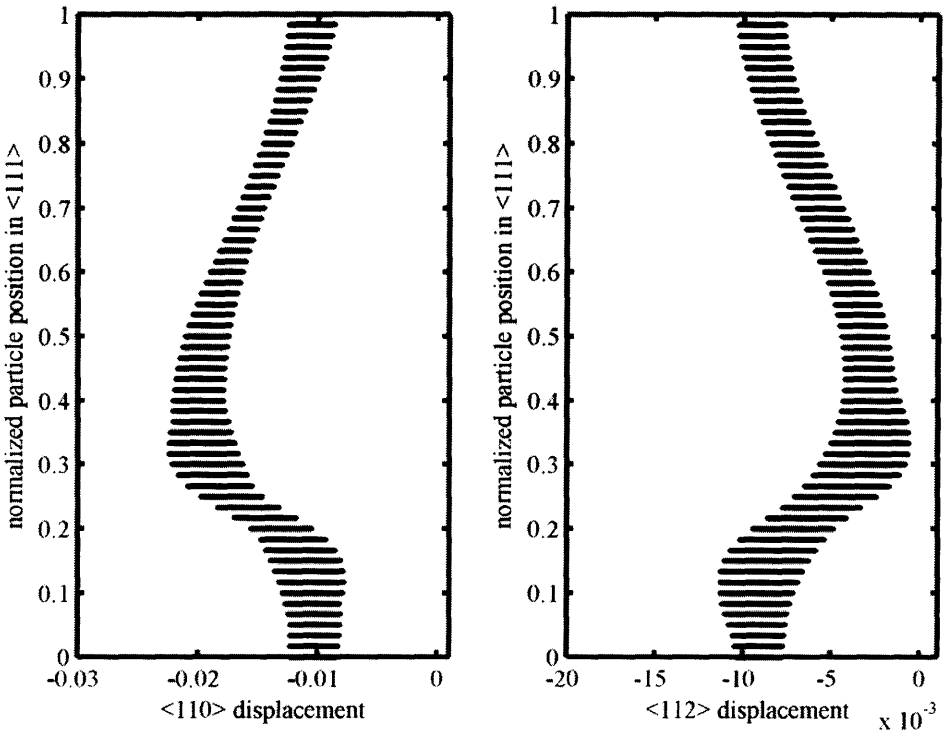
normalized particle position in <111>
<110> displacement
<112> displacement
x 10^-3

a)

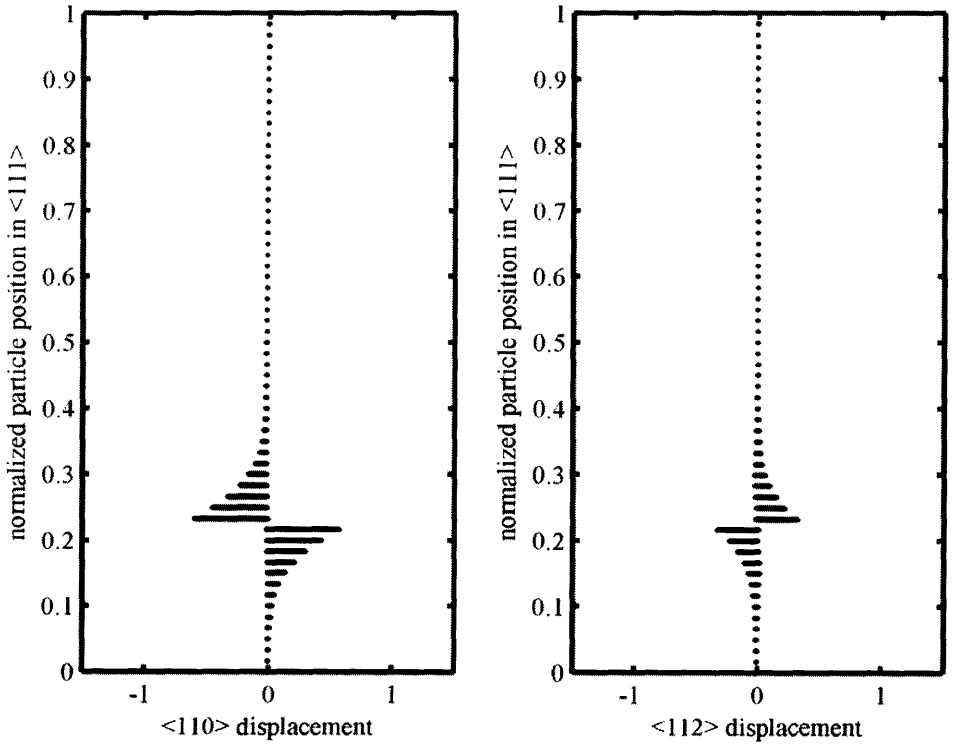
normalized particle position in <111>
<110> displacement
<112> displacement

b)

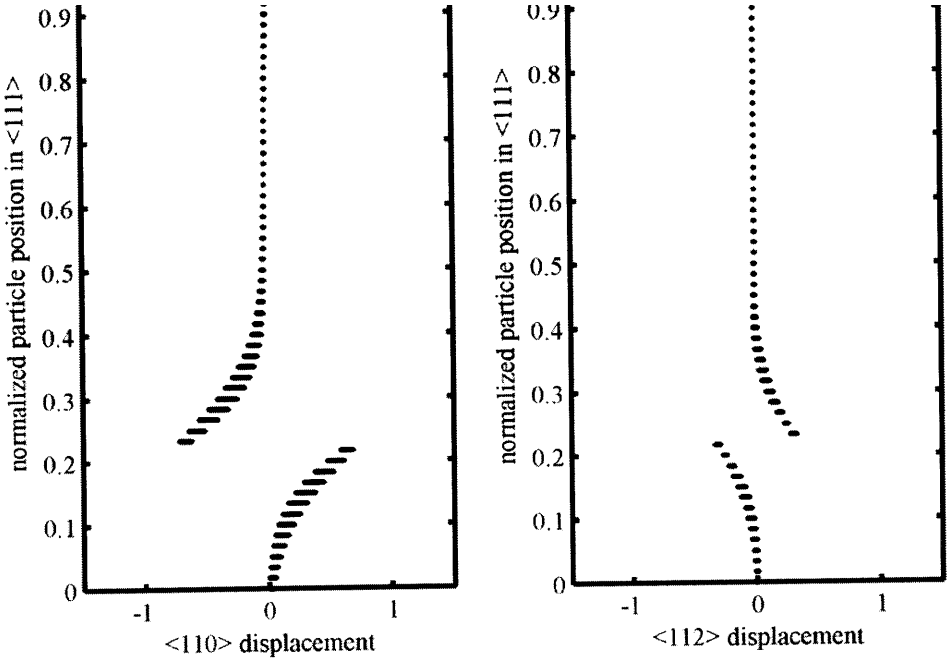
normalized particle position in <111>
0.9
0.8
0.7
0.6
0.5
0.4
0.3
0.2
0.1
0
-1
0
1
<110> displacement
normalized particle position in <111>
0.9
0.8
0.7
0.6
0.5
0.4
0.3
0.2
0.1
0
-1
0
1
<112> displacement

c)

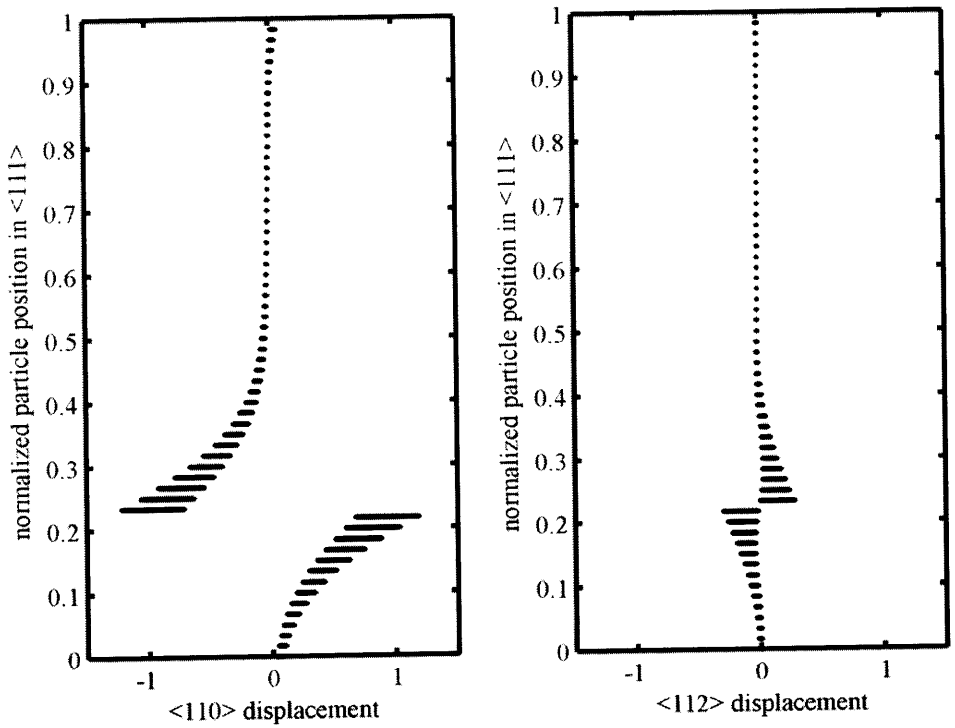
normalized particle position in <111>
1
0.9
0.8
0.7
0.6
0.5
0.4
0.3
0.2
0.1
0
-1
0
1
<110> displacement
normalized particle position in <111>
1
0.9
0.8
0.7
0.6
0.5
0.4
0.3
0.2
0.1
0
-1
0
1
<112> displacement

d)

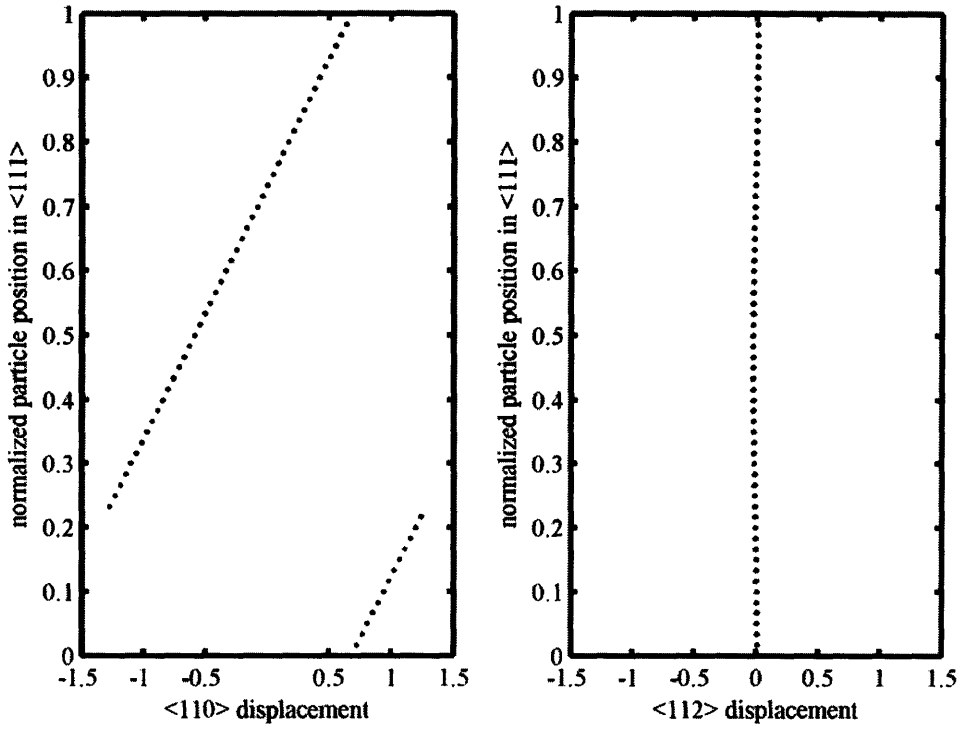

e)

Figure 4-3: The displacement in the <110> and <112> directions from the initial perfect crystal configuration to a series of images along the reaction pathway is plotted for each of 161,280 particles in the atomistic CINEB calculation. The pathway corresponds to a) the onset of shear localization, b) the nucleation of a leading partial dislocation loop, c) the formation of an unstable stacking fault, d) the nucleation of a trailing partial dislocation loop and e) the return of a prefect crystal whose strain is decreased by the Burger's vector compared to the initial perfect crystal configuration.

4.4 Three-Dimensional 1-D Chain Analysis

Our intention is to follow the process of shear localization for a three-dimensional system with full atomistic degrees of freedom with an eye towards the wave-steepening behavior described in the previous sections. The CINEB simulations remove the constraint of the one-dimensional chain model which requires all atoms in a slip plane to move as a single unit. However, the concept of a one-dimensional chain can still be applied to the three-dimensional system by defining one-dimensional chains with a single atom from each of the 60 {111} slip planes in the simulation cell. The system was divided such that each of the 2688 one-dimensional chains contains atoms from each slip plane as close as possible to the same <111> direction normal to the slip plane. The stacking of the {111} planes in the FCC structure results in a spiral arrangement of particles in each chain. An example of one of these one-dimensional chains is given in Figure 4-4 where all other particles in the configuration have been removed for clarity. Each image configuration is now considered as a two-dimensional grid of one-dimensional chains, and the behavior of each chain along the reaction pathway can be examined in order to characterize the behavior of the three-dimensional atomistic system during homogeneous dislocation loop nucleation.

As shown in Figure 4-2, the system no longer conforms to the one-dimensional chain model as early as image seven, and we must switch to the three-dimensional analysis for a more detailed picture of the systems behavior. In Figure 4-3a the displacement profiles of the 2688 chains in our system have diverged, but following each quickly becomes cumbersome. As a result we have chosen to track the behavior of two chains in particular, the first passing directly through the center of the developing partial dislocation, chain A, and the second as far removed, considering the in-plane periodic boundary condition, from this center as possible, chain B. The positions of each chain relative to the emerging dislocation loop are indicated by a white circle and a green square respectively in Figure 4-5.

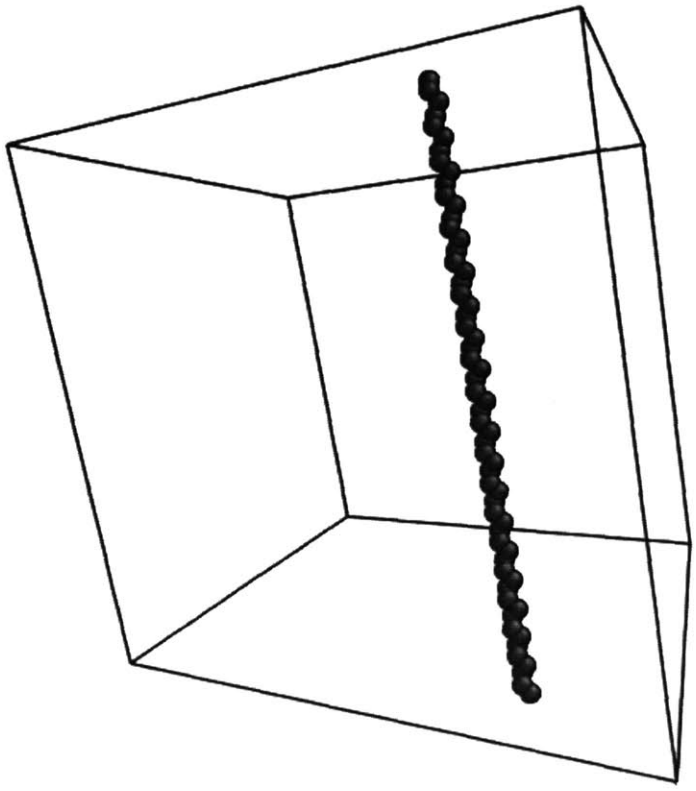

Figure 4-4: A sample one-dimensional chain in the three-dimensional configuration shows the spiral pattern along the chain direction which is a consequence of the atomic stacking of {111} slip planes in an FCC lattice

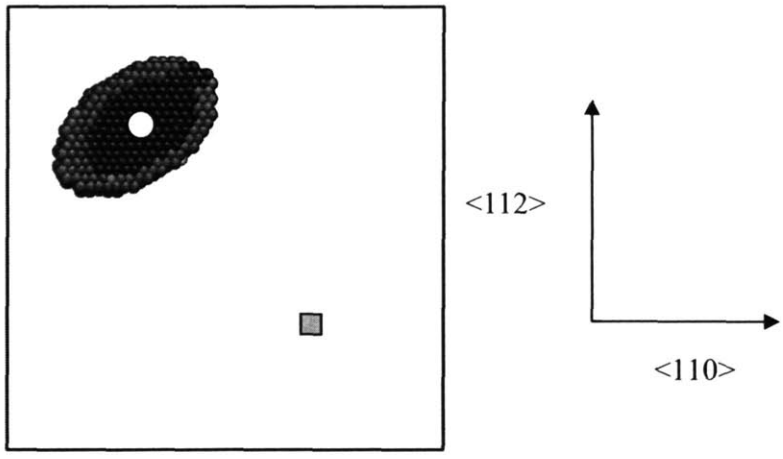

Figure 4-5: The positions relative to the emerging defect for the two one-dimensional chains used in the current analysis are shown as a white circle, chain A, and a green square, chain B. Chain A passes through the center of the emerging defect while chain B is as far from the center as possible considering the periodic boundary condition.

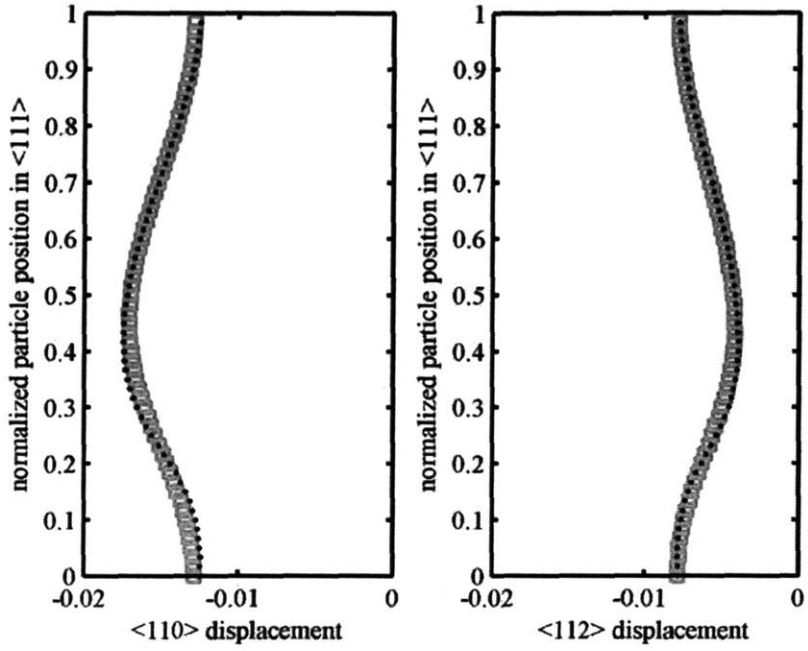
normalized particle position in <111>
<110> displacement
<112> displacement

a)

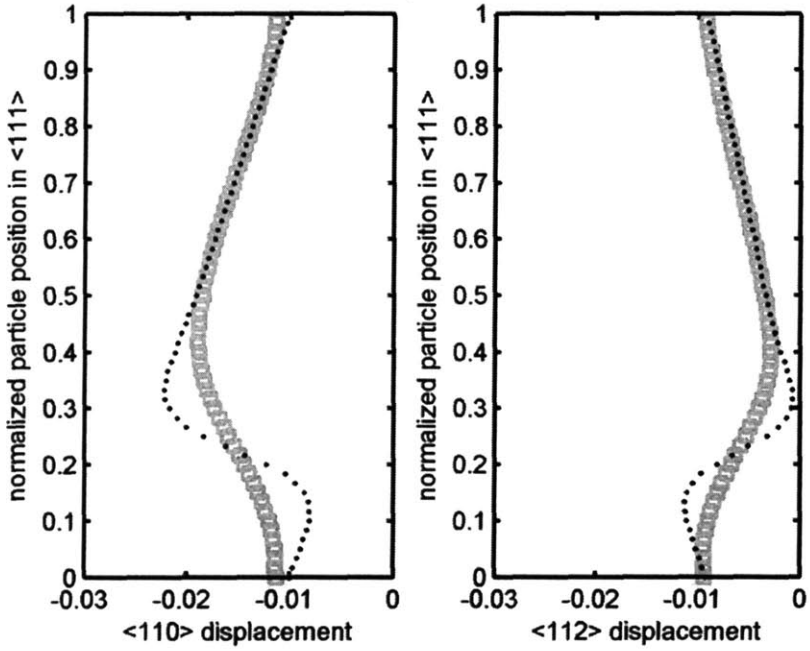
normalized particle position in <111>
<110> displacement
<112> displacement

b)

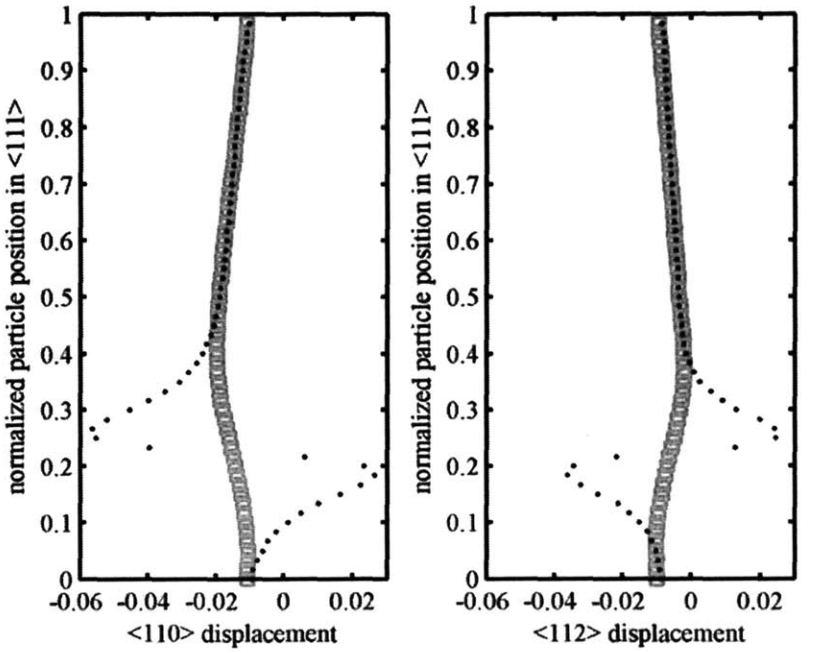

c)

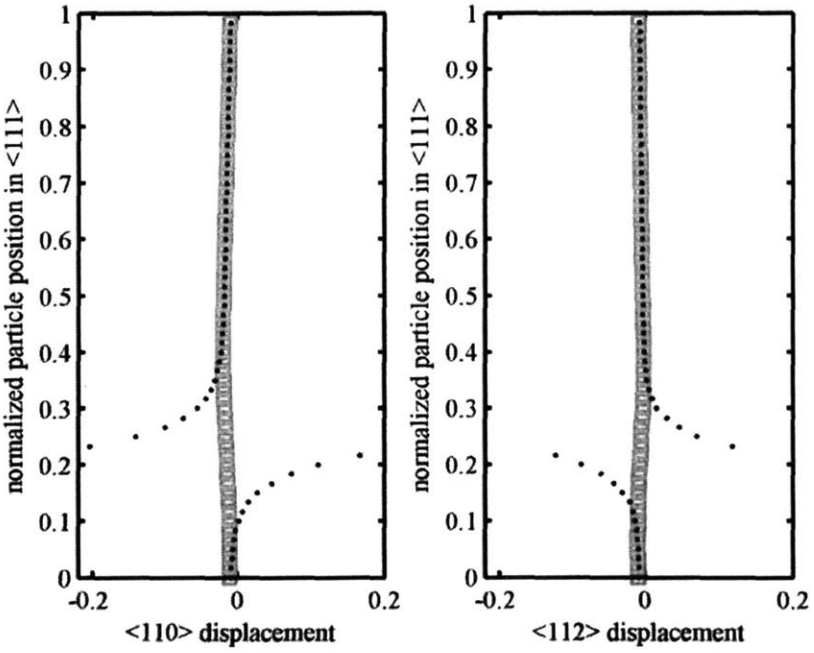

d)

Figure 4-6: For each particle in chain A (points) and chain B (open squares) the displacement between the initial strained perfect crystal configuration and a series of images along the reaction pathway for dislocation nucleation exhibit the four stages of wave steepening. Shear localization in chain A occurs with a) initial divergence from the uniform linear growth of the entire system (R_7) and proceeds through b) non-linear growth (R_8), c) formation of a shear shock (R_{10}) and ultimately d) atomistic defect nucleation (R_{12}). Displacements are given in units of angstroms.

Both chains, and in fact the entire system, initially exhibit a linearly-increasing sinusoidal perturbation (Figure 4-2). A series of displacement profiles for chains A and B, as dots and open square respectively, are shown in Figure 4-6 as the system evolves along the section of the reaction pathway in Figure 4-1 prior to the saddle. Divergence in the behavior of these two chains, as the displacement profile for chain A becomes non-linear and the magnitude of the maximum displacement in chain A surpasses that of chain B is shown in Figure 4-6a and constitutes the first instance of three-dimensional shear localization in our system. The linear growth of chain B is slowed as the evolution of the system is localized towards the volume surrounding chain A. This localization is observed as non-linear growth in chain A in Figure 4-6b. Chain A then proceeds to a discontinuous displacement profile in Figure 4-6c, and finally to the formation of an atomistic defect (in this case a partial dislocation loop) in Figure 4-6d. Chain B proceeds much more slowly through this same series of behaviors and exhibits essentially linear behavior leading into non-linear growth until after the partial dislocation loop is fully formed in Chain A. As the dislocation loop sweeps through the slip plane, beyond the saddle in the reaction pathway, chain B exhibits the final three stages of wave steepening behavior (not shown).

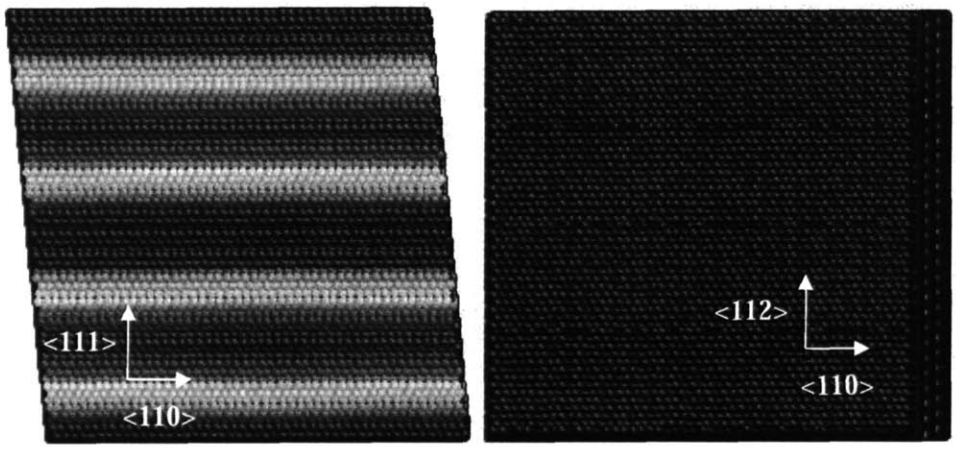

a)

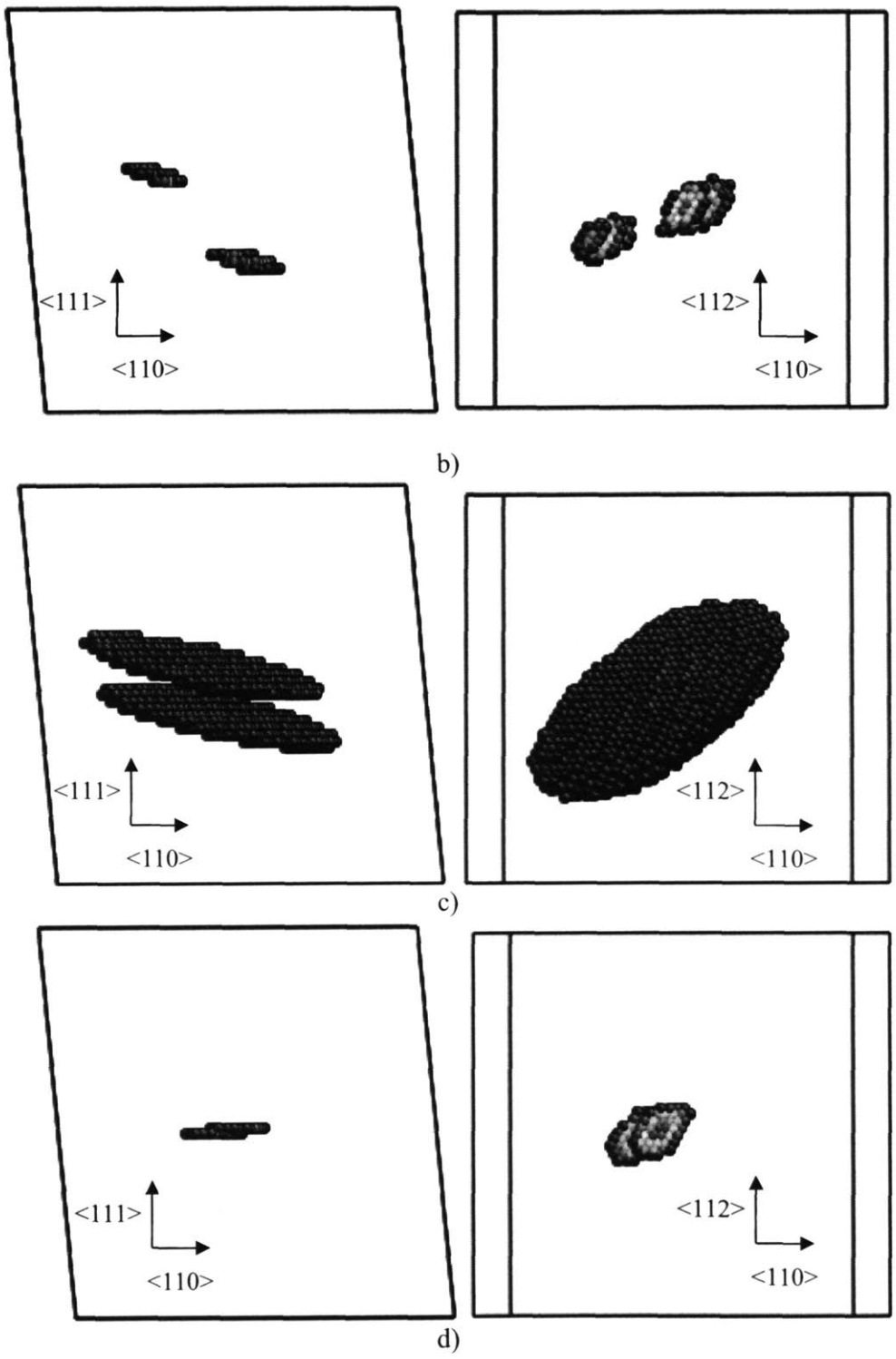

Figure 4-7: Atomistic configurations colored by the centrosymmetry parameter representing the four stages of wave steepening a) linear growth, b) non-linear growth, c) shear shock formation and d) atomistic defect formation.

The four stages observed in the initial three-dimensional shear localization process manifest themselves in the atomistic configurations associated with each displacement profile. The configuration in Figure 4-7a representing the linear growth stage is plotted with atoms colored according to the centrosymmetry parameter ranging from 6.7×10^{-17}, dark blue, to 1.3×10^{-12}, dark red. The fluctuation is directly related to the slope of the shear displacement wave. Consequently the break of symmetry is highest when the shear displacement is zero and relatively lowers near the peaks and valleys of the shear wave. Shear localization really begins as the magnitude of the shear displacement for chains normal to the emerging defect grows faster than those in the bulk, or far from the emerging defect. Localization continues as the shear wave in the material volume from which the defect eventually emerges goes non-linear. During the nonlinear growth stage the maximum centrosymmetry falls between the positions of chain A and chain B in the shear direction. The largest break in symmetry does not occur along the chains in the center of the newly forming defect but somewhat off-center where the break in symmetry between slip planes is augmented by the rapidly changing maximum shear displacement between one-dimensional chains. The atoms in Figure 4-7b have the largest centrosymmetry in the non-linear growth stage of chain A, ranging from 8.5×10^{-11} to 9.3×10^{-11}. These particles lie in front of and behind chain A in the slip direction and span several {111} planes above and below the rapidly forming discontinuity in the displacement profile of chain A. Shear shock formation is a metastable stage where the shear displacement wave has become discontinuous but the surrounding elastic body has not fully relaxed. As a result the configuration in Figure 4-7c shows the particles with highest centrosymmetry (2.0×10^{-9} to 9.0×10^{-9}) not yet fully localized to the slip plane containing the emerging defect. Lastly an in plane shear perturbation with local centrosymmetry ranging from 1.0×10^{-5}, dark blue, to 4.0×10^{-5}, dark red represents a atomistic defect formation for the chains normal to the atoms rendered in Figure 4-7d.

4.5 Structurally-Defined Shear Localization at a Vacancy

To this point we have solely considered homogeneous dislocation loop nucleation, nucleation from an initially perfect crystal, under an affine strain state. While homogeneous nucleation serves as a valid foundation for discussion of plastic deformation mechanisms, the richness of the field lies in a vast array of potential heterogeneous processes. Furthermore, although we have

shown that a larger range of stresses than expected exists over which homogeneous nucleation is feasible, heterogeneous nucleation is typically energetically favorable compared to the homogeneous process and as such may be deemed of more practical importance. In this section the consequences of introducing a single vacancy into the previously perfect crystal will be discussed within the framework of the wave steepening description for shear localization.

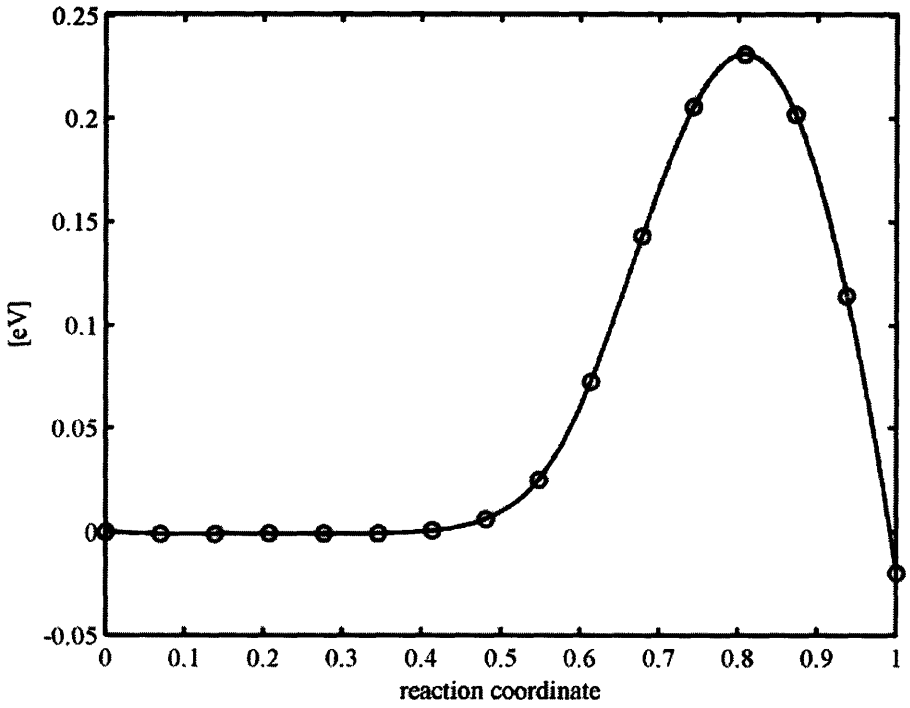

Figure 4-8: The reaction pathway for dislocation nucleation at a vacancy, calculated with the CINEB method and the free-end algorithm, provides the energy (open circles) and atomistic configurations for a series of images for use in the three-dimensional wave-steepening analysis.

We have performed a CINEB simulation for dislocation nucleation in a Cu lattice with a single vacancy under a <110>{111} shear strain of 0.112 such that the activation energy is equal to 0.37 eV. The initial vacancy configuration was created by removing a single particle from the perfect crystal lattice. The atomistic configuration was then relaxed using the conjugate gradient method [87] at constant strain. Further input configurations were obtained via low-temperature (0.0001 K) MD simulations at a stress above the athermal threshold. The Mishin Cu potential was used for energy and force calculations in both MD and CINEB calculations. Again the density of image configurations was biased towards the portion of the path prior to the saddle point. The image density is maintained due to the decoupled "climbing image" saddle point

configuration. The resulting relaxed reaction pathway, plotted in Figure 4-8, is terminated before reaching a stable minimum. The final configuration was relaxed using the free-end algorithm [63].

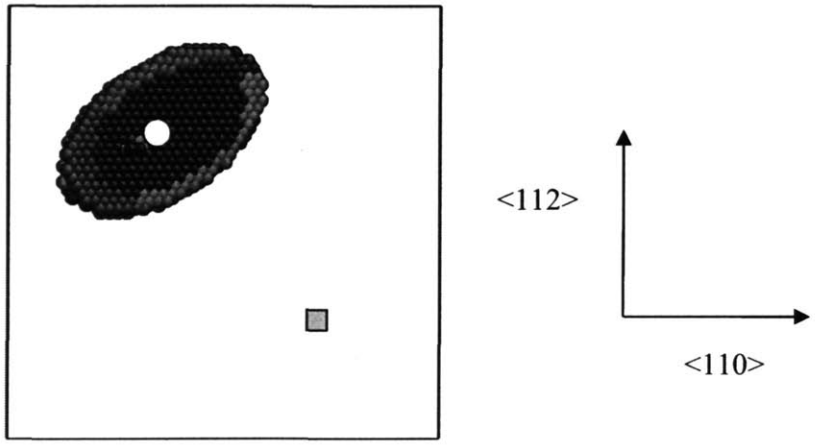

Figure 4-9: The positions relative to the emerging defect for the two one-dimensional chains used in the analysis of dislocation nucleation at a vacancy are shown as a white circle, chain A_{vac}, and a green square, chain B_{vac}. Chain A_{vac} passes through the crystal adjacent to the vacancy while chain B_{vac} is as far from the vacancy as possible considering the periodic boundary condition.

Following the three-dimensional analysis described in the previous sections, we define two one-dimensional chains of interests. The position of chain A_{vac}, passing through a particle adjacent to the vacancy and in the center of the emerging dislocation loop, is shown as a white dot in Figure 4-9. Chain B_{vac}, located at the green square in Figure 4-9, was chosen to be as far as possible from chain A_{vac} through the periodic boundary. Taking the relaxed vacancy configuration from R_1 as our reference, the displacement profiles for the two representative chains are plotted in Figure 4-10 where the displacement of each particle in chain A_{vac} is plotted as a black point and the displacement of particles in chain B_{vac} are plotted as green squares.

In Figure 4-10a the displacement profile for R_5 exhibit the linear growth of a shear displacement wave whose period is the length of the system in the <111> direction. the displacement at R_1 is also plotted as a reference. However, in contrast to the homogeneous case some local atomic relaxation around the vacancy is also observed in chain A_{vac} as the system

evolves along the path. The vacancy sits in the plane whose normalized <111> position is 0.78. The local atomic relaxation takes the form of a shear perturbation in the range of normalized <111> positions roughly between 0.6 and 0.9. By R_6 the relaxation has resulted in what appears to be non-linear growth in chain A_{vac} which is shown in Figure 4-10b. However, the non-linear growth occurs in the localized perturbation near the vacancy while far from the vacancy in the <111> direction, the evolution of the system has stalled. The higher frequency perturbation in the vicinity of the vacancy wins out over the longer wavelength perturbation. Moving farther along the path the displacement profile for chain A_{vac} then precedes to shear-shock formation at R_7 in Figure 4-10c. The final localization processes, shear shock and eventually atomistic defect formation, at R_9 in Figure 4-10d, revert to the length scale observed in the example of homogeneous nucleation. While the initial stages of the wave steepening behavior seem to be compressed into the material volume near the vacancy, the relaxation normal to the final dislocation or stacking fault is equivalent regardless of whether the defect was nucleated heterogeneously or homogeneously.

Our interest is to discuss the concept of stress concentration from a structural point of view within the one-dimensional chain framework. An important observation comes by taking the perfect crystal with a particle removed prior to relaxation as the reference state for calculation of the atomic displacements for each chain. In this reference frame the initial configuration, a vacancy relaxed under a <110>{111} shear strain of 0.112, contains nonzero shear displacements. Chain A_{vac}, for the initial configuration, exhibits in Figure 4-11 a displacement profile equivalent to the third stage of the wave steepening process (shear shock formation). If the behavior of the system is observed relative to the perfect crystal reference, we see the linear growth of the shear displacement waves in each chain. However, the localization to chain Avac has been assured. Where in the homogeneous case we have observed preferential linear growth followed by non-linear growth and shear shock formation, chain A_{vac} proceeds directly from the shear shock already created by local atomic relaxation near the vacancy towards the formation of a dislocation loop. The choice of an equivalent reference frame (the perfect crystal) allows for a clearer picture of the effects of a vacancy in the lattice on shear localization.

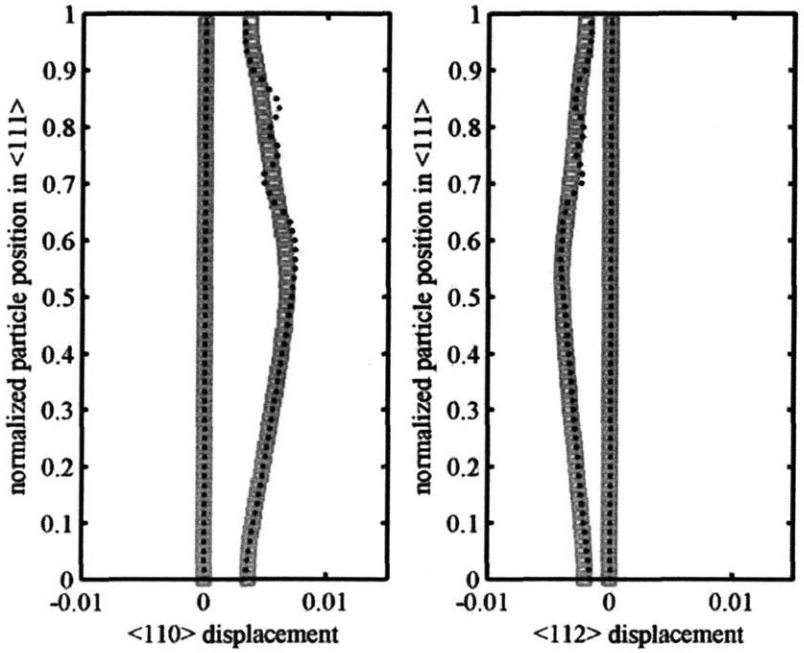
normalized particle position in <111>
<110> displacement
<112> displacement
1
0.9
0.8
0.7
0.6
0.5
0.4
0.3
0.2
0.1
0
-0.01
0
0.01

a)

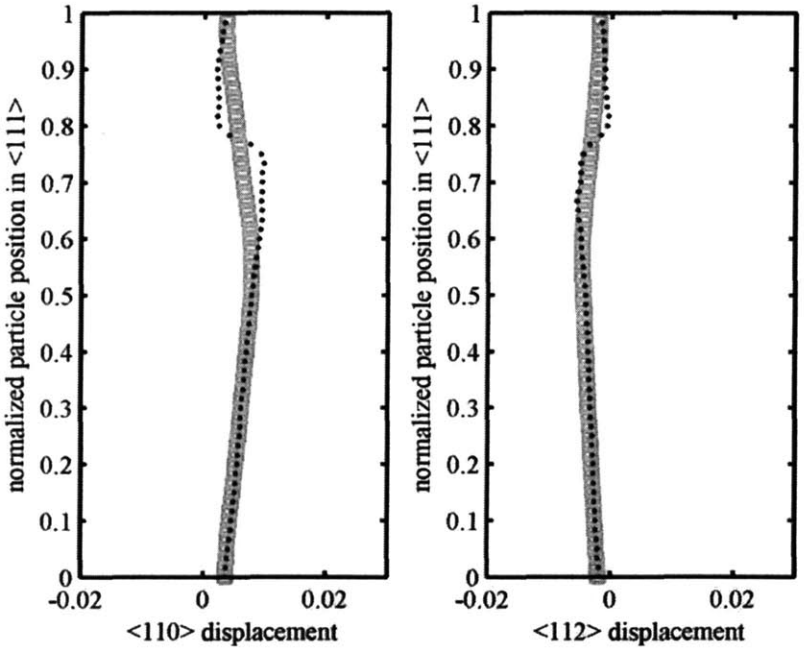
normalized particle position in <111>
<110> displacement
<112> displacement
1
0.9
0.8
0.7
0.6
0.5
0.4
0.3
0.2
0.1
0
-0.02
0
0.02

b)

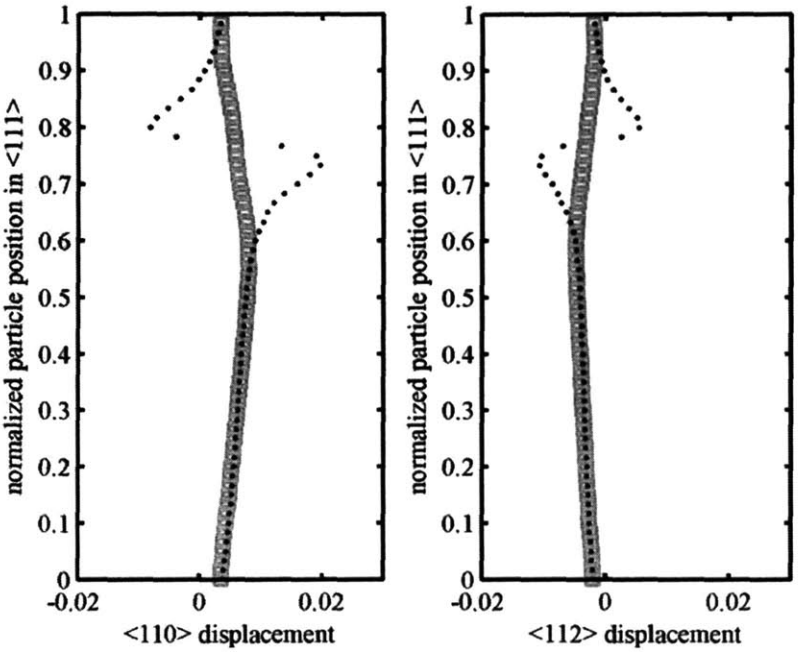

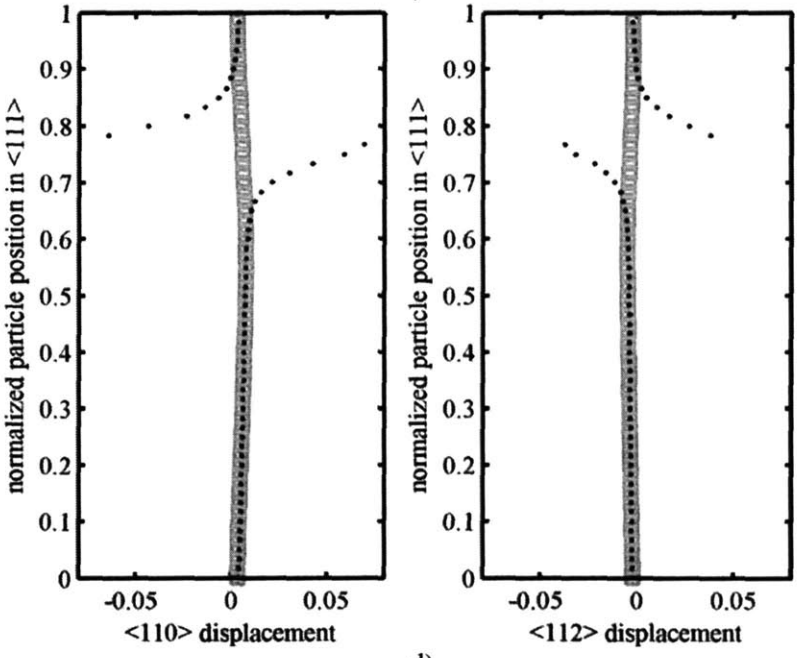

Figure 4-10: For each particle in chain A_{vac} (points) and chain B_{vac} (open squares) the displacement between the initial relaxed vacancy configuration and a series of images along the reaction pathway for dislocation nucleation exhibit the four stages of wave steepening. In the vicinity of the vacancy chain A_{vac} exhibits a) linear growth of local shear displacement wave (R_1 and R_5) b) non-linear growth (R_6), c) formation of a shear shock (R_7) and ultimately d) atomistic defect nucleation (R_9). Displacements are given in units of angstroms.

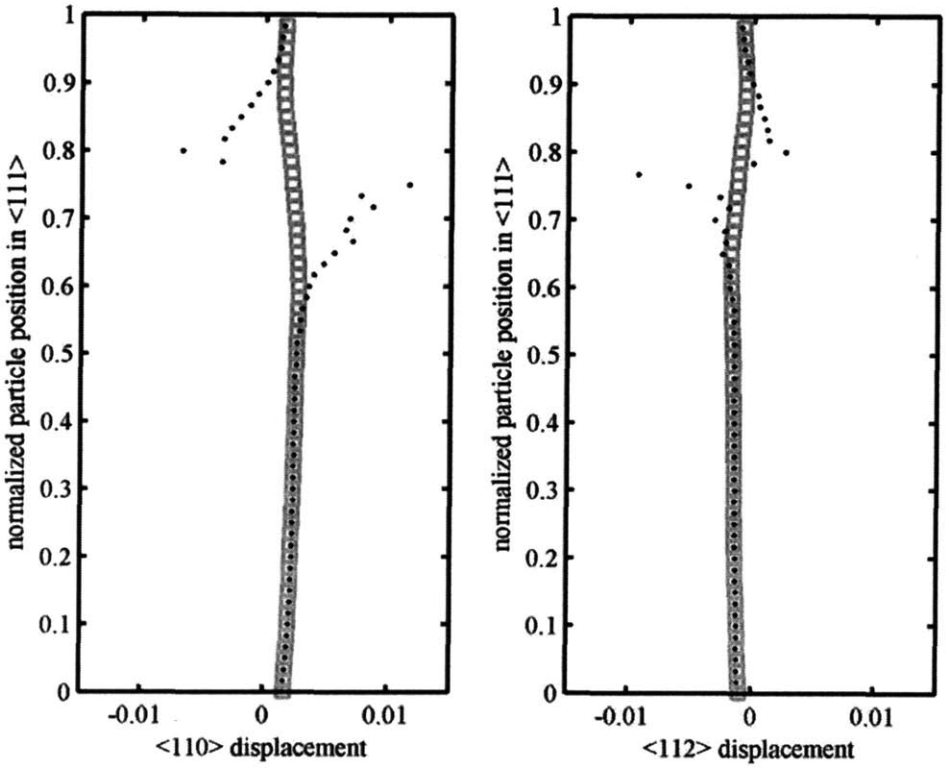

Figure 4-11: Displacement profile at both chain A_{vac} and chain B_{vac} for the initial configuration along the reaction pathway taking a perfect FCC lattice as the reference configurations. All displacements are in angstroms.

The "shear shock" associated with the atomic relaxation near the vacancy extends over the same range of <111> normalized positions, 0.6 to 0.9, for which we have observed in Figure 4-10 the localized wave-steepening when considering the system relative to the relaxed vacancy. Although referencing the perfect crystal, as in Figure 4-11, provides insight into the lattice's behavior, the more accurate picture involves the competition of the long and short wavelength shear perturbations. A volume smaller than the simulation cell is destabilized by the presence of the vacancy, and the four stages of wave-steepening are observed in this local region. The introduction of a vacancy overwhelming predisposes the lattice towards nucleation at the vacancy site because some degree of shear localization has already occurred prior to any evolution of the applied shear strain.

4.6 Conclusions

In this chapter we have discussed the process of shear localization in a three-dimensional crystalline lattice of FCC Cu. We have adopted the wave-steepening behavior proposed by Chang for a model one-dimensional system of slip planes constrained to move as rigid units and expanded the description for use in a system containing full atomistic degrees of freedom. The three-dimensional analysis requires the division of a system into a two-dimensional grid of one-dimensional chains normal to the slip plane of the emerging shear defect which is a surprisingly robust description of the localization behavior in a three-dimensional system.

In the case of homogeneous dislocation nucleation each one-dimensional chain follows the generic wave steepening behavior. The first instance of shear localization occurs as chains in the vicinity of the emerging defect proceed more quickly through the stages of wave steepening. The magnitude of the linear growth at some chains exceeds others and progresses more quickly to non-linear behavior. Localization stalls the progress of chains far from the more active region while a subset of the lattice proceeds through non-linear growth, shear shock formation and finally atomistic defect formation. As a dislocation loop sweeps out more area in the slip plane, the chains normal to the advancing dislocation loop proceed through the wave steepening behavior. The single description initially observed in a one-dimensional chain model accurately describes the fully atomistic static reaction pathway for the shear localization process in a perfect crystal.

We have also used the wave-steepening model to provide a structural description of the effect of heterogeneities on the process of shear localization. The dominance of heterogeneous processes over their homogeneous counterparts is well documented. Here a single vacancy is shown to predispose the crystalline lattice towards dislocation nucleation. In one view the introduction of the vacancy itself constitutes an atomistic defect and the vacancy's signature in terms of shear displacement relative to the perfect crystal lattice preempts the first several stages of the wave steepening process. The more rigorous view is taken from the reference of the relaxed vacancy which constitutes the initial equilibrium image configuration in the CINEB simulations. While in a homogeneous system the onset of shear localization occurs when a single

chain grows preferentially relative to the rest of the system and proceeds to non-linear growth, the local atomic relaxations associated with a vacancy serve to break the shear displacement wave for the chains containing particles adjacent to the vacancy. As a result, shear localization in the chains near the vacancy is significantly favored over any other region in the crystal. Furthermore the four stages of wave steepening are observed for a higher frequency shear perturbation localized to the portion of each one-dimensional chain passing through the material volume surrounding the vacancy. A single vacancy is perhaps only a model nucleation site; however, the observed behavior highlights two properties of shear localization in heterogeneous systems. First the presence of a lattice defect destabilizes a local region compared to the bulk crystal and allows for shorter wavelength modes. Secondly, at least for a vacancy, even these localized modes follow the three-dimensional wave steepening behavior we have depicted in this work which indicates that these four stages constitute a robust description of shear localization in material deformation.

Chapter 5

Effects of Heterogeneity on Activation

5.1 Introduction

In general real materials contain a large number and variety of defects relative to the perfect crystal lattice due to processing or as a consequence of extended use. At every scale, from point defects to free surfaces, defects can act as stress concentrators and heterogeneous sources of plastic deformation via dislocation nucleation or other mechanisms. Particularly in ductile metals the concerted action of many such sources is required to produce macroscopic deformation or eventual materials failure. The proceeding sections contain a few examples of the defect processes that are accessible to analysis via the NEB method. In general our interest is to discuss how the presence of defects affects the nucleation of a partial dislocation loop similar to the homogeneously nucleated defect in chapter two. The activation energy is taken as a measure of the tendency for nucleation in comparison to the homogeneous case. Furthermore we will discuss the effects of symmetry and local atomic structure on thermal activation.

5.2 Vacancy-Mediated Activation for Dislocation Nucleation

We have already shown that the local atomic relaxation associated with a vacancy provides sufficient lattice disruption to prescribe shear localization in an adjacent slip plane. While the structural description provides insight into the mechanism for this localization process,

understanding the ability of a vacancy to enhance plastic deformation via nucleation events is directly related to the energetics of the process. Another point of interest is the ability of a vacancy to modify the stress-dependent behavior observed for homogeneous dislocation loop nucleation.

Molecular dynamics simulation of high strain-rate <112>{111} simple shear was performed on a FCC Cu lattice containing 161279 particles and a single vacancy. Even with a vacancy multiple dislocations, one on each slip plane adjacent to the point defect, are nucleated almost simultaneously. To avoid the nucleation of multiple dislocations, we effectively quench the temperature of the MD simulation from 10 K to 0.0001 K and lower the strain immediately following the creation of the initial nucleate. Lowering the stress decreases the driving force for any further nucleation events to occur, particularly compared to the available thermal energy at 0.0001 K. In this way a single partial dislocation loop is formed and we can compare the activation energy of a homogeneous and a heterogeneous process which result in identical dislocation loops.

The FCC arrangement of particles into a crystalline lattice constitutes a stable configuration in Cu for all stresses below τ_{ath}; therefore, in the case of homogeneous dislocation loop nucleation each NEB simulation takes an identical perfect crystal initial image configuration. However, the local atomic relaxation around a vacancy is a stress-dependent behavior. As a result the initial configuration for a series of CINEB simulations at increasing <112>{111} shear stress were each relaxed via the conjugate gradient method[87]. Another perspective is that the calculation of the activation energy for dislocation nucleation at a vacancy takes as its reference the stress-dependent sum of the energy for the 161,279 FCC atoms in the atomistic configurations and the vacancy formation energy for a single vacancy. A series of input image configurations for CINEB calculations can be obtained via linear interpolation between a conjugate-gradient relaxed vacancy and the MD-derived dislocation loop configuration. Here we again utilize the free-end algorithm [63] to limit the number of image configurations while maintaining a sufficient image density along the path. Nine image configurations were used in the calculations presented here.

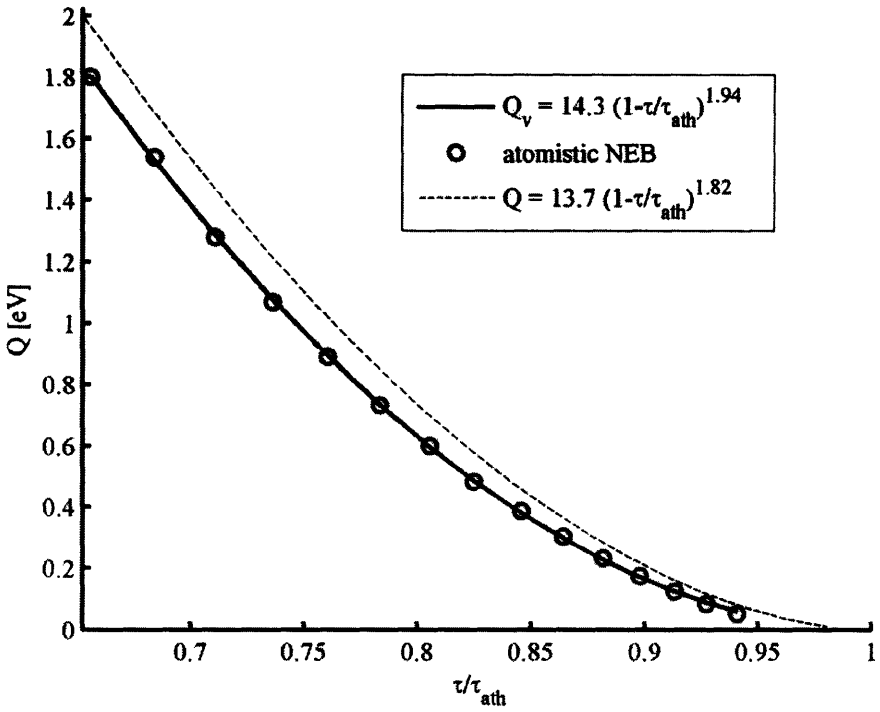

Figure 5-1: The activation energy for dislocation nucleation at a vacancy was calculated via the CINEB method (open circles) for a range of <112>{111} shear stresses, τ, and fit via the least-squares method to Equation 2.1 (solid black line). At all τ the vacancy-mediated activation energy is lower than the energy for homogeneous nucleation (dashed line).

We have plotted in Figure 5-1 the activation energy for dislocation nucleation at a vacancy versus the applied shear stress from CINEB calculations (open circles) and from a fit of the data to Equation 2.1 (solid line). The activation energy for homogeneous dislocation nucleation is also plotted as the previously presented fit to Equation 2.1 (dashed line). At every value of applied shear stress the activation energy is lowered by the presence of the vacancy. The shear stress in both cases is normalized by the appropriate athermal stress which is 3.78 GPa for homogeneous dislocation nucleation and 3.76 GPa for dislocation nucleation at a vacancy. The trend supports the structural observations made in the previous chapter using the one-dimensional chain model which indicate that the presence of the vacancy provides a higher frequency mode which fails in advance of the dominant mode in the homogeneous case.

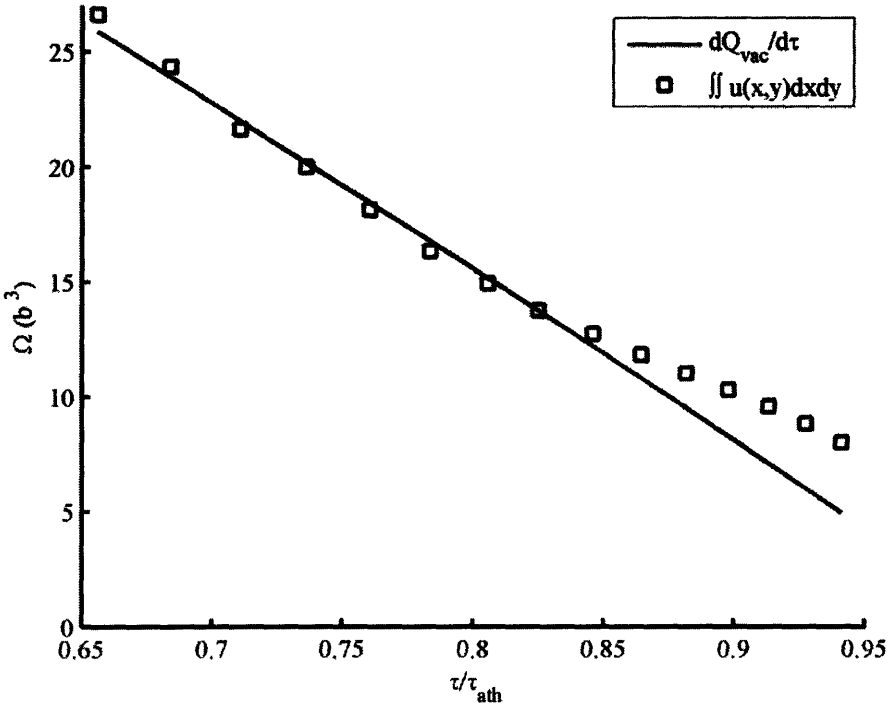

Figure 5-2: The activation volume calculated as the derivative of the activation energy (solid line) and the integral of the inelastic displacement in the slip plane (open squares) for dislocation nucleation at a vacancy show trends very similar to the observed behavior for homogeneous nucleation.

Following the analysis for homogeneous dislocation nucleation we have calculated the activation volume using both the structural definition given by Equation 2.4 and as the derivative of Q_{vac} w.r.t. τ. In Figure 5-2 the structural definition one again seems a reasonable quantitative approximation in the range of stress for which the saddle point is an in-plane shear perturbation with $0.5\ b_p < u_{max} < b_p$. However the general conclusion that the structurally defined activation volume is not an accurate reflection of the true stress dependence for activation is still observed for vacancy-assisted nucleation.

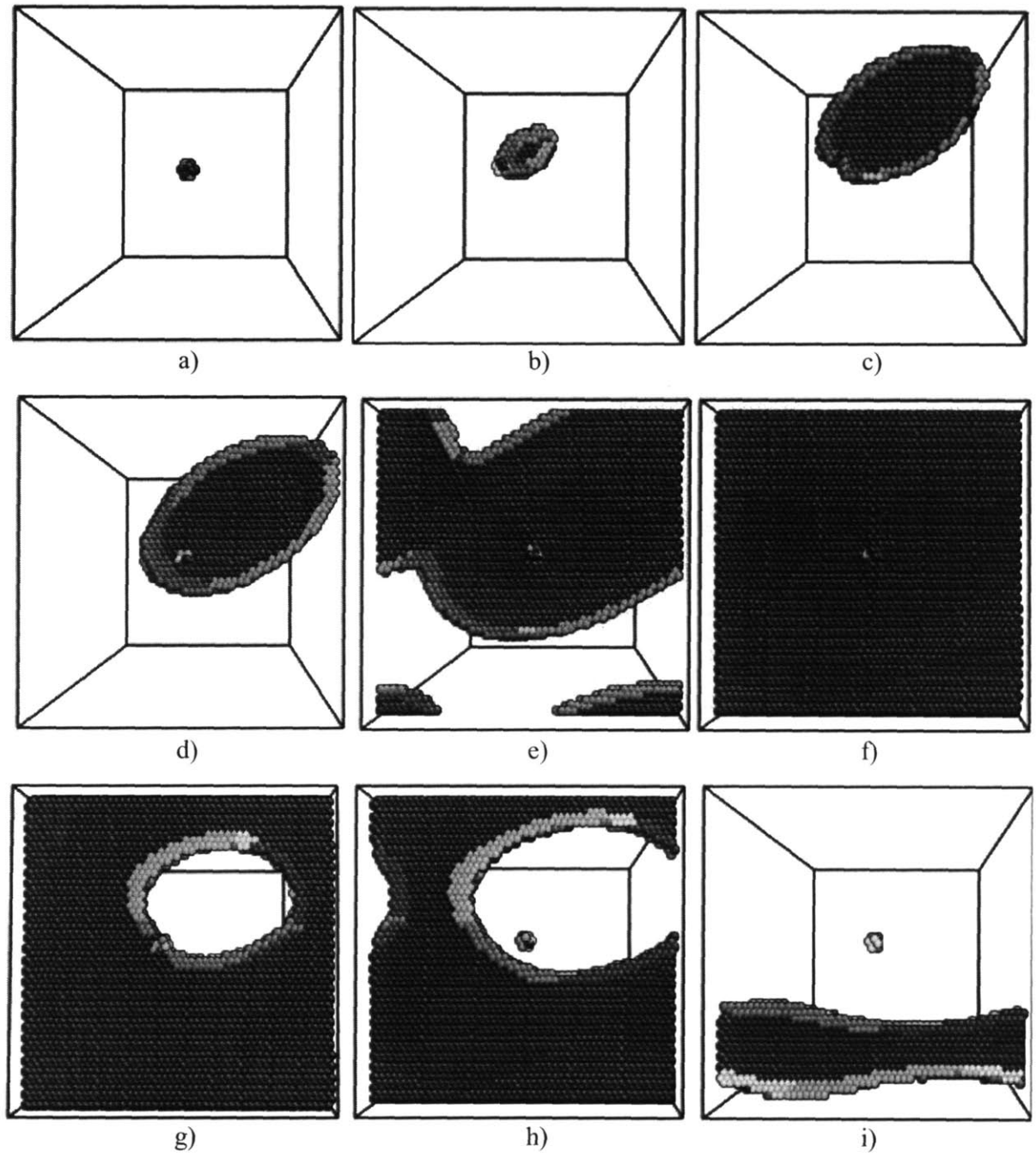

Figure 5-3: A series of snapshots from atomistic configurations along the pathway for dislocation nucleation at a vacancy reveal a behavior reminiscent of a Frank-Reed source. Centrosymmetry for all snapshots ranges from 0.037 to 0.26 with dark blue for the stacking fault (c.s. $\approx$ 0.04) and all other colors corresponding to the dislocation line or, as in a) the vacancy. An initial leading partial dislocation is b) nucleated, c) grows from the vacancy, d) finally breaks free from the point defect e) impinges on itself and f) annihilates to form a stacking fault from which g) a trailing partial dislocation is nucleated and grows to bow out at the vacancy before eventually h) breaking free of the dislocation and i) annihilating itself through the periodic boundary.

Seitz proposed in 1950 that large vacancy clusters confined to a single atomic plane or to a series of adjacent atomic planes (depending on the specific crystal structure) could collapse to form dislocation loops[88]. The model description of a dislocation loop as a cluster of vacancies has persisted [48, 89]; however, the validity of a single vacancy as a dislocation source was downplayed by Seitz. In Figure 5-3 we present a series of snapshots, colored by the centrosymmetry parameter, along the reaction pathway for dislocation loop nucleation at a vacancy under applied <112>{111} simple shear. Centrosymmetry for all snapshots ranges from 0.037 to 0.26 with the dislocation loop comprising the majority of the range and all the colors other than the dark blue associated with a stacking fault (c.s. $\approx$ 0.04). The vacancy exists in each configuration and is observable in Figure 5-3a because of the broken symmetry of the first nearest neighbor particles. The leading partial dislocation loop is nucleated at the vacancy in Figure 5-3b. Unlike the homogeneously nucleated dislocation described in Figure 2-2, the dislocation loop does not grow symmetrically from its origination point. In the homogeneous case the center of the dislocation loop does not travel as the loop glides in the slip plane. However, the partial dislocation nucleated at a vacancy is initially pinned to the vacancy at one end. As a result in Figure 5-3c the dislocation glides away from the vacancy at which it was nucleated. and the dislocation line is seen to bow out to either side of the vacancy. Uniform growth of the dislocation loop does not occur until the dislocation line wraps around the vacancy and the region pinned to the vacancy is annihilated in Figure 5-3d. Once the dislocation has broken free of the vacancy it impinges on itself through the periodic boundary in Figure 5-3e and annihilates to form a stacking fault in Figure 5-3f, which still contains the original vacancy. The vacancy exhibits similar interaction with the trailing partial dislocation in Figure 5-3g as it is nucleated and glides away from the vacancy in one direction while bowing around the vacancy in the other. The dislocation then breaks free in Figure 5-3h and eventually annihilates with itself through the boundary in Figure 5-3i leaving the original vacancy in its wake.

The behavior described above is almost exactly that of a Frank-Read source [90] where a dislocation line pinned at two points in a slip plane bows out under applied stress and eventually wraps around the pinning points to annihilate part of it's line length and break free as a fully formed dislocation loop. The action of many dislocations is necessary for ductile behavior. By allowing for the multiplication of a single pinned dislocation, dislocation sources, which can

repeatedly create dislocation loops under constant applied load, are necessary for the large degree of plastic deformation required for ductility in metals. While the presence of a vacancy in the lattice does not dramatically decrease the activation energy for dislocation nucleation, vacancies can act as valid, reusable dislocation sources. In the absence of other mechanisms, vacancy mediated dislocation nucleation may play a role in the plastic deformation of ductile metals.

5.3 Pore-Size Effects on Dislocation Nucleation

In the previous sections we have shown that the introduction of a single vacancy to a crystal lattice provides enhancement of the ability of the lattice to deform plastically via dislocation nucleation from both a structural and energetic perspective. However, the strength of the enhancement due to a vacancy compared to other heterogeneous processes is not obvious. A vacancy can be reasonably considered as the smallest possible void that can be introduced into an atomic lattice or perhaps more accurately as the smallest possible vacancy cluster where instead of a void radius or other geometric parameter, the number of vacancies is considered as the controlling parameter. Here we will explore the effects of increasingly large vacancy clusters on the activation energy for partial dislocation nucleation under a constant strain state.

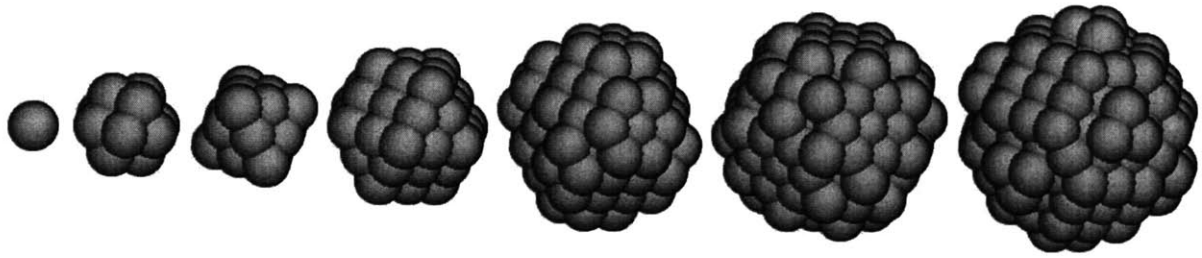

Figure 5-4: Increasingly large clusters of atoms were removed from a perfect crystal to create configurations with nearly spherical vacancy clusters. Each of these clusters is labeled with the number of particles it contains.

Starting from a perfect crystal of FCC Cu with 161,280 particles an increasingly large spherical void centered on an atomic position was removed. As a result the clusters removed from the perfect crystal correspond to the nearest neighbors, second nearest neighbors, etc. in the FCC structure and are 1, 13, 19, 55, 123, 177 and 225 particles in size. To illustrate the atomic configurations, Figure 5-4 shows the clusters of atoms removed for each of the seven configurations. Although the criterion for removal of particles was a sphere of increasing radius the shape of each vacancy cluster varies based on the intersection between a sphere and the discrete atomic positions in the FCC lattice. For each cluster size a MD simulation of <112>{111} simple shear deformation at 10K with a strain rate of 1×10^{9} s^{-1} was performed using the Cu Mishin potential in order to capture a dislocation nucleation event. Configurations just after the nucleation of a first dislocation loop were used as the input for a second run at 0.0001 K and a constant <112>{111} shear strain of 0.096. The second MD run serves to isolate the first nucleation event by quenching both temperature and stress as well as to remove thermal fluctuations which are not part of the relaxed pathway for the static NEB calculations.

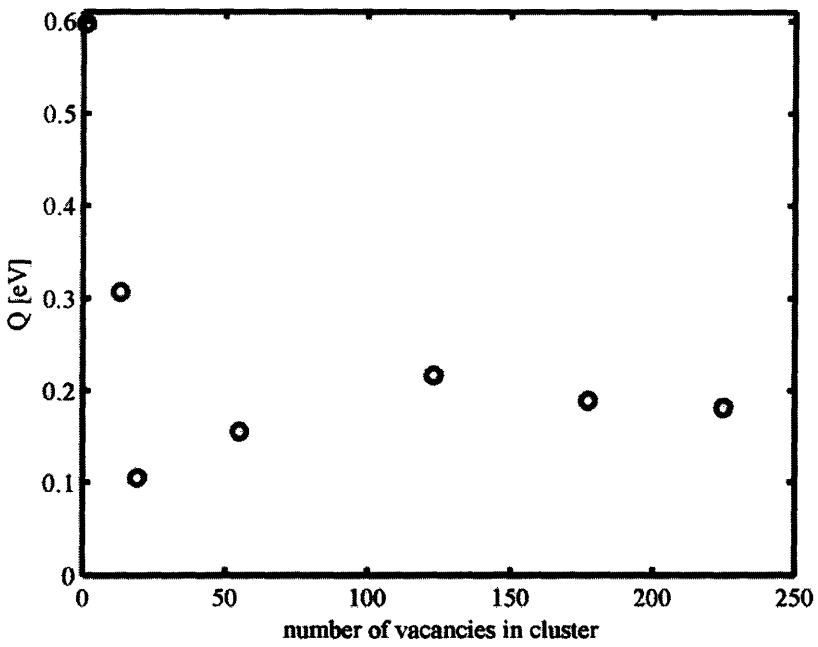

Figure 5-5: The activation energy for dislocation nucleation under constant <112>{111}shear stress strain for a series of increasingly large vacancy clusters indicates that the behavior is dominated by the surface symmetry and not the cluster size at atomic length scales.

From MD-derived atomistic configurations for dislocation nucleation at a series of increasingly large vacancy clusters, we have performed CINEB calculations under a constant <112>{111} simple shear strain of 0.096. Several observations can be made directly from the calculated activation energy in Figure 5-5 for dislocation nucleation at each of the vacancy clusters represented in Figure 5-4. First, all the multiple vacancy clusters provide a significant decrease in activation energy relative to both the perfect crystal and single vacancy processes. This confirms that the probability of perfect crystal or even lone vacancy mediated nucleation is relatively small compared to the likelihood of nucleation from larger-scale heterogeneous nucleation sites. Secondly, the activation energy is not solely related to some trend in the cluster size which is particularly obvious from the varied behavior of the smallest clusters. Third, the local structure at the surface of the vacancy clusters likely plays a dominant role in allowing for specific atomic processes for dislocation nucleation.

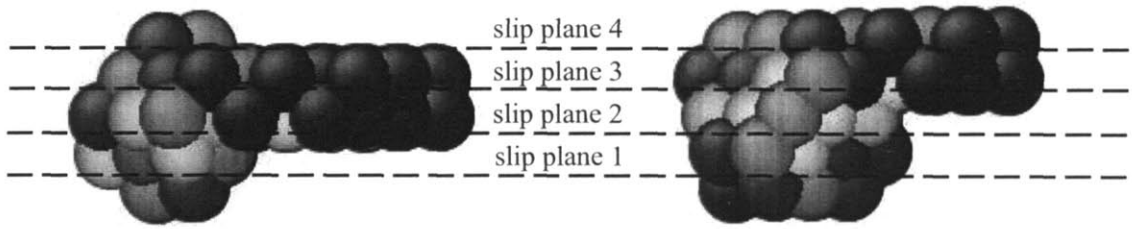

Figure 5-6: The saddle point configurations along the reaction pathway for dislocation nucleation at a) the 13 and b) 19 vacancy clusters are represented by the particles with non-FCC symmetry which include the dislocation loops and the atoms surrounding the cluster. In addition the four slip planes which intersect the cluster are represented by dashed lines.

Of particular interest is the dramatic difference in activation energy for the thirteen-particle and nineteen-particle clusters. Each of these clusters is contained within three adjacent {111} planes but the nineteen-vacancy cluster includes the addition of six second nearest neighbors. We are primarily interested in comparing the relaxation from the perfect crystal configurations to the initial vacancy cluster configurations used as the starting point for the reaction pathway for dislocation nucleation. In Figure 5-6 we examine the atomic representation of the vacancy clusters which are taken at the saddle point along the reaction pathway for the thirteen-vacancy

cluster (Figure 5-6a) and the nineteen-vacancy cluster (Figure 5-6b). Only particles where the FCC symmetry has been significantly disrupted are displayed. As a result the images in Figure 5-6 include the atoms surrounding the vacancy clusters as well as the atoms in the small dislocation loops emerging from the clusters.

In Figure 5-6 we have also labeled the four slip planes that intersect the thirteen and nineteen-vacancy clusters. The first observation is that the dislocation is nucleated in one of the two slip planes that intersect the center of the thirteen-vacancy cluster while in the nineteen-vacancy case we see the dominant nucleation event in the slip plane that intersects the top of the cluster. Both atomic planes adjacent to slip plane 3 contain vacancies while slip plane 4 is adjacent to one complete atomic plane and one containing six vacancies. In each slip plane, the relaxation surrounding the vacancy clusters under applied shear can be calculated in terms of shear displacement.

In order to determine the origin of the disproportionately large decrease in activation energy for the inclusions of vacancies in the second nearest neighbor positions, we have calculated the shear displacement profiles in the series of four slip planes. The displacement is calculated between the initially perfect crystal and the initial relaxed cluster configuration for the NEB calculations. The vacancy cluster is centered in each slip plane. In Figure 5-7 we present the shear displacement profiles in the <110> and <112> directions for each of the four slip planes highlighted in Figure 5-6 for the thirteen-vacancy cluster.

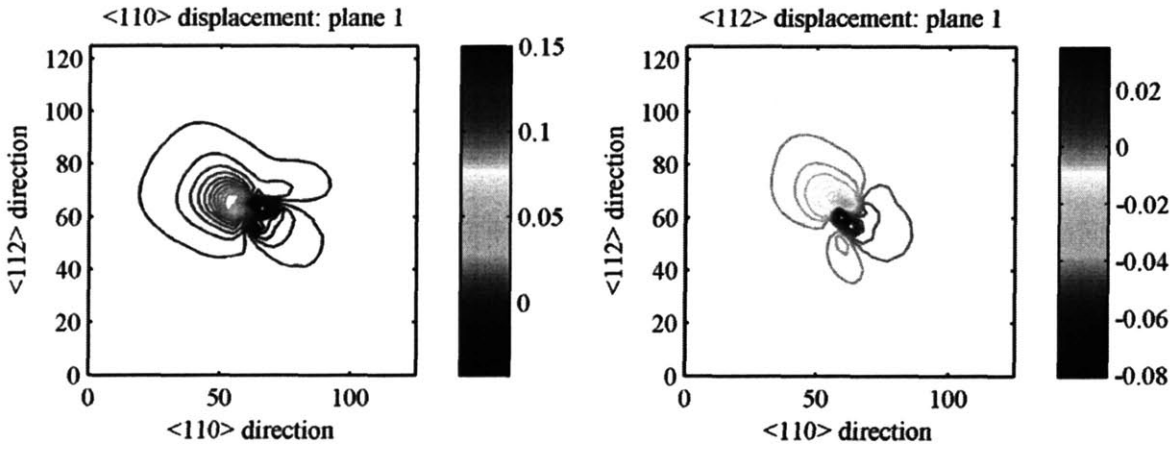

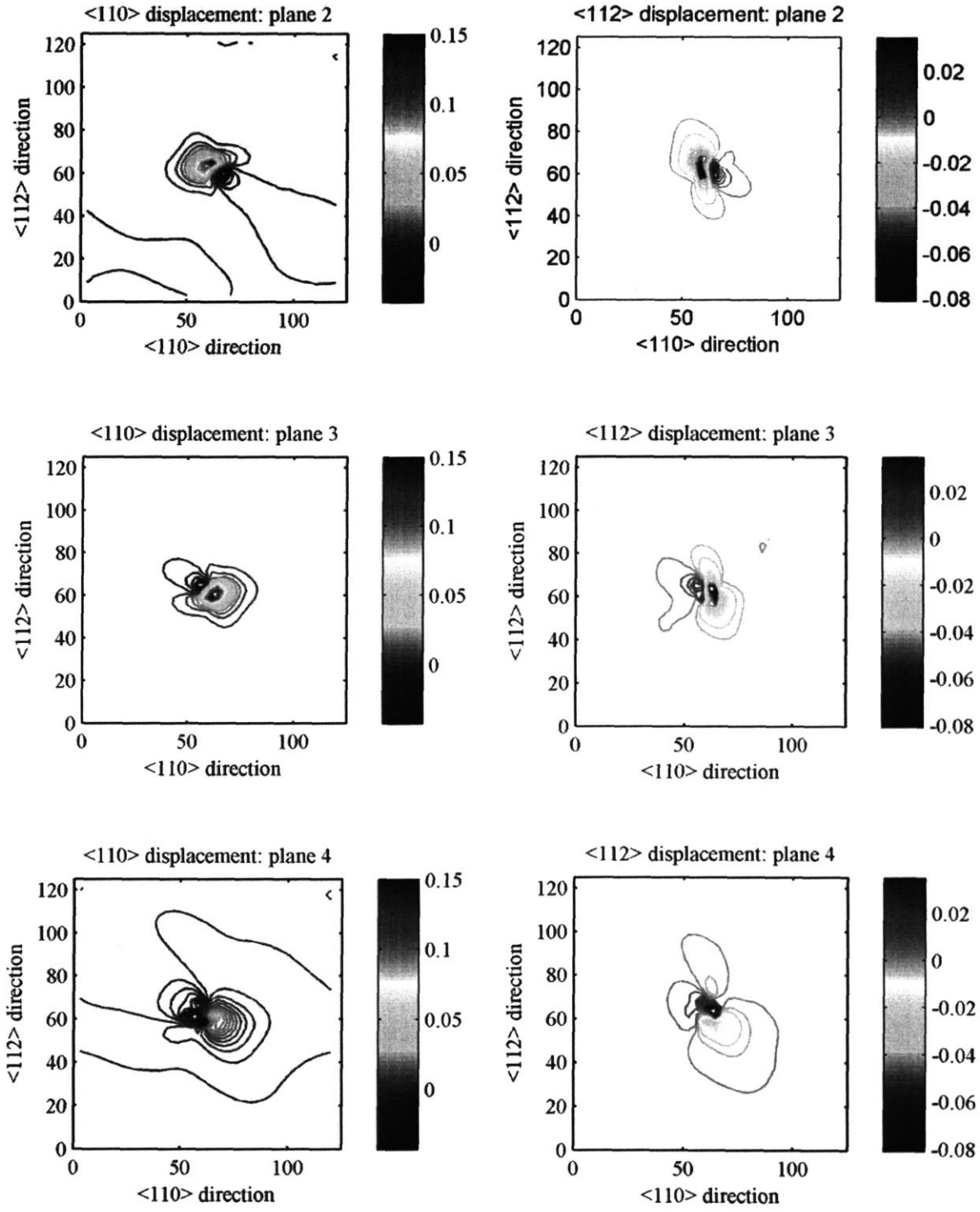

Figure 5-7: Displacement profiles for a series of parallel <111> slip planes intersecting the thirteen-vacancy cluster illustrate the local atomic relaxation near the cluster relative to a perfect crystal lattice.

We have in general referred to slip systems in our discussion using the notation for the generic families of slip planes and directions. However, in this case it is important to note that although the axis directions in the NEB simulations presented here are in the <110> family of directions, for the x-axis, and <112> family of directions, for the y-axis, the applied shear is not along the direction of the <112> axis. The <112> shear strain is applied at -30° to the positive <110> direction in the contours presented in Figures 5-7 and 5-8, which results in the nucleation of a partial dislocation whose Burger's vector is aligned along the same <112> direction.

Not surprisingly the maximum shear displacement due to the relaxation of the lattice around the thirteen-vacancy cluster occurs symmetrically in slip planes 2 and 3. Expansion of the shear displacement in plane 2 would produce a phantom dislocation within the vacancy cluster. As a result the initial dislocation nucleation event occurs in slip plane 3 where the propagation of the dislocation through the lattice decreases the shear strain in the system. Similarly, although nearly equivalent displacement profiles exist in slip planes 1 and 4 as a result of the nineteen-vacancy cluster, under the applied shear only the propagation of the shear displacement in slip plane 4 will relax the crystal lattice.

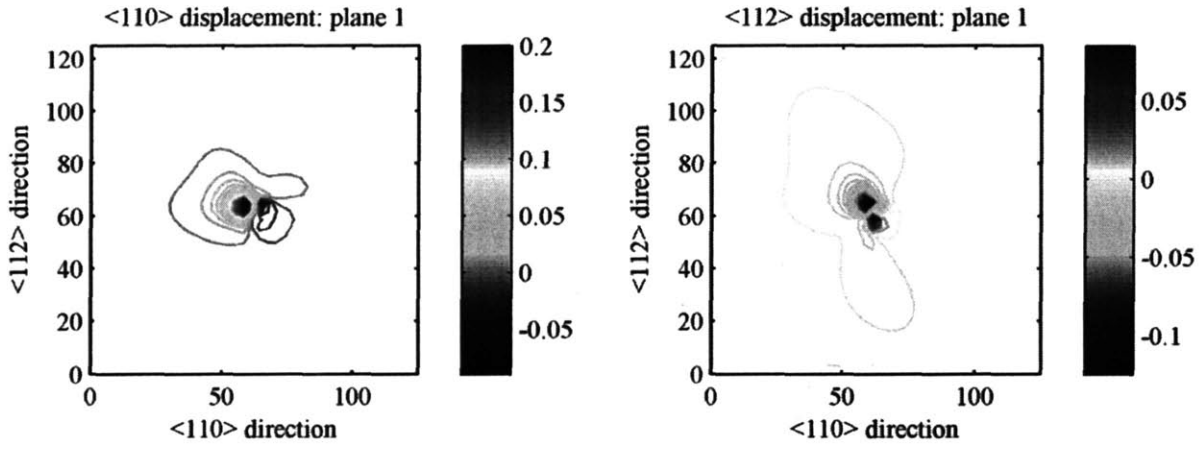

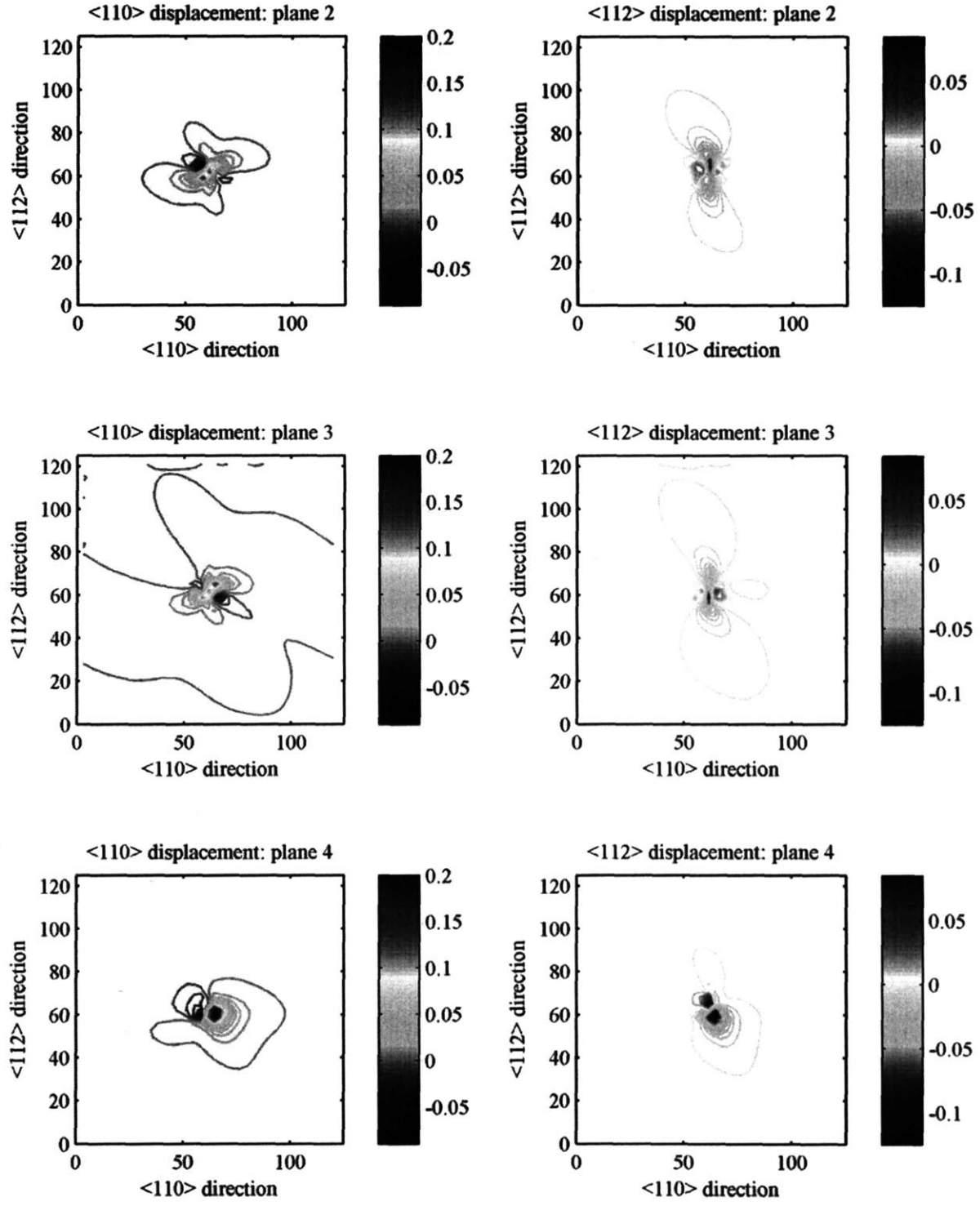

Figure 5-8: Displacement profiles for a series of parallel <111> slip planes intersecting the nineteen-vacancy cluster illustrate the local atomic relaxation near the cluster relative to a perfect crystal lattice.

The maximum shear displacement in slip planes 2 and 3 are similar for both the thirteen and nineteen-vacancy clusters. However, in the nineteen-vacancy cluster the maximum shear displacement in slip planes 1 and 4 in the shear direction due to the relaxation of the perfect crystal lattice is 0.24 Å versus 0.15 Å for slip planes 2 and 3. The inclusion of vacancies in the second nearest neighbor positions creates a much larger disruption to the local atomic lattice which predisposes nucleation in slip plane 4. The significantly increased shear displacement due to initial relaxation also lowers the energy necessary for the nucleation of a dislocation at the nineteen vacancy cluster.

5.4 Surface Nucleation in Nanowires

A cylindrical nanorod of FCC Cu was cut from an initially perfect crystal such that the axial direction of the rod is normal to a {111} slip plane. MD simulations produce an extremely high dislocation density. We have therefore initially deformed via MD simulation, at a strain rate of 1E9 s^{-1} and temperature of 10 K, a nanorod whose diameter, d, is 10.8 nm and whose axial length is only 3.13 nm. Periodic boundary conditions were used in the axial direction only. The small configuration size allowed for the isolation of a single dislocation nucleation event at an axial strain of 0.075. The isolated dislocation nucleate was then attached to a portion of defect free nanorod relaxed via the conjugate gradient method at the same applied strain to create a 25 nm long nanorod with a single dislocation nucleate. We have taken the 25 nm nanorod with periodic boundary conditions in the axial direction shown in Figure 5-9 as our sample for the current study, but in principle the method of spatially isolating a single dislocation nucleate allows for the study of an identical dislocation nucleation event in an increasing long nanorod. MD simulation cannot be relied upon to produce an isolated event for an arbitrarily large simulation cell at the applied stress required for nucleation. Further MD simulation allows for the growth of this single nucleate, although the simulations were performed using a periodic boundary condition in the axial direction so that the true system is an infinitely long nanorod with a periodic array of identical dislocations. For axial tensile loading a dislocation is nucleated at the surface of the nanorod on a {111} slip plane as shown in Figure 5-10 and glides through the interior of the nanorod to terminate in the surface leaving behind a stacking fault whose area is related to the geometry of the nanorod (area = $2\pi d^2$).

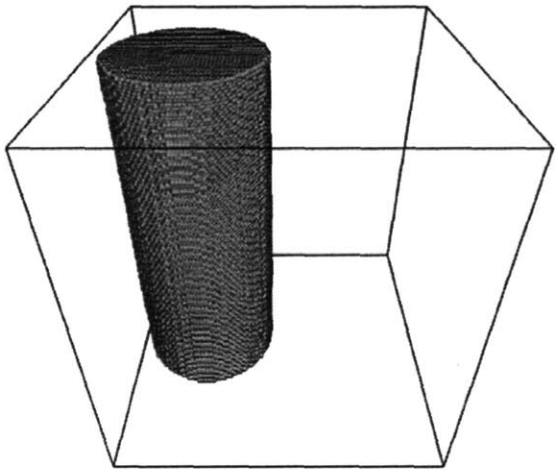

Figure 5-9: The nanorod configuration used for NEB calculations contains 205,480 particles and is initially 25 nm long and 10.8 nm in diameter.

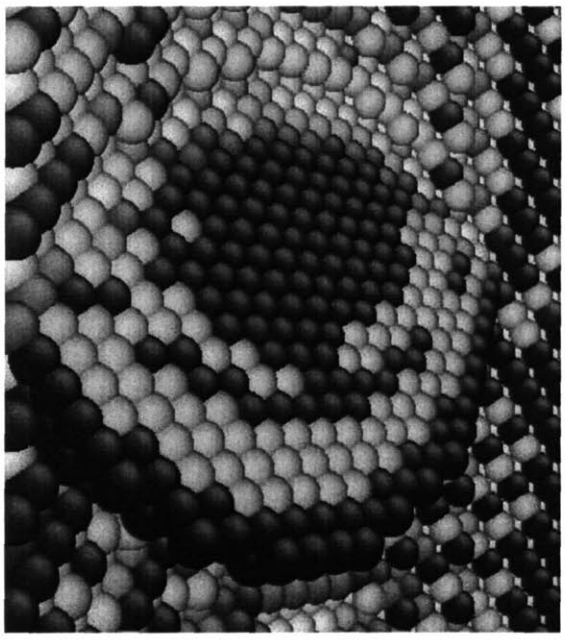

Figure 5-10: In the snapshot from an MD simulation, particles are colored according to the centrosymmetry parameter with all FCC particles removed to reveal a partial dislocation loop emerging from the surface of the nanorod and leaving a stacking fault in its wake.

Having isolated a single dislocation nucleation event from MD simulation we have everything we need to perform CINEB simulations of dislocation nucleation under applied tensile stress at the surface of a nanorod. Our interest however is to compare the nucleation of dislocations at a surface to the previous cases of shear driven nucleation in a perfect crystal and vacancy. The driving stress for dislocation nucleation is the shear stress in the activated slip system. The relationship between the resolved shear stress in the activated slip system, τ, due to the applied uniaxial tensile stress, σ, based on the geometry of the crystal lattice was initially laid out by Schmid [91]:

$$\tau = \sigma \cos\Phi \cos\lambda \tag{5.1}$$

where Φ is the angle between the tensile axis and the normal to the slip plane and λ is the angle between the tensile axis and the slip direction.

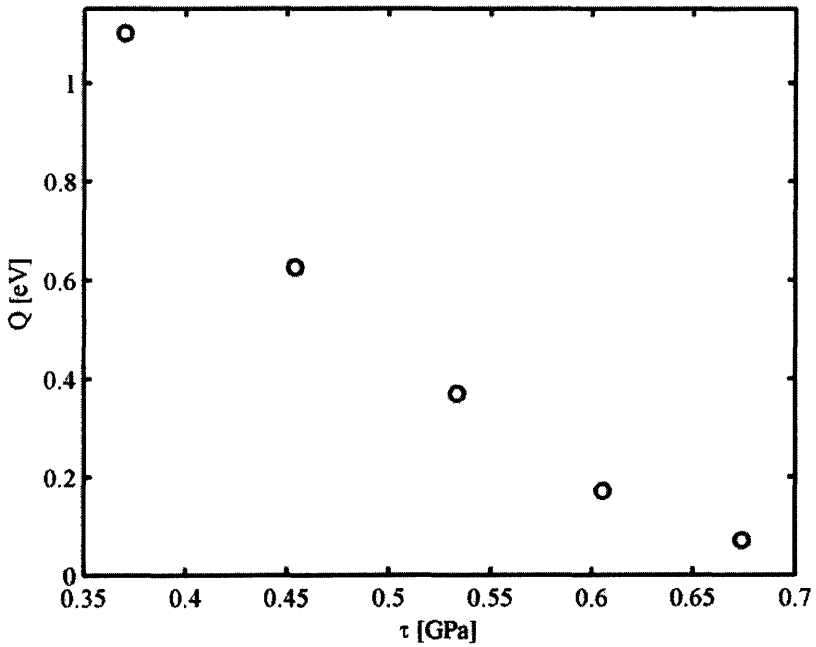

Figure 5-11: The activation energy for nucleation of a dislocation loop at the surface of a nanowire pulled in tension is plotted with respect to the resolved shear stress in the activated slip system.

The activation energy for dislocation nucleation at the nanorod surface is plotted in Figure 5-11 for a range of resolved shear stresses. The uniaxial stress in the initial configuration along the CINEB pathway for dislocation nucleation was taken as an approximation of the stress along the entire path. The shear stresses presented in Figure 5-11 were then derived from Equation 5.1 taking into account that for the activated <112>{111} slip system $\Phi = 70.3^\circ$ and $\lambda = 19.7^\circ$. The shear stress required to nucleate a dislocation at the nanorod surface under uniaxial tension is significantly lower than the driving stress observed for any of the previously discussed nucleation processes. However, direct comparison of the shear stress in the nanorod and the applied simple shear in the homogeneous and vacancy examples is inappropriate. Although the shear stress is the driving force for dislocation nucleation, the stress normal to the slip plane plays an important role in the magnitude of the shear stress required to slide the planes relative to one another. In simple shear for Cu, there is a compressive stress on the slip plane whereas the tensile deformation of the nanorod yields a non-trivial tensile stress on the slip plane in addition to the resolved shear stress. The disparity indicates a potential direction for future work involving further consideration of the effects of a general stress state on the activation energy for dislocation nucleation.

5.5 Conclusions

We have explored in this chapter a variety of heterogeneous processes which increase the propensity for dislocation nucleation in ductile metals such as Cu. In general the activation energy under applied simple shear has been used as a basis for comparison amongst the series of structural environments with steadily decreasing symmetry. We also expect that the examples given in this chapter are really the tip of the iceberg in terms of the dislocation processes which can be accurately described, in the framework of transition state theory, using the NEB or other reaction pathways sampling methods.

In particular we have shown that although a single vacancy is a relatively small heterogeneity, point defects being the smallest possible defect in a lattice, the activation energy for dislocation nucleation is decreased in the presence of a vacancy for any level of applied shear stress.

Furthermore a single vacancy can act as a reusable Frank-Read source. In the absence of other dislocation sources, vacancy mediated dislocation nucleation may play a role in the plastic deformation of ductile metals.

A series of nominally spherical vacancy clusters has provide several insights into the characteristics of a potent dislocation source. In general extended heterogeneities, larger in scale than a point defect, provide a significant decrease in activation energy relative to either perfect crystal or single vacancy nucleation sites. This confirms that the probability of perfect crystal or even lone vacancy mediated nucleation is relatively small compared to the likelihood of nucleation from larger-scale heterogeneous nucleation sites. However, the activation energy is not solely related to the size of the heterogeneous nucleation site. The lowest activation energy amongst the clusters studied occurred for a nineteen vacancy cluster. The local structure at the surface of the vacancy cluster, or perhaps more generally the degree of symmetry associated with a heterogeneous nucleation site, plays a dominant role in activation. Low-symmetry sites predispose the lattice towards defect nucleation by encouraging localized shear displacement to accommodate the local atomic structure.

Although a free surface is at least as well-suited to dislocation nucleation as a large vacancy cluster, the effect of the extended defect relative to the bulk crystal is overshadowed in our study by the variation in stress state. Although the shear stress in the activated slip system is the driving force for dislocation nucleation, the stress normal to the slip plane plays an important role in the magnitude of the shear stress required to slide the planes relative to one another. In the simple shear under which all other defects were studied, a compressive stress is exerted on the slip plane whereas the tensile deformation of the nanorod yields a non-trivial tensile stress on the slip plane in addition to the resolved shear stress. the athermal stress calculated for surface nucleation is a factor of five lower than the athermal stress for homogeneous nucleation. We believer the result is substantially affected by the differing applied stresses normal to the slip plane.

Conclusions

In this thesis we have discussed the stress-dependent behavior of dislocation nucleation in Cu in a variety of structural contexts. The coupling of MD simulations, for physically intuitive initial pathways, and the NEB method has allowed us to probe the static energy landscape provided by an empirical potential for both energetic and mechanistic information regarding systems at driving stresses extending far below the athermal stress. Within this framework we have explored a number of problems relating to the plastic deformation of FCC Cu via dislocation nucleation.

In chapter two we calculated the activation energy and activation volume for homogeneous dislocation nucleation under a range of applied shear stresses using fully atomistic CINEB calculations. Near the athermal stress most thermally-activated defect processes in plasticity cannot be considered as functions of a single parameter. Even a relatively simple process such as homogeneous dislocation nucleation requires consideration of both a loop radius and a maximum shear displacement. With atomistic NEB calculations we have found the exponent of the stress-dependent driving force for dislocation nucleation to be 1.82, because dislocation does not fully meet the single degree of freedom requirement for the derivation of a 3/2 model. The stress-dependence of the activation energy diverges from the expected behavior in part because of the spreading of in-plane shear perturbations with maximum displacements less than the Burger's vector. This behavior of the saddle point configuration for dislocation nucleation as the system approaches the athermal stress suggests that a transition from a discrete critical nucleate, large in degree but small in extent, to a diffuse critical nucleate, small in degree but large in extent, should be generically observed as thermally activated nucleation phenomenon approach the athermal driving force.

Homogeneous dislocation nucleation is typically ignored as a possible dislocation source because of the assumed large activation volume associated with creating a fully formed dislocation loop. Our atomistic simulations have shown that although the coordinated motion of one hundred or more atoms is required to nucleate a dislocation loop, for a large range of shear stresses below τ_{ath} the local shear displacement associated with most atoms is very small relative

to the partial Burger's vector. Low activation energy due to smaller than expect contribution from the particles involved lends credence to the idea that homogeneously nucleated dislocation loops could be responsible for plasticity in idealized conditions such as those available under nanoindentation. We have also shown that although, the structure of the saddle point configuration is typically purported to contain complete information regarding the stress-dependence for thermally activated defect processes, the commonly used structural definitions are insufficient to fully explain the behavior of the activation volume.

In chapter three we continue the discussion of stress-mediated activation with the implementation of a Peierls-Nabarro model for a circular in-plane shear displacement used in the NEB framework. However, the stress-dependence of the PN model is incommensurate with the atomistic results at least in part because near the athermal stress the failure mode for Cu corresponds neither to shear in a single slip plane nor to affine shear. Instead we have observed via atomistic calculation that an intermediate mode of shuffling slip planes, which is inaccessible to the PN model, is responsible for the lattice instability. However some observations have been made from the model. A closer look at the structure of the saddle point configuration from both atomistic and PN model reveals that, although the total activation volume tends toward a finite constant as the applied stress approaches the athermal stress, the maximum displacement decreases continuously to zero. The nearly constant structural volume is a result of high energy activation volume at the peak being replaced by low energy volume near the periphery of the defect as it expands in the plane. In the original conception of the term, all structurally defined activation volume contributed equally to the activation energy. However, when the saddle point configuration becomes an in-plane shear perturbation in fact not all activation volume is equal. Furthermore, the decreasing misfit energy and shear modulus with increased applied stress ensure that in general the energetic penalty for activated volume decreases as the applied stress rises. We have also observed, that holding constant the shear modulus increases the activation energy for at any level of applied shear stress. We expect that inclusion of the stress-dependent shear modulus may allow for improved accuracy in some previously formulated PN models for dislocation nucleation within the limitations of the model.

In chapter four we have discussed the generic process of shear localization in a three-dimensional crystalline lattice of FCC Cu. We have adopted the wave-steepening behavior proposed by Chang for a model one-dimensional system of slip planes constrained to move as rigid units and expanded the description for use in a system containing full atomistic degrees of freedom. Shear localization occurs in a perfect crystal as the magnitude of the linear growth of a shear perturbation normal to the slip plane in some chains exceeds the displacement in others and progresses more quickly to non-linear behavior. Localization stalls the progress of chains far from the more active region while a subset of the lattice proceeds through non-linear growth, shear shock formation and finally atomistic defect formation. The remainder of the crystal continues through the four stages as the dislocation line glides in the slip plane. While in a homogeneous system the onset of shear localization occurs when a single chain grows preferentially relative to the rest of the system, the local atomic relaxations associated with a vacancy serve to break the shear displacement wave for the chains containing particles adjacent to the vacancy. The presence of a vacancy destabilizes a local region compared to the bulk crystal and allows for localized, shorter wavelength modes which preferentially follow the four stages of wave steepening. The observation of these four stages in the shear localization process for both long wavelength shear perturbations in a perfect crystal and in localized shear modes near a point defect indicate that they constitute a robust description of three-dimensional shear localization.

While the perfect crystal provides an ideal model system for the study of the fundamental behavior of dislocations under shear, the majority of dislocation nucleation occurs heterogeneously. With this in mind, we have studied several heterogeneous dislocation nucleation processes in chapter five. First we have shown that while a single vacancy is perhaps only a model heterogeneous nucleation site, even the presence of a point defect decreases the activation energy for dislocation nucleation. Furthermore the dislocation nucleation mechanism at a vacancy is almost exactly the behavior of a Frank-Read source. Although this behavior has long been expected for extended vacancy clusters, the operation of such a vacancy source is seemingly novel. In the absence of other mechanisms, vacancy-mediated dislocation nucleation could play a role in the plastic deformation of ductile metals. We then proceeded to the study of dislocation nucleation at a series of nominally spherical dislocation clusters. Such extended

defects provide an increased propensity for dislocation nucleation compared to the perfect crystal or even point defects as observed by the relatively low activation volume for all the vacancy clusters studied. However, although a generic trend towards decreased activation energy with increasing cluster volume is observed, the largest decreases occurs for a nineteen vacancy cluster whose surface structure required anomalously large atomic relaxation under applied shear. In general we expect that any such symmetry breaking local atomic structure provides additional means for lowering the activation energy for dislocation nucleation. Lastly we calculated the activation energy for dislocation nucleation at the surface of a nanowire. Here the result was substantially affected by the tensile stress state. Although the shear stress in the activated slip system is the driving force for dislocation nucleation, the stress normal to the slip plane plays an important role in the magnitude of the shear stress required to slide the planes relative to one another. In simple shear for Cu, there is a compressive stress on the slip plane whereas the tensile deformation of the nanorod yields a non-trivial tensile stress on the slip plane in addition to the resolved shear stress. The action of many dislocations is necessary for ductile behavior. Dislocation sources that can repeatedly create dislocation loops under constant applied load, such as the heterogeneities discussed in this chapter, are necessary for the large degree of plastic deformation required for ductility in metals.

References

1. Xia, Z.C. and J.W. Hutchinson, *Crack tip fields in strain gradient plasticity.* Journal of the Mechanics and Physics of Solids, 1996. **44**(10): p. 1621-1648.

2. Spence, J.C.H., Y.M. Huang, and O. Sankey, *Lattice Trapping and Surface Reconstruction for Silicon Cleavage on (111) - Ab-Initio Quantum Molecular-Dynamics Calculations.* Acta Metallurgica Et Materialia, 1993. **41**(10): p. 2815-2824.

3. Silva, E.C.C.M., et al., *Atomic scale chemo-mechanics of silica: nano-rod deformation and water reaction.* Journal of Computer-Aided Materials Design, 2006. **13**(1-3): p. 135-159.

4. Wang, C.Z., et al., *Undissociated screw dislocation in Si: Glide or shuffle set?* Applied Physics Letters, 2006. **89**(5).

5. Van Swygenhoven, H., P.M. Derlet, and A.G. Froseth, *Stacking fault energies and slip in nanocrystalline metals.* Nature Materials, 2004. **3**(6): p. 399-403.

6. Rasmussen, T., et al., *Simulation of structure and annihilation of screw dislocation dipoles.* Philosophical Magazine a-Physics of Condensed Matter Structure Defects and Mechanical Properties, 2000. **80**(5): p. 1273-1290.

7. Farkas, D. and W.A. Curtin, *Plastic deformation mechanisms in nanocrystalline columnar grain structures.* Materials Science and Engineering a-Structural Materials Properties Microstructure and Processing, 2005. **412**(1-2): p. 316-322.

8. Li, J., et al., *Atomistic mechanisms governing elastic limit and incipient plasticity in crystals.* Nature, 2002. **418**(6895): p. 307-310.

9. Yamakov, V., et al., *Dislocation processes in the deformation of nanocrystalline aluminium by molecular-dynamics simulation.* Nature Materials, 2002. **1**(1): p. 45-48.

10. Lund, A.C. and C.A. Schuh, *Molecular simulation of amorphization by mechanical alloying.* Acta Materialia, 2004. **52**(8): p. 2123-2132.

11. Lund, A.C., T.G. Nieh, and C.A. Schuh, *Tension/compression strength asymmetry in a simulated nanocrystalline metal.* Physical Review B, 2004. **69**(1).

12. Boyer, R.D., et al., *Analysis of shear deformations in Al and Cu: empirical potentials versus density functional theory.* Modelling and Simulation in Materials Science and Engineering, 2004. **12**(5): p. 1017-1029.

13. Cheung, K.S. and S. Yip, *A Molecular-Dynamics Simulation of Crack-Tip Extension - the Brittle-to-Ductile Transition.* Modelling and Simulation in Materials Science and Engineering, 1994. **2**(4): p. 865-892.

14. Bulatov, V., et al., *Atomistic modeling of crystal-defect mobility and interactions.* Nuclear Instruments & Methods in Physics Research Section B-Beam Interactions with Materials and Atoms, 1997. **121**(1-4): p. 251-256.

15. Chang, J.P., et al., *Dislocation motion in BCC metals by molecular dynamics.* Materials Science and Engineering a-Structural Materials Properties Microstructure and Processing, 2001. **309**: p. 160-163.

16. Decelis, B., A.S. Argon, and S. Yip, *Molecular-Dynamics Simulation of Crack Tip Processes in Alpha-Iron and Copper.* Journal of Applied Physics, 1983. **54**(9): p. 4864-4878.

17. Allen, M.P. and D.J. Tildesley, *Computer simulation of liquids.* Oxford science publications. 1989, New York: Clarendon Press

18. Schiotz, J., F.D. Di Tolla, and K.W. Jacobsen, *Softening of nanocrystalline metals at very small grain sizes.* Nature, 1998. **391**(6667): p. 561-563.

19. Zhu, T., J. Li, and S. Yip, *Atomistic configurations and energetics of crack extension in silicon.* Physical Review Letters, 2004. **93**(20).

20. Zhu, T., J. Li, and S. Yip, *Atomistic study of dislocation loop emission from a crack tip.* Physical Review Letters, 2004. **93**(2).

21. Henkelman, G. and H. Jonsson, *Improved tangent estimate in the nudged elastic band method for finding minimum energy paths and saddle points.* Journal of Chemical Physics, 2000. **113**(22): p. 9978-9985.

22. Henkelman, G., B.P. Uberuaga, and H. Jonsson, *A climbing image nudged elastic band method for finding saddle points and minimum energy paths.* Journal of Chemical Physics, 2000. **113**(22): p. 9901-4.

23. Gao, F., et al., *Finding possible transition states of defects in silicon-carbide and alpha-iron using the dimer method.* Nuclear Instruments & Methods in Physics Research Section B-Beam Interactions with Materials and Atoms, 2003. **202**: p. 1-7.

24. Henkelman, G. and H. Jonsson, *A dimer method for finding saddle points on high dimensional potential surfaces using only first derivatives.* Journal of Chemical Physics, 1999. **111**(15): p. 7010-7022.

25. Sorensen, M.R., M. Brandbyge, and K.W. Jacobsen, *Mechanical deformation of atomic-scale metallic contacts: Structure and mechanisms.* Physical Review B, 1998. **57**(6): p. 3283-3294.

26. Vegge, T. and W. Jacobsen, *Atomistic simulations of dislocation processes in copper.* Journal of Physics-Condensed Matter, 2002. **14**(11): p. 2929-2956.

27. Zhu, T., J. Li, and S. Yip, *Atomistic characterization of three-dimensional lattice trapping barriers to brittle fracture.* Proceedings of the Royal Society a-Mathematical Physical and Engineering Sciences, 2006. **462**(2070): p. 1741-1761.

28. Vegge, T., et al., *Determination of the of rate cross slip of screw dislocations.* Physical Review Letters, 2000. **85**(18): p. 3866-3869.

29. Wen, M. and A.H.W. Ngan, *Atomistic simulation of kink-pairs of screw dislocations in body-centred cubic iron.* Acta Materialia, 2000. **48**(17): p. 4255-4265.

30. Zhu, T., et al., *Deformation and fracture of a SiO2 nanorod.* Molecular Simulation, 2003. **29**(10-11): p. 671-676.

31. Vineyard, G.H., *Frequency factors and isotope effects in solid state rate processes.* Journal of Physics and Chemistry of Solids, 1957. **3**(1-2): p. 121-127.

32. Ercolessi, F. and J.B. Adams, *Interatomic Potentials from 1St-Principles Calculations - the Force-Matching Method.* Europhysics Letters, 1994. **26**(8): p. 583-588.

33. Sankey, O.F. and D.J. Niklewski, *Abinitio Multicenter Tight-Binding Model for Molecular-Dynamics Simulations and Other Applications in Covalent Systems.* Physical Review B, 1989. **40**(6): p. 3979-3995.

34. Mishin, Y., et al. *Interatomic potentials for Al and Ni from experimental data and ab initio calculations.* 1999. Boston, MA, USA: Mater. Res. Soc.

35. Mishin, Y., et al., *Structural stability and lattice defects in copper: Ab initio, tight-binding, and embedded-atom calculations.* Physical Review B (Condensed Matter and Materials Physics), 2001. **63**(22): p. 224106-1.

36. Liu, X.Y., F. Ercolessi, and J.B. Adams, *Aluminium interatomic potential from density functional theory calculations with improved stacking fault energy.* Modelling and Simulation in Materials Science and Engineering, 2004. **12**(4): p. 665-670.

37. Ogata, S., J. Li, and S. Yip, *Ideal pure shear strength of aluminum and copper.* Science, 2002. **298**(5594): p. 807-811.

38. Boyer, R.D. and Massachusetts Institute of Technology. Dept. of Materials Science and Engineering., *Shear-induced homogeneous deformation twinning in FCC aluminum and copper via automistic simulation.* 2003. p. 80 leaves.

39. Cerny, M., et al., *Higher-energy structures and stability of Cu and Al crystals along displacive transformation paths.* Journal of Computer-Aided Materials Design, 2005. **12**(2-3): p. 161-173.

40. Feibelman, P.J., *Diffusion Path for an Al Adatom on Al(001).* Physical Review Letters, 1990. **65**(6): p. 729-732.

41. Robertson, I.J., V. Heine, and M.C. Payne, *Cohesion in Aluminum Systems - a 1St-Principles Assessment of Glue Schemes.* Physical Review Letters, 1993. **70**(13): p. 1944-1947.

42. Kioussis, N., et al., *Topology of electronic charge density and energetics of planar faults in fcc metals.* Physical Review Letters, 2002. **88**(12).

43. Zimmerman, J.A., H.J. Gao, and F.F. Abraham, *Generalized stacking fault energies for embedded atom FCC metals.* Modelling and Simulation in Materials Science and Engineering, 2000. **8**(2): p. 103-115.

44. Guanshui, X. and A.S. Argon, *Homogeneous nucleation of dislocation loops under stress in perfect crystals.* Philosophical Magazine Letters, 2000. **80**(9): p. 605-11.

45. Cottrell, A.H., *Dislocations and plastic flow in crystals.* 1953: Clarendon Press. 324.

46. Cahn, J.W. and F.R.N. Nabarro, *Thermal activation under shear.* Philosophical Magazine A (Physics of Condensed Matter: Structure, Defects and Mechanical Properties), 2001. **81**(5): p. 1409-26.

47. Khraishi, T.A., et al., *The stress field of a general circular Volterra dislocation loop: analytical and numerical approaches.* Philosophical Magazine Letters, 2000. **80**(2): p. 95-105.

48. Hirth, J.P. and J. Lothe, *Theory of dislocations.* 2nd ed. 1982, New York: Wiley. xii, 857 p.

49. Mason, J.K., A.C. Lund, and C.A. Schuh, *Determining the activation energy and volume for the onset of plasticity during nanoindentation.* Physical Review B, 2006. **73**(5).

50. Schuh, C.A., J.K. Mason, and A.C. Lund, *Quantitative insight into dislocation nucleation from high-temperature nanoindentation experiments.* Nature Materials, 2005. **4**(8): p. 617-621.

51. Zuo, L., A.H.W. Ngan, and G.P. Zheng, *Size dependence of incipient dislocation plasticity in Ni3Al.* Physical Review Letters, 2005. **94**(9).

52. Kocks, U.F., A.S. Argon, and M.F. Ashby, *Thermodynamics and kinetics of slip.* 1st ed. Progress in materials science ; v. 19. 1975, Oxford ; New York: Pergamon Press.

53. Xu, G., A.S. Argon, and M. Ortiz, *Nucleation of Dislocations from Crack Tips under Mixed-Modes of Loading - Implications for Brittle against Ductile Behavior of Crystals.* Philosophical Magazine a-Physics of Condensed Matter Structure Defects and Mechanical Properties, 1995. **72**(2): p. 415-451.

54. Rice, J.R. and G.E. Beltz, *The Activation-Energy for Dislocation Nucleation at a Crack.* Journal of the Mechanics and Physics of Solids, 1994. **42**(2): p. 333-360.

55. Schuh, C.A. and A.C. Lund, *Application of nucleation theory to the rate dependence of incipient plasticity during nanoindentation.* Journal of Materials Research, 2004. **19**(7): p. 2152-2158.

56. Van Vliet, K.J., et al., *Quantifying the early stages of plasticity through nanoscale experiments and simulations.* Physical Review B, 2003. **67**(10).

57. Zhu, T., et al., *Predictive modeling of nanoindentation-induced homogeneous dislocation nucleation in copper.* Journal of the Mechanics and Physics of Solids, 2004. **52**(3): p. 691-724.

58. Knap, J. and M. Ortiz, *Effect of indenter-radius size on Au(001) nanoindentation.* Physical Review Letters, 2003. **90**(22): p. 226102-1.

59. Wo, P.C., L. Zuo, and A.H.W. Ngan, *Time-dependent incipient plasticity in Ni3Al as observed in nanoindentation.* Journal of Materials Research, 2005. **20**(2): p. 489-495.

60. Choi, Y., et al., *Size effects on the onset of plastic deformation during nanoindentation of thin films and patterned lines.* Journal of Applied Physics, 2003. **94**(9): p. 6050-6058.

61. Kelchner, C.L., S.J. Plimpton, and J.C. Hamilton, *Dislocation nucleation and defect structure during surface indentation.* Physical Review B, 1998. **58**(17): p. 11085-11088.

62. Henkelman, G., B.P. Uberuaga, and H. Jonsson, *A climbing image nudged elastic band method for finding saddle points and minimum energy paths.* Journal of Chemical Physics, 2000. **113**(22): p. 9901-9904.

63. Zhu, T., et al., *From the Cover: Interfacial plasticity governs strain rate sensitivity and ductility in nanostructured metals.* PNAS, 2007. **104**(9): p. 3031-3036.

64. Cottrell, A.H., *The Nabarro equation for thermally activated plastic glide.* Philosophical Magazine, 2006. **86**(25-26): p. 3811-17.

65. Cottrell, A.H., *Thermally activated plastic glide.* Philosophical Magazine Letters, 2002. **82**(2): p. 65-70.

66. Lu, G., et al., *The Peierls-Nabarro model revisited.* Philosophical Magazine Letters, 2000. **80**(10): p. 675-682.

67. Cahn, J.W. and J.E. Hilliard, *Free energy of a nonuniform system. III. Nucleation in a two-component incompressible fluid.* Journal of Chemical Physics, 1959. **31**(3): p. 688-699.

68. Peierls, R., *The size of a dislocation.* Proceedings of the Physical Society, 1940. **52**(1): p. 34.

69. Nabarro, F.R.N., *Dislocations in a simple cubic lattice.* Proceedings of the Physical Society, 1947. **59**(2): p. 256.

70. Ngan, A.H.W., *A new model for dislocation kink-pair activation at low temperatures based on the Peierls-Nabarro concept.* Philosophical Magazine a-Physics of Condensed Matter Structure Defects and Mechanical Properties, 1999. **79**(7): p. 1697-1720.

71. Ngan, A.H.W. and H.F. Zhang, *Mobility of non-planar screw dislocations ahead of a mode III crack tip.* Mechanics of Materials, 1999. **31**(6): p. 367-379.

72. Xu, G., A.S. Argon, and M. Oritz, *Critical configurations for dislocation nucleation from crack tips.* Philosophical Magazine a-Physics of Condensed Matter Structure Defects and Mechanical Properties, 1997. **75**(2): p. 341-367.

73. Rice, J.R., *Dislocation Nucleation from a Crack Tip - an Analysis Based on the Peierls Concept.* Journal of the Mechanics and Physics of Solids, 1992. **40**(2): p. 239-271.

74. Lee, C.-L. and S. Li, *A half-space Peierls-Nabarro model and the mobility of screw dislocations in a thin film.* Acta Materialia, 2007. **55**(6): p. 2149-2157.

75. Bulatov, V.V. and E. Kaxiras, *Semidiscrete variational Peierls framework for dislocation core properties.* Physical Review Letters, 1997. **78**(22): p. 4221-4224.

76. Schoeck, G., *The core structure of «001» dislocations in bcc metals.* Philosophical Magazine Letters, 1997. **76**(1): p. 15 - 24.

77. Vitek, V., *Stacking faults on {111} and {110} planes in aluminium.* Scripta Metallurgica, 1975. **9**(6): p. 611-615.

78. Vitek, V., *Intrinsic stacking faults in body-centred cubic crystals.* Philosophical Magazine, 1968. **18**(154): p. 773-86.

79. Xu, D.S., et al., *Atomistic simulation of the influence of pressure on dislocation nucleation in bcc Mo.* Computational Materials Science, 2006. **36**(1-2): p. 60-64.

80. Li, J., et al., *Core energy and Peierls stress of a screw dislocation in bcc molybdenum: A periodic-cell tight-binding study.* Physical Review B, 2004. **70**(10).

81. Lu, G., et al., *Generalized-stacking-fault energy surface and dislocation properties of aluminum.* Physical Review B, 2000. **62**(5): p. 3099-3108.

82. Khraishi, T.A., et al., *The displacement, and strain-stress fields of a general circular Volterra dislocation loop.* International Journal of Engineering Science, 2000. **38**(3): p. 251-266.

83. Li, J. and S. Yip, *Atomistic measures of materials strength.* Cmes-Computer Modeling in Engineering & Sciences, 2002. **3**(2): p. 219-227.

84. Clatterbuck, D.M., et al., *Phonon instabilities and the ideal strength of aluminum.* Physical Review Letters, 2003. **91**(13):

85. Xu, D.S., et al., *Dislocation slip or deformation twinning: confining pressure makes a difference.* Materials Science and Engineering a-Structural Materials Properties Microstructure and Processing, 2004. **387-89**: p. 840-844.

86. Chang, J. and Massachusetts Institute of Technology. Dept. of Nuclear Engineering., *Atomistics of defect nucleation and mobility : dislocations and twinning.* 2003. p. 211

87. Press, W.H. and Numerical Recipes Software (Firm). *Numerical recipes in FORTRAN 77 and FORTRAN 90.* 1996 [cited; 2nd:[1 computer disk].

88. Seitz, F., *On the formation of dislocations from vacancies.* Physical Review, 1950. **79**: p. 890-891.

89. Nabarro, F.R.N., *Theory of crystal dislocations.* International series of monographs on physics. 1967, Oxford,: Clarendon P.

90. Frank, F.C. and W.T. Read, Jr., *Multiplication processes for slow moving dislocations.* Physical Review, 1950. **79**: p. 722-723.

91. Dieter, G.E., *Mechanical metallurgy.* 3rd ed. McGraw-Hill series in materials science and engineering. 1986, New York: McGraw-Hill.

92. Zhu, T., J. Li, and S. Yip, *Atomistic study of dislocation loop emission from a crack tip.* Physical Review Letters, 2004. **93**(2):

Appendix A

Practical Guide for High-Dimensionality NEB

The nudged elastic band technique (NEB) is one of an expanding group of reaction pathway sampling methods whose purpose is to probe configuration space in an efficient numerical manner. These methods have been developed in a variety of fields and are now increasingly applied to problems in materials science where a large number of particles is required to accurately describe the mechanisms of interest. We have performed a number of such studies for topics related to dislocation nucleation. Along the way we have encountered a number of problems and in many cases solutions to address them. Our purpose here is to discuss some practical issues and methods related to high-dimensionality NEB where the details would unnecessarily detract from the explanation of the physical problems discussed in the rest of the thesis.

Well-conditioned Input Configurations:

NEB calculations simply search for the minimum energy path (MEP) between a pair of initial and final stable configurations. The calculated MEP corresponds directly to the local saddle in which the initial guess of the pathway falls. As a result the most critical aspect of such simulations is the initial guess, and while the basic NEB formulation is straightforward, producing quality input configurations can be relatively tricky. In many cases, particularly for simple reaction parameters, input for NEB simulations are obtained via linear interpolation between relaxed initial and final configurations [21, 92]. However, in some instances linear interpolation between the initial and final configuration creates an unphysical or undesirable initial reaction pathway and a satisfactory MEP is unattainable. Also when using the free-end

algorithm [63] as an update to the general NEB formulation, the final configuration is unstable and cannot be created with a numerical relaxation technique. These scenarios require additional input configurations taken directly from MD simulations or perhaps produced by some other method.

Nucleation of a partial dislocation loop at a stress low enough that a stacking fault can be formed stably is a scenario where physically intuitive intermediate input configurations are required. Linear interpolation between a perfect crystal configuration and one containing a stable stacking fault yields a series of images each exhibiting rigid shearing of two half crystals relative to one another. With a periodic boundary normal to the slip plane, the description of the intermediate configurations is somewhat more complex but equally unphysical. Furthermore, the initial guess will never relax to the physical pathway where a small dislocation nucleate is formed and grows into a stable stacking fault configuration. Here a series of intermediary configurations can most easily be obtained via MD. Because our goal is a series of images to be used as input to a static relaxation technique (associated in MD to a temperature of 0 K), it is advantageous to produce input at a very low temperature. In general we performed MD simulations at 0.0001 K with the goal of limiting as much thermal vibration as possible while still allowing for the dynamic evolution of the system. Because the reaction coordinate is the atomic displacement for every particle, even at 1 K the kinetic energy stored in a configuration causes problems for the NEB simulations. Although higher temperatures may seem desirable because they facilitate the activated process of interest output is essentially useless particularly if some linear interpolation will be performed to produce additional images. Typically we have obtained a nucleate at some slightly higher temperature (10 K) and driving stress in excess of the athermal load. The MD simulation was then restarted after an abrupt quench to 0.0001 K and a lowering of the stress to the level at which the NEB simulation was to be performed. in this way a series of configurations containing the physical intuition of a MD simulation can be used to create a physically meaningful initial guess of the mechanistic pathway.

In the standard NEB formulation, a relaxed pathway contains a series of images evenly spaced along the MEP. Unnecessary competition between the relaxation of the pathway with respect to the energy landscape and the relaxation of the images along the pathway due to the

artificial spring force can result in a significant increase in the number of iterations required to relax the path. If the initial distribution of images along the path is far from uniform the spring forces can in some cases dominate the behavior of the simulation resulting in counterproductive iterations of the path or even failure to converge. In general we have found that the artificial spring force very successfully maintains uniform spacing along the MEP but is not as well-suited to creating a uniform spacing, although in both theory and practice it is possible to successfully relax a pathway with initially random spacing. Input configurations uniformly distributed in the reaction coordinate are however much preferred to a random distribution. We have had much success using low temperature MD simulations to output a series of configurations which are uniformly distributed in the reaction coordinate. Typically the steps between MD-derived configurations and the two relaxed endpoints are difficult to match as it is difficult to approximate the length of the path prior to running a MD simulation and several attempts are needed to obtain an appropriate number of evenly spaced configurations. Combing a few MD-derived configurations at key points along the path in terms of defining the mechanism of interest with linear interpolation has proven to be a practical alternative to the full set of MD-derive configurations. Linear interpolation is performed from an initial to an intermediate, or sometimes multiple intermediate, and then to a final configuration. The number of interpolated images between each of the intermediate configurations allows enough flexibility to create an initial series of configurations whose distribution is reasonable uniform without the cost of a MD run for each guess.

A Representation of Simulation Progress:

In regards to physical problems studied with the NEB method, the relaxation of the image spacing along the reaction pathway is not a reportable parameter. The relaxation is informed by the physics included in the potential, but the intermediate steps are of little physical relevance. However as our discussion thus far has indicated, the choice of inputs that will readily converge towards the MEP is not always straightforward, and as such the ability to observe the progress of a simulation is vital to avoid wasted computation. In particular we have found it very useful to plot the evolution of the reaction pathway versus the NEB iterations. A sample plot is shown in Figure A-1 for an ideal NEB run. In the sample simulation well-conditioned input led to easy convergence of the pathway. The most useful feature of the representation of a NEB simulation

presented in Figure A-1 is that it allows for quick observation of whether or not a simulation is converging. Rather than plotting a series of individual energy versus reaction coordinate curves, the behavior of the reaction coordinate alone is typically an adequate indicator of the success or failure of a NEB simulation. Simulations that have "blown up" are typically marked by a single image configuration breaking away from the MEP due either to poorly conditioned input, some incorrect application of the unphysical spring force, or an inadequate restoring force for the dangling image in the free-end algorithm. In these cases the distance between the escaped image and those around it usually expands over the period of a relatively small number of iterations. Often the rogue configuration eventually pulls the rest of the images from the MEP and in some cases the reaction coordinate is returned to a uniform spacing far from any physically meaningful configurations.

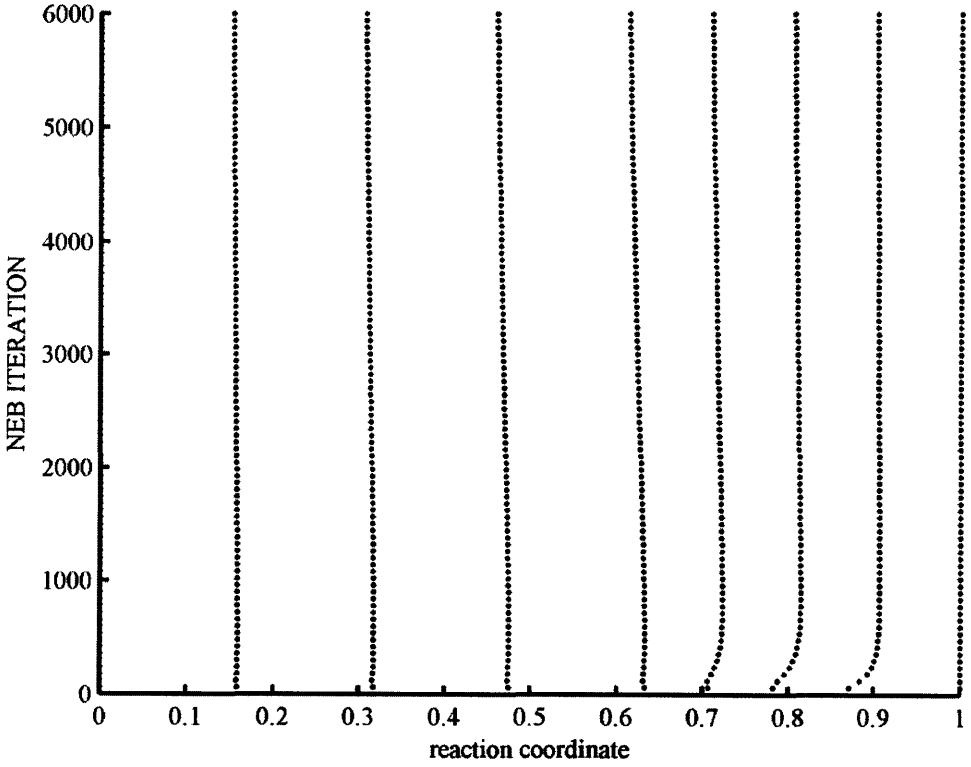

Figure A-1: The behavior of the reaction coordinate as the NEB simulation progresses is one indicator that a simulation is converging.

Methods to Create and Maintain Non-Uniform Image Density:

The competition between computational efficiency and high image density along the reaction pathway is another potential difficulty that can arise for NEB simulations with a large number of particles. The problem is exacerbated in large systems where the reaction pathway can be long compared even to the region of interest. In the example of dislocation nucleation, we are particularly interested in the creation of a shear displacement in the slip plane. The atoms in the two planes adjacent to the slip plane comprise a small fraction of the total number of particles. As a result a significant portion of the path length is devoted to an accurate description of the elastic reaction of the "bulk" atoms after the nucleation event has occurred. As much as one third of the reaction pathway occurs even after the dislocation has moved through the slip plane and been annihilated through the periodic boundary. Henkelman et al suggested a method of variable spring constants in order to bias the image density toward the saddle point regime for a more accurate description of the path near the saddle[62]. They modified the spring constant, k', such that it was dependent on the energy of the configurations bounding the spring:

$$k' = \begin{cases} k_{\max} - \Delta k \left(\dfrac{E_{\max} - E_i}{E_{\max} - E_{ref}} \right) & if \quad E_i > E_{ref} \\ k_{\max} - \Delta k & if \quad E_i < E_{ref} \end{cases} \tag{A.1}$$

where k_{max}, the maximum allowed spring constant, Δk, the difference between k_{max} and the minimum allowed spring constant, and E_{ref}, the energy above which increased image density should occur, are left as user inputs to the technique. The maximum image energy, E_{max}, and the energy at each image, E_i, are updated in the normal way. The concept of a variable spring constant is sound but the formulation does not have the desired effect. The equilibrium condition for the spring force at each image is met when the distances to the next image and from the last image are equal, and the spring force goes to zero. The spring constant simply defines the magnitude of the artificial restoring force. A variable spring constant may cause an initial increase image density in certain situations but would require that the convergence criterion for the gradient of the energy landscape is met prior to the equilibrium condition of the spring force. Convergence to the path is the only real concern so data collected in this way would be sound;

however in the large scale simulations we have run convergence to the path is slow compared to the examples given by Henkelman et al, requiring several thousand iterations instead of less than one hundred. As a result the spring force is able to find the equilibrium uniform spacing. In theory appropriate values of k_{max} and Δk should exist which slow the convergence of the image spacing along the path relative to the convergence of the images to the actual MEP. In practice the slow convergence of the images along the path seems to disrupt the convergence relative to the gradient of the energy landscape, and as a result the simulation becomes increasingly inefficient computationally as the two forces compete.

We have adapted the concept of the variable spring constant to a methodology that works towards a converged path in terms of both the gradient of the energy landscape and the spacing of the images along the path. Effectively this requires a regime where equilibrium occurs for uneven spacing of the images along the reaction pathway. Borrowing the terminology of Equation A.1 we have defined a reference energy, E_{ref}, above which the spring force will act to set up a decrease in the image spacing as the image energy, E_i, increases. The spring force is then defined as:

$$F_{\parallel}^{S} = k(|\, R_i - R_{i+1}\,| - \Delta R|\, R_{i-1} - R_i\,|) \tag{A.2}$$

where the equilibrium distance between images i and i-1 is modified relative to the spacing between images i and i+1 by the factor ΔR which is defined according to:

$$\Delta R = \begin{cases} (\Delta k - 1)\left(\dfrac{E_i - E_{ref}}{E_{\max} - E_{ref}}\right) - 1 & \text{if} \quad E_{i-1} > E_i > E_{ref} \\ \left[(\Delta k - 1)\left(\dfrac{E_i - E_{ref}}{E_{\max} - E_{ref}}\right) - 1\right]^{-1} & \text{if} \quad E_i > E_{ref} \;\&\; E_i > E_{i-1} \\ 1 & \text{if} \quad E_i < E_{ref} \end{cases} \tag{A.3}$$

The action of Equation A.3 is somewhat dramatic as even for a small Δk the final image spacing near the saddle point can be quite small. However, the method does effectively create a discernable decrease in the image density for high energy configurations in pathways relaxed in

regards to the artificial spring force. The image spacing in Figure A-2 at the final iteration is significantly compressed near the vicinity of the saddle point configuration. Moving along the path from the saddle point, at a reaction coordinate of 0.04, towards the final configuration, the image spacing increases until the reaction coordinate reaches 0.25. Farther along the path there is a relatively low density of uniformly spaced images. As a result a more accurate description of the path near the saddle point can be obtained with fewer total images and consequently less computation.

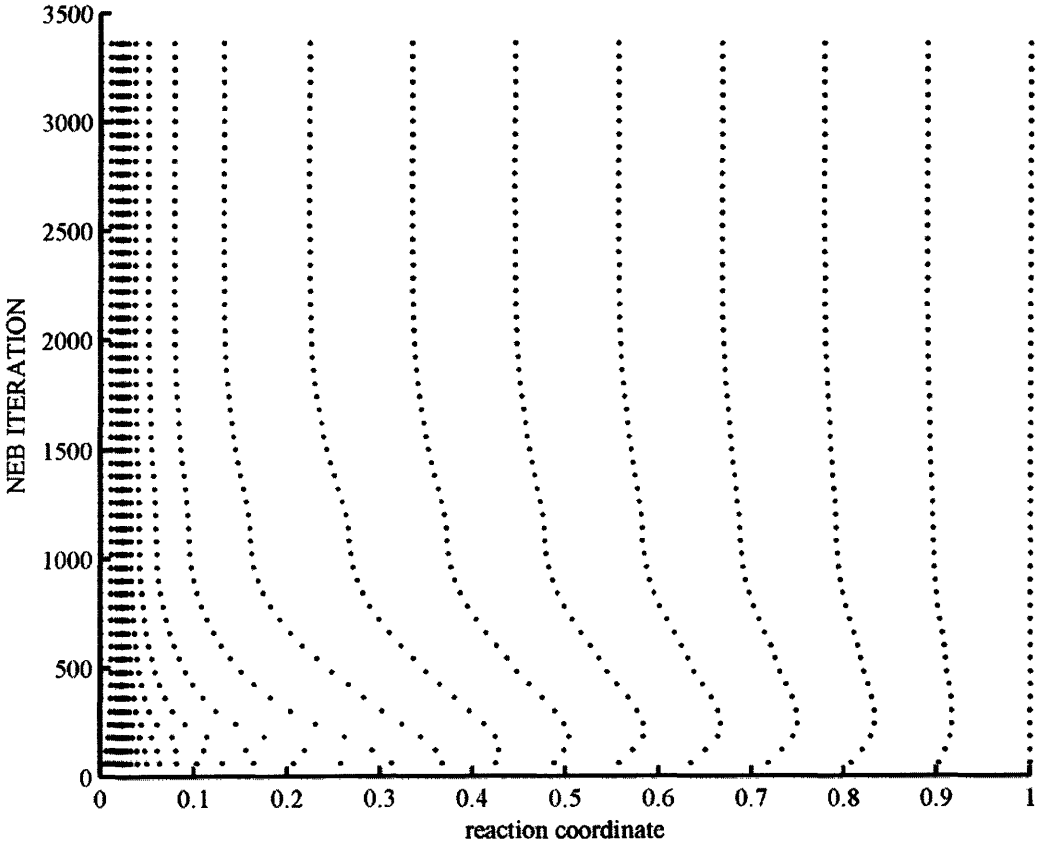

Figure A-2: The behavior of the reaction pathway under the influence of the updated variable spring constant method which creates high image density near the saddle point (reaction coordinate ≈ 0.04) and uniform image density along the portions of the path with $E_i < E_{ref}$.

In this thesis we have also used the CINEB methodology not only for the advantage of finding a more accurate saddle point configuration, but also as a means for biasing the image density. The CINEB generally takes the highest energy configuration as the eventual saddle point which is relaxed according to a different set of forces. In general the climbing image

methodology requires a period of initial relaxation using standard NEB in order to ensure that the configuration chosen to search for the saddle is in fact near to the saddle point. Once the simulation has converged to within the vicinity of the correct path, CINEB iterations using a well condition initial guess of the saddle point can be performed. The decoupling of the saddle point configuration in the CINEB method does not allow for transmission of a difference in spring force across the saddle, and the relationship between the spacing before and after the saddle point configuration in the evolving pathway does not affect the relaxation. Therefore, once a reasonable description of the path is obtained, it is possible to add more images to one side or the other, via linear interpolation for example. In this way a difference in image density is maintained and a more accurate description of the pathway either before or after the saddle is obtained. The use of the CINEB method to maintain biased image density is exhibited in Figure A-2 where the image density prior to the saddle point is significantly higher than after. Our study of shear localization is a prime example of the usefulness of this procedure. In this particular example maintaining the density used prior to the saddle along the entire reaction pathway would have required an order of magnitude more computational time.

Another method for gaining additional information in a very localized portion of the reaction pathway takes advantage of a disconnect between choosing the reaction coordinate as any change in particle position while using empirical potentials that are, correctly, insensitive to rigid translation of the crystal. The NEB methodology has no built in mechanism for correcting a rigid translation and neither the energetics nor the calculated minimum energy path are affected by the presence of such a translation. However by introducing translation between two images the pathway is effectively stretched in terms of the reaction coordinate. More images are required to transverse this length of path because each particle contributes to the reaction coordinate a small displacement due to the translation. Reversion of the increased image density to the physical path length is easily performed by resetting the center of mass for each configuration along the pathway to the same position. The advantage of this method over all others discussed above is that it can be used at any point along the pathway. In general the best results are obtained by first relaxing a series of uniformly spaced images to the minimum energy pathway. With the mechanistic information provided by these images, the region of interest is easily identifiable. Relaxed images just before and just prior to the local pathlength of interest become the boundary

of the translated region. By performing any simple, equivalent translation on all the images prior to the region of interest and then interpolating between the two chosen boundary images an increased image density can be naturally maintained with no change in the NEB formulation.

Updated Free-end Method (Catching an Escaped Path):

When using the NEB method to calculated the activation energy for a specific process, it is often beneficial to use the recently devised free-end algorithm to increase computational efficiency by reducing the number of images required to accurately describe the path in the vicinity of the saddle point. In general the NEB method requires two stable end points which are relatively easy to obtain via numerical relaxation techniques such as the conjugate gradient method. However, the unstable configuration from which the "free end" algorithm derives its name poses a practical difficulty not encountered in standard NEB implementations. We have discussed above the use of MD simulations to condition input data for use as either intermediate or unstable final images. In general these images are not fully relaxed to the minimum energy path (if they were the NEB method would be redundant). While the free-end algorithm is designed to swing the final configuration along the energy landscape in order to keep the preceding images from relaxing down the gradient in the energy landscape, in practice the path is prone to escaping from the free end. The basic algorithm has no means for restoring the path once a portion has moved below the free end.

It is difficult to visualize the behavior of these pathways in the high-dimensionality space needed to describe them. However, our observation has been that the portion of the path that escapes the free end does so by moving more quickly towards the minimum energy path than the free-end itself. Consequently, by taking the initially escaped image as a new free end, the process of escaping can be used to search for a stable free-end configuration. Since the goal of the free end algorithm is the use of relatively few image configurations there are typically not many to spare and simply discarding the defunct free end and replacing it with the escaped image can quickly remove too many of the images. We have found the process of taking the escaped image as a new free end and then linearly interpolating between the new free end and the current saddle point to be the most effective means of searching for a stable free end. In Figure A-3 unconverged reaction paths before and after updating the free end are plotted in the standard

energy versus reaction coordinate representation. We updated the free end and performed linear interpolation when the energy of the image prior to the current free end is less than or equal to the energy of the free end. Earlier criterion are likely possible, but the simple energy criterion has proved effective. A series of such free end updates may be necessary. In Figure A-4 the pathway escapes from the free end five times, as observed by the discontinuities in the reaction coordinate versus iteration, before finally relaxing to the minimum energy pathway

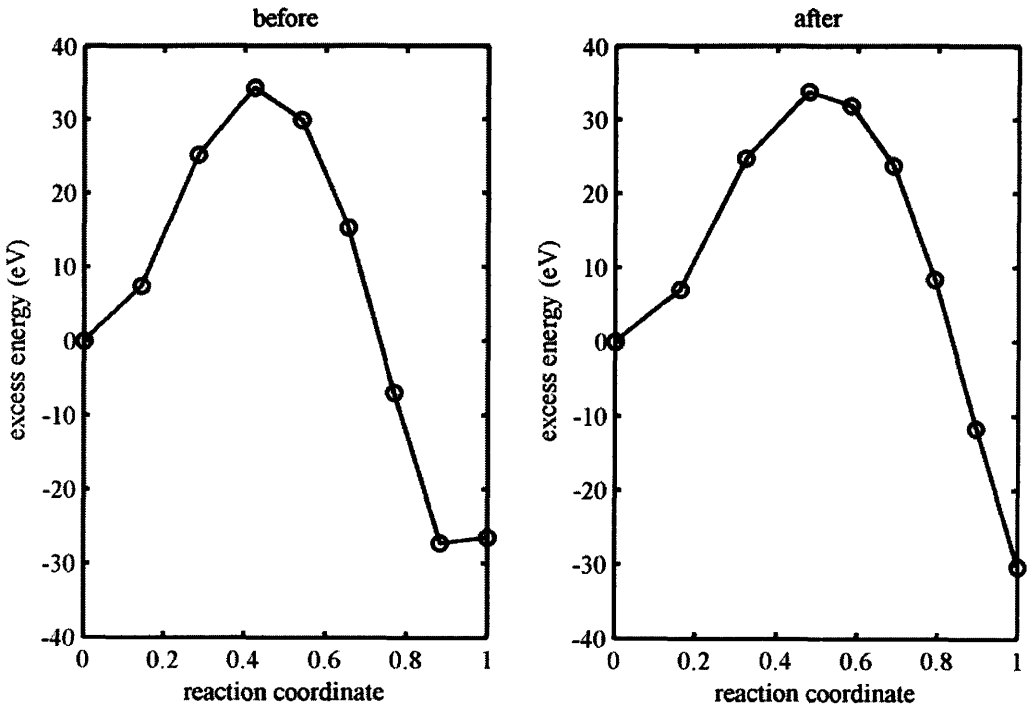

Figure A-3: The reaction pathway for an unconverged NEB simulation utilizing the free-end algorithm is a) susceptible to escaping the 'free end' but b) can be caught via a simple addition to the methodology.

We must also note that the use of linear interpolation is particularly useful in this case because of the nature of the saddle point configuration. We show in chapter two that for homogeneous dislocation nucleation the saddle point is an in-plane shear perturbation for a large range of shear stresses below the athermal stress. Linear interpolation from a perfect crystal to a shear perturbation past the saddle point gives a series of shear perturbations with increasingly large maximum displacement. For stresses approaching the athermal stress such a series of

configurations is a reasonable guess at the pathway near the saddle. Linear interpolation of a fully formed dislocation loop, as would be required at lower stresses, creates a series of in-plane shear plateaus which are non-physical. As a result the method described above for catching an escaped free-end takes longer to converge because each linear interpolated guess of the pathway between the saddle and the free end is initially non-physical. In this case some other method for updating the path after it has escaped the free end may be necessary.

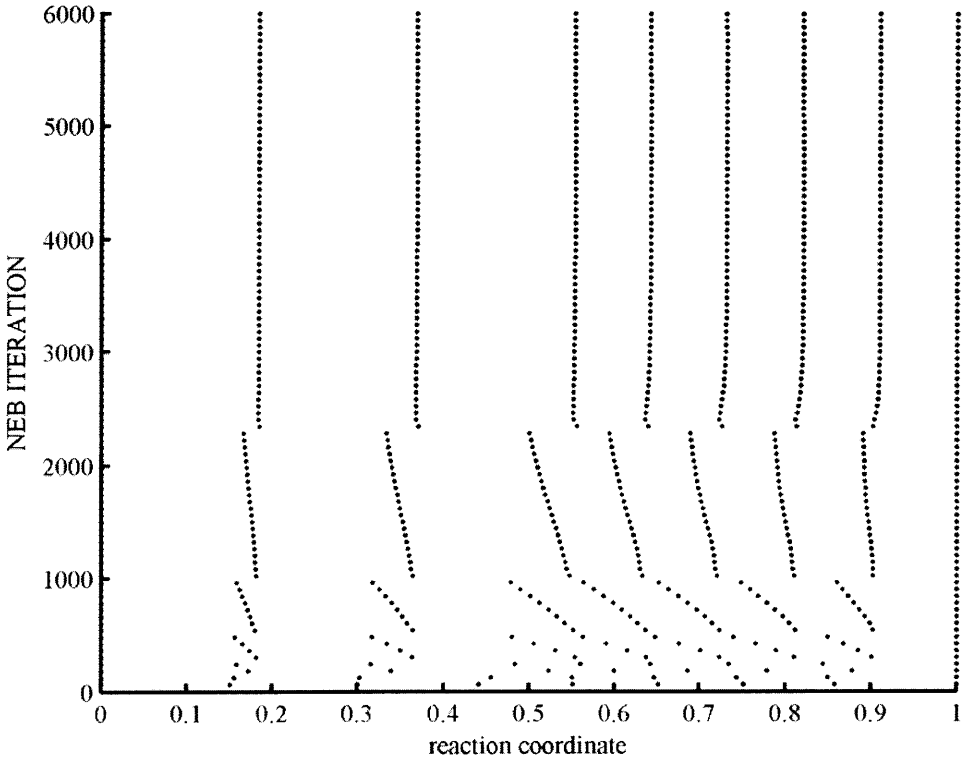

Figure A-4: The reaction pathway escapes from the free end and is updated five times before finding a stable free end which allows the simulation to converged to the minimum energy pathway.